Spectroscopy and Kinetics of Reactive Intermediates in the Atmosphere of Venus: The Catalytic Role of Chlorine Atoms

Thesis by

Wen Chao

In Partial Fulfillment of the Requirements for
the degree of
Doctor of Philosophy

CALIFORNIA INSTITUTE OF TECHNOLOGY
Pasadena, California

2024
(Defended May 13, 2024)

Wen Chao
ORCID: 0000-0003-0602-1606

ACKNOWLEDGEMENTS

For the most part of my thesis, I would like to thank thionyl chloride (Cl_2SO) and the ClSO radicals. The mysterious sulfur and chlorine chemistry are very little studied and has provided a large room for me to explore the science behind interactions of sulfur and chlorine. I could not have completed my PhD without their interesting and special reactivities.

To officially start off, I must acknowledge my collaborators at NASA Jet Propulsion Laboratory—Fred Winiberg, Carl Percival, and Stanley Sander. Dr. Winiberg introduced the unexplored chemistry that occurs on Venus to me. I have had a great time working with him to rationalize the role of chlorine atoms in Venus' mesosphere. I would like to thank Dr. Percival for giving me the opportunity to continue working on atmospheric chemistry in Earth's atmosphere, especially the Criegee intermediates. His expertise in combining field measurement results and laboratory studies really showed me how fundamental science helps to solve real-world problems. To accomplish these projects, I would like to thank Dr. Sander. I could not have finished all the tasks without his wisdom and rich knowledge, especially regarding iodine chemistry. Of course, I would like to acknowledge my advisor, Mitchio Okumura, for making connections with JPL scientists and showing me the beauty of English writing, which I will continue to improve at throughout my life.

I would like to thank my colleague, Greg Jones, who convinced me to start working on ab initio calculations. His mentorship and detailed explanations really helped me to overcome the barrier of theoretical calculations. Following his steps, I eventually gained the confidence to conduct calculations and interpret the results of ClCO radicals. A hidden colleague for my thesis is Dr. Markus, who expanded my ability to work on Python code for data analysis. Besides, I learned so much from him about the infrared measurements, including linewidth, optics properties, and applications.

I'd also like to thank my committee—Scott Cushing, Paul Wennberg, and Yuk Yung for all their advice to guide my future and point out my weaknesses, helping me to become a better scientist.

My PhD work has been funded by Dr. Winiberg via the NASA Solar System Workings Program. I would like to thank the J. Yang Scholarship (founded by the J. Yang & Family Foundation) which, at a key moment in my PhD life, provided me with three months of funding to initiate the

collaboration with NASA JPL. The de Karman Fellowship supported me through my last year of PhD life, during which many memorable events occurred.

I need to thank my family for supporting me in pursuing my PhD. I would also like to thank my friends for their company during this five-year journey. They taught me how to play badminton and softball, though I am still quite bad after a few years of practice. Finally, I would like to thank my roommates for the traditional Chinese board game nights and the discussions about the tips of “traveling with points”.

There are so many people I should mention who helped me finish the journey of my PhD degree. It is entirely my fault if anyone important is not mentioned above. As I get close to the end, I want to pray to the universe that all the kind and friendly people I met have a happy and rich future.

ABSTRACT

Chlorine chemistry plays essential roles in both industrial and academic fields due to the special reactivity required to initiate or catalyze important reactions in our daily life. For example, Cl atoms are the most common oxidation agents in combustion and are famous for the catalyzed destruction of ozone that eventually leads to the ozone hole.

As terrestrial planets, Venus and Earth's atmospheres have similar origins but very different evolutions. Compared to Earth, Venus suffers strong water loss in hydrodynamics escape due to its distinct distance from the Sun; as a result, high abundances of chlorine and sulfur species are not trapped in the sea and survive in Venus' atmosphere. For example, a dense cloud, made with sulfuric acid, has been observed at the middle altitude (50 - 70 km) and the concentration profiles for distinct species (SO_2, CO, CO_2, O_2…, etc.) have been measured during the Venus Express mission operated by the European Space Agency. Digging into the discrepancy between the observations and model simulations, a few important questions arose, and further laboratory studies are needed to solve the puzzles, including (1) the unknown UV absorber, (2) the SO_2 concentration inversion at high altitude and (3) the extremely low O_2 and high CO_2 abundances, wherein a reactive chlorine atom is proposed for explaining these phenomena.

In this thesis, we performed the pulsed-laser photolysis experiments with a homemade time-resolved broadband UV-Vis transient-absorption spectroscopy coupled with a temperature- and pressure-controlled flow reactor to study the spectroscopic and kinetic properties of key intermediates (ClSO, ClCO and $ClCO_3$) in the oxidation process of sulfur and carbon to ultimately form SO_2 and CO_2. The recorded spectra are analyzed, and high-level ab initio calculations were performed to rationalize the electronic structures of target molecules to reveal the catalysis role of Cl atoms. In addition, key reaction rate coefficients (ClSO + Cl, $k_{\mathrm{ClSO+Cl}}(292\ \mathrm{K}) = (1.48 \pm 0.42)\times10^{-11}\ \mathrm{cm^3\ molecule^{-1}\ s^{-1}}$; ClCO + O_2, $k_{\mathrm{ClCO+O2}}(0) = (9.0 \pm 2.3) \times 10^{-32}\ \mathrm{cm^6\ s^{-1}}$ a $\mathrm{cm^3\ molecule^{-1}\ s^{-1}}$), and thermodynamic property (Cl + CO $\rightleftharpoons$ ClCO, $K_{\mathrm{eq}} = 1.8\times10^{-18}\ \mathrm{molecules\ cm^{-3}}$) have been measured to further assist the model simulations.

This thesis not only offers essential data for model simulations to understand the complex chemistry in Venus' atmosphere but also provide new insights to guide future tasks to explore Venus, e.g. DAVINCI+ and VERITAS by NASA.

PUBLISHED CONTENT AND CONTRIBUTIONS

Winiberg, F. A. F.; Chao, W.; Caravan, R. L.; Markus, C. R., Sander, S. P.; Percival, C. J. "A white cell based broadband transient UV-vis absorption spectroscopy with pulsed laser photolysis reactors for chemical kinetics under variable temperatures and pressures". *Rev. Sci. Instrum.* 94, 114103 (2023). DOI: 10.1063/5.0164733

W.C. participated in experimental measurements, data analysis, validation, visualization and wrote the original manuscript.

Chao, W.; Jones, G. H.; Okumura, M.; Percival, C. J.; Winiberg, F. A. F. "Spectroscopic and Kinetic Studies of the ClSO Radical from Cl_2SO Photolysis". *J. Am. Chem. Soc.* 144, 44, 20323-20331 (2022). DOI: 10.1021/jacs.2c07912

W.C. participated in conception of project, experimental measurements, data analysis, validation, visualization and wrote the original manuscript.

Chao, W.; Jones, G. H.; Okumura, M.; Percival, C. J.; Winiberg, F. A. F. "A-Band Absorption Spectrum of the ClSO Radical: Electronic Structure of the Sulfinyl Group". J. *Phys. Chem. A* 127, 8374-8382 (2023). DOI: 10.1021/acs.jpca.3c04977

W.C. participated in conception of project, experimental measurements, theoretical calculations, data analysis, validation, visualization and wrote the original manuscript.

Chao, W.; Markus C. R..; Okumura, M.; Winiberg, F. A. F.; Percival, C. J. "Chemical Kinetic Study of the Reaction of CH_2OO with CH_3O_2". J. *Phys. Chem. Lett.* 15, 13, 3690-3697 (2023). DOI: 10.1021/acs.jpclett.4c00159

W.C. participated in conception of project, experimental measurements, data analysis, validation, visualization and wrote the original manuscript.

TABLE OF CONTENTS

LIST OF FIGURE AND TABLES

Chapter 1

Chapter 2

Chapter 3

Chapter 4

Chapter 5

Chapter 6

SUMMARY

The work outlined in this thesis cover the spectroscopic and kinetic measurements of the two important radicals, ClCO and ClSO, in Venus' mesosphere. Chapter 1 discusses the details and performances of the homemade UV-Vis spectrometer, which was used to measure the UV-Vis spectrum and temporal profiles of target radicals. Chapter 2 and Chapter 3 detail the electronic structure of ClSO radicals and their kinetics with Cl atoms to generate thionyl chloride. The similarity with other sulfinyl radicals are also discussed. Chapter 4 and Chapter 5 discuss the spectroscopic and kinetic properties of ClCO radicals. The results and ideas needed to obtain the critical kinetic parameters, including the ClCO equilibrium constant and the ClCO + O_2 reaction rate coefficients, are discussed. Finally, Chapter 6 discusses the important CH_2OO + CH_3O_2 reaction in Earth's troposphere, which shows the wide applications of the homemade UV-Vis spectrometer.

Chapter 1—A White Cell Based Broadband Transient UV-Vis Absorption Spectroscopy with Pulsed Laser Photolysis Reactors for Chemical Kinetics under Variable Temperatures and Pressures

This chapter is reprinted and adapted with permission from Rev. Sci. Instrum. 94, 114103. Copyright 2023, American Institute of Physics.

1.1—Abstract

UV-Vis spectroscopy is widely used for kinetic studies in physical chemistry, as species' absolute cross-sections are usually less sensitive to experimental conditions (i.e., temperature and pressure). Here, we present the design and characterization of a multipass UV-Vis absorption spectroscopy White cell coupled to a pulsed-laser photolysis flow reactor. The glass reactor was designed to facilitate studies of gas phase chemical reactions over a range of conditions (239 – 293 K and 10 – 550 Torr). Purged windows mitigate contamination from chemical precursors and photolysis products. We report the measured impact of this purging on temperature uniformity and the absorption length, and present some supporting flow calculations. The combined optical setup is unique and enables the photolysis laser to be coaligned with a well-defined absorption pathlength probe beam. This alignment leverages the use of one long-pass filter to increase the spectrum flatness and increase the light intensity, versus other systems that use two dichroic mirrors. The probe beam is analyzed with a dual-exit spectrograph, customized to split the light between an intensified CCD and photomultiplier tube, enabling simultaneous spectrum and single wavelength detection. This multipass system yields a pathlength ~450 cm; minimum observable concentrations ~3.7×10^{11} molecule cm^{-3} (assuming cross-sections ~1.2×10^{-17} cm^{2}). The temperature profile across the reaction region is ±2 K, defined by the worst-case at 239 K, validated by measurements of the N_2O_4 equilibrium constant. Finally, the system is implemented to study the simplest Criegee intermediate, demonstrating the instrument performance and advantage of simultaneous spectrum and temporal profile measurements.

1.2—Introduction

UV-Vis absorption spectrometers have been widely applied to many fields, (e.g., atmospheric chemistry, organic chemistry, combustion chemistry and planetary chemistry) to quantitatively study reaction kinetics.[1] The UV-Vis spectral region possesses information about the excited states of the target species, and the absorption cross-sections are typically large but with fewer spectra features. [2] Additionally, the alignment of UV-Vis light is facilitated by an easily observable beam to the naked eye. Most importantly, the UV-Vis cross-sections of most species of interest are less affected by the experimental conditions, such as pressure, temperature, buffer gas composition (in the gas phase) and the solvent species (in the liquid/aqueous phase).[3,4]

For typical small-scale gas phase photochemical kinetics measurements, precursor gas mixtures are flowed into a reactor and chemistry is initiated with a flash photolysis light source (typically a UV laser pulse). Depending on the photolytic precursor and target reactant, multiple species with similar functional groups are likely to be present in a given chemical system. Therefore, in the UV-Vis region, competing unwanted secondary reactions might significantly perturb the measurements of target species because of overlap of interfering molecular absorptions. To overcome these difficulties, photochemical kinetics measurements are usually performed at low starting radical/atom concentrations, which results in small product signal intensities.[4] In short, several factors are necessary for an accurate photochemical kinetic apparatus in the UV-Vis region to measure rate coefficients and product branching ratios important to Earth and planetary atmospheres: (1) knowing the absolute concentration of target molecules (i.e., well-defined absorption pathlength and absolute cross-section), (2) high sensitivity (e.g., a multi-pass system), (3) continuous monitoring in real time with a μs time resolution (a bright continuous light source with high-speed data acquisition, DAQ, card and fast response detector), (4) wide spectral coverage (grating and charge-coupled device, CCD), (5) ability to measure under atmospherically relevant conditions (e.g., reasonable temperature and pressure range). [5]

Multipass optic UV-Vis apparatuses have grown in popularity in recent years, particularly in response to the measurement of Criegee intermediates, which have unique and strong UV/Vis cross-sections ($\sim 1\times10^{-17}$ cm^2) close to 340 nm. Typical multipass systems that have been employed in recent years for kinetics measurements include optical cavities, both broadband[6,7] and single wavelength[8], Herriot optics arrangements (single wavelength, but scanned)[9], and custom spherical mirror arrangements.[10,11] Experimenters must also choose to house the multipass optics inside the reaction volume or externally. Cavities favor being positioned inside the gas flow to avoid transmission losses through successive passes through windows that enclose the reactor. Each option represents a trade-off in terms of pathlength (>1000 m for cavities) versus signal-to-noise at the detector, where the longer pathlength is inversely proportional to the number of photons impinging the detector. Calibration of the intersection region of the probe and photolysis beams is also paramount for accurate chemical kinetics measurements, and must be considered in the design and characterization of the system.

In this article, we present the design, installation, and characterization a new broadband UV-Vis spectrometer for gas phase pulsed-laser-photolysis reaction kinetics studies over a range of temperatures and pressures (239 – 293 K and 10 – 550 Torr).

1.3—Experimental Setup

1.3.1—Flow Reactor Design

Figure 1 is a schematic of the gas-phase flow reactor. The reactor is a 40 mm internal diameter, 46 cm long tube, with an external jacket designed for coolant fluid surrounding the reaction region. The temperature is controlled by flowing chilled methanol through the outer jacket using a commercial chiller (ThermoFisher, 156-5408), which allows the reactor temperature to be controlled between 239 – 293 K. Chilled methanol flows first through the reactor jacket, then to a pre-cooled inlet (modified Graham condenser, Chemglass, CG-1830-30), before returning to the chiller. Before the experiments, the reactor gas temperatures are calibrated by direct measurements in the reactors and the temperature of chilled methanol by two thermocouples (OMEGA, TT-T-24-100 and TT-E-30). The thermocouples were calibrated by liquid nitrogen (77 K), methanol/dry ice mixture (195 K), water/ice mixture (273 K) and the boiling water (373 K). Coolant flow connectors are not shown in Figure 1, but were located at either end of the flow reactor, introducing coolant on the bottom of the reactor.

The main gas flow is introduced into the reactor in the center, and removed at either end. The gas flows are controlled by several mass-flow controllers (MKS, GM series), with overall reported accuracies of ~0.2% of the total flow scale. The total pressure of the flow reactor is controlled by a butterfly-type throttle valve (MKS, type 153), and has a total pressure range between 10 – 550 Torr. Reactor pressures are measured using 100 and 1000 Torr diaphragm-based capacitance manometers (MKS, 127AA series) at the gas exhaust, with overall reported accuracies of ~0.5%.

A small flow of total bath gas flow (5%) is diverted to purge the inner side of the reactor windows to prevent undesired photochemistry product deposition. In an early prototype, accumulation of such products was observed to reduce the transmission of the probe beam light when photolyzing oxalyl chloride or di-iodomethane precursors, greatly reducing signal-to-noise of the absorption measurement.

The windows are mounted on “purge arms” using O-ring seals. The “purge arms” were small flow tubes that interfaced with the main reactor using a glass KF-40 type connection. The outer diameter (OD = 38 mm) of the “purge arms” were slightly smaller than the main flow reactor inner diameter (ID = 40.0 mm), and guided the purge flow directly to the main reactor gas flow exhaust connections. This also enabled the windows to be held at room temperature when the reactor is cold, without the risk of condensation forming on the windows, in the beam path.

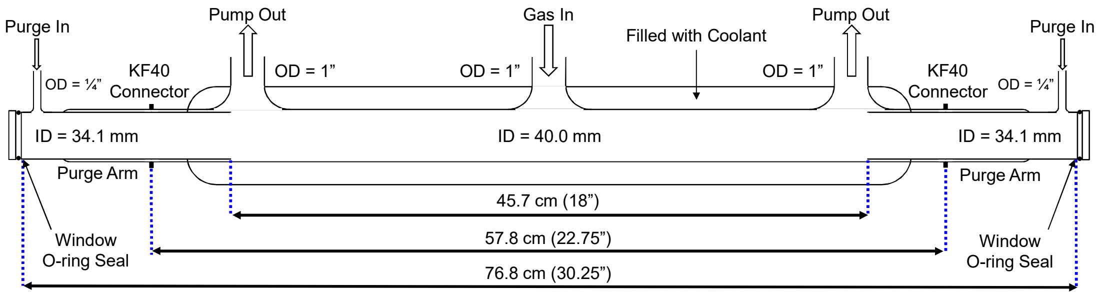

Figure 1.1. Schematic of the jacketed glass flow reactor. The coolant flow connectors are not shown for simplicity.

1.3.2—Optical Design

The schematic summary of the optical design is shown in Figure 2. Broadband light (190 – 2100 nm) from a Laser Driven Light Source (LDLS, Energetiq, EQ99) provided the probe beam for the apparatus. The LDLS was fiber optically coupled, which enabled a collimated light beam to be produced using a parabolic mirror (Thorlabs, RC08SMA-01). Collimated light was guided into a custom White-cell-type multipass optical system, consisting of aluminum spherical mirrors with UV anti-reflection (AR) coating (Acton H1900-1D-PLCC-140-D, *f* = 140 cm, #1900 coating). Light exiting the multipass system was directed towards a spectrograph (Acton, 300i), focused at the slits using a lens (1” dia., *f* = 100 mm, Newport, SPX022AR.10). All 45 degree turning optics used were enhanced UV aluminum mirrors (1” dia., Thorlabs, PF10-03-F01).

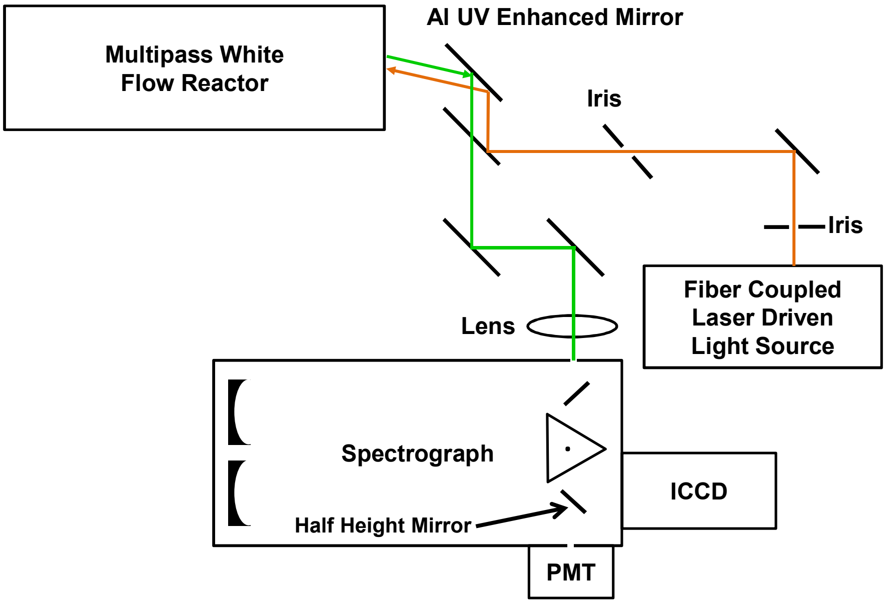

Figure 1.2. Schematic of the optical setup, external to the multipass White cell.

The White cell design optimizes the overlap between the photolysis laser beam and the broadband probe-beam inside the reactor. The distance between the field mirror and object mirrors is 140 cm, matching the radius of curvature, with the reactor positioned towards the field optic. The photolysis laser beam (λ = 248 nm) from an excimer laser is loosely focused (SCX-25.4-152.6-C) into the gap between two objective mirrors of the White cell (gap = 20 mm) and then aligned using turning optics (Newport, 20QM20EM.15) to aim towards the field optic (Figure 3). A 0° angle-of-incidence (AOI) long-pass optical filter (Semrock, LP02-257RU) is aligned at a shallow angle and separates the photolysis laser beam from the probe-beam before the field optic. The long-pass filter protects the field optic from damage, while removing scattered UV excimer light from the probe-beam path, and therefore from entering the spectrograph. The reflected excimer light is dumped into a home-made, black-painted Wood's horn. This optical configuration allows: (1) the photolysis laser beam to be approximately co-linear with the probe beam, (2) the photolysis laser beam to fully fill the flow reactor, resulting in a well-defined absorption path length, and (3) the minimum number of optics in the probe-beam path without placing the mirrors inside of the reactor.

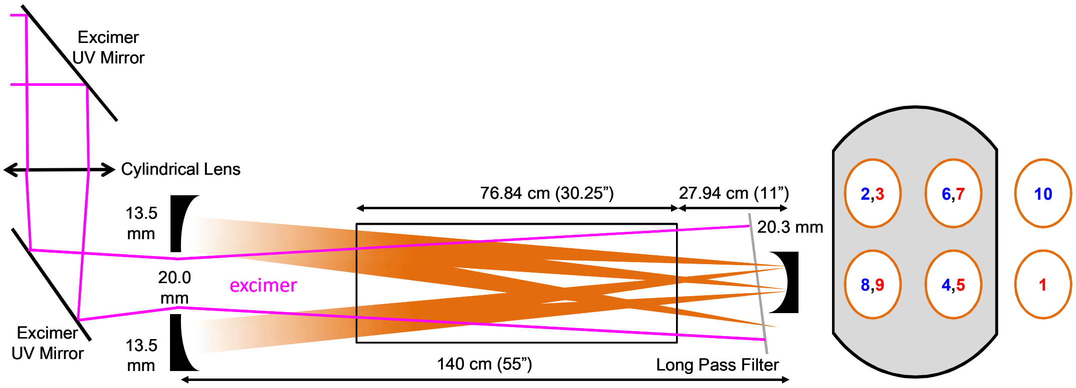

Figure 1.3. Schematic (not to scale) of the white cell setup for ten passes. The entrance and exit apertures for the White cell system are vertically stacked, in the plane of the page, and so appear on the same side of the field optic. The right panel shows the beam spots observed on the field mirrors. The red and blue number shows the probe beam go backward and toward the field mirrors.

Light multipassed through the White cell is maximized by using highly reflective White cell optics (R >97%, λ = 340 nm), combined with AR coated windows (Edmund Optics, 36-948, 3 mm thick, T = 98%, λ = 340 nm). The long-pass filter sits in the multipass probe-beam path, and so also contributes to cumulative light losses, as can be seen in Figure 4A.

The spectrograph has been modified to simultaneously collect light on to a photomultiplier tube (PMT, Hamamatsu, R928) and an image-Intensified CCD camera (ICCD, Princeton Instrument, PI-MAX 4) using a half-height turning mirror. The half-height mirror was aligned such that the probe light from the grating was split vertically. This enabled ~25% of the light intensity to be directed towards the exit slits, and the PMT, with the remaining

75% carrying on past the mirror towards the ICCD. In a previous prototype, a 50:50 beamsplitter was used to reflect/transmit the whole grating image, however internal reflections inside the beamsplitter were found to produce “ghost” images on the ICCD detector, precluding accurate spectra measurements.

This half-height mirror configuration enables kinetic time traces to be collected on the PMT at the grating central wavelength, while simultaneously recording spectra over a series of delay times (see section 2.3 for more detail on the data acquisition), without the need for switching the exit aperture turning mirror position in a stock spectrograph. To assess kinetic profiles across varying wavelengths, the grating is adjusted, and the calibrations for both the ICCD and the PMT need to be validated. However, the Acton 300i spectrograph features a wavelength repeatability of roughly ±0.05 nm. This level of precision has been checked using a Hg-Ar pen-ray lamp and is determined to be below the spectral resolutions needed for the actual experiments, as illustrated in Figure S4. Therefore, we only checked the wavelength calibration before and after the experiments within a day. For optimal results, it is advisable to perform calibration following each adjustment to the grating to maintain accuracy.

1.3.2.1—Light Sources

1.3.2.1.1—Probe Beam

The LDLS, in which a high power infrared laser is focused into a Xe lamp to generate a small plasma (~ 100 μm dia.),[12] provides an output spectrum covering the deep-UV to near-IR region. The output light intensity is reasonably flat and the intensity near 200 nm is about 10 mW mm^{-2} sr^{-1} nm^{-1}, which is a factor of ~10 greater than a typical xenon arc lamp (~1 mW mm^{-2} sr^{-1} nm^{-1}).[12,13] In the current configuration, the spectral coverage is limited to a range of 260–520 nm due to the constraints imposed by the long-pass filter and the second-order diffraction from grating (figure S4). Figure 4A shows the probe light spectra as captured by the ICCD. The grating in our spectrograph has blazed at 300 nm and grooves equals 600 per millimeters, offering a coverage span of about 120 nm across 1204 pixels. Although the center wavelength can be adjusted between 200 nm and 600 nm, the detector's quantum efficiency drops for wavelengths exceeding 400 nm, which predominantly influences the observed profile. It is crucial to note that different spectral coverage could be achieved by alternative gratings, optics, and detectors.

While the LDLS is a brilliant light source, the light intensity has been observed to oscillate with a period ~23.5 μs (Figure 4B), resulting in a ~7% power fluctuation. The impact of this instability on spectroscopic data can be minimized by either implementing a "lock technique",[14] which has been shown in the literature to be highly effective, or simply to integrate the light across multiple periods using random triggering, to average out the fluctuations.

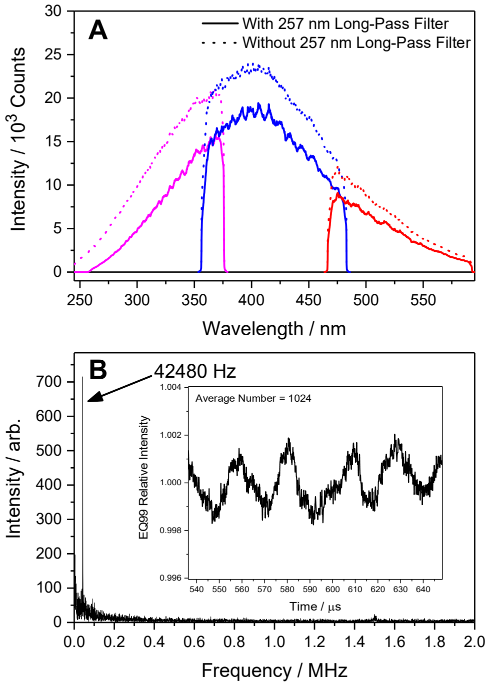

Figure 1.4. (A) The observed spectra of LDLS source as recorded by ICCD detector. The dotted and solid lines show the spectra with and without the long-pass filter on the probe beam light path. The magenta, blue and red colors denote the grating center wavelengths to be 310 nm, 420 nm and 530 nm. Oscillation on the magenta line is caused by the long-pass filter. (B) The noise frequency spectrum of the output of the LDLS, which shows a strong oscillation at 42,480 Hz. The inset shows the temporal profile recorded by the PMT of this apparatus. The impact of the oscillation on data acquisition is greatly reduced by averaging with random triggering. The smallest detectable absorption is about 6.5×10^{-4} after 1024 averages (>3σ of the noise).

1.3.2.1.2—Photolysis Laser

The pulsed-photolysis light source is a fluorine gas excimer laser (Coherent, COMPex 205F, Krypton Fluoride), which produces ~300 mJ pulse^{-1} at λ = 248 nm. The repetition frequency of the laser is 5% slower than the gas residence time, to ensure that the gas is entirely replenished each time the laser is triggered. The excimer laser light is loosely focused horizontally and then expanded using a cylindrical lens placed between the final two alignment mirrors, such that the light fills the entire ID of the reactor (~1.5”), maximizing overlap of the probe and photolysis beams (Figure 3). The horizontal profile widths at the input and output of the reactor's relevant region measure around 31 mm and 40 mm with laser energy 130.90 mJ and 98.45 mJ, respectively. While the photolysis power inside the reactor may not be highly uniform, kinetic measurements can still proceed effectively by operating at low concentrations, especially to mitigate the influence of self-reactions for radical species. Kinetic measurements under pseudo-first-order conditions are fairly acceptable, as validated by the kinetics of CH_2OO, which has a notably high self-reaction rate coefficient[15] (see Section 3.4 Chemical Kinetics System Characterization). By carefully regulating the concentration of radicals, second-order kinetics, such as $Cl + ClSO \rightarrow Cl_2SO$,[16] can also be quantified.

1.3.2.2—Detectors

An image-intensified CCD camera and a PMT are used to obtain spectra and monochromatic temporal profiles, respectively. Both detectors have high gain and are suitable for monitoring low intensity light, which enables longer path lengths in the multipass absorption setup. The noise levels for the PMT and the ICCD are about 0.2% and 0.06% in intensity (1024 average, ICCD gate width = 47 μs, DAQ Sampling Rate = 10^6 samples s^{-1}, PMT Output Intensity = −344), respectively, which could be further reduced by increasing the average number. The PMT signal chain has a response time of ~6 μs, limited by a home-made transimpedance amplifier circuit (LF357, gain-bandwidth product

= 5 MHz, R_f = 50 kHz, C = 720 pF). Amplified signals from the PMT are recorded using a DAQ card (Gage, CS144002U).

Because the LDLS is continuous, the temporal resolution of the experiment is limited primarily by the speed of sequential spectrum acquisition by the ICCD, which can be characterized experimentally. The ICCD couples a CCD array with a gated microchannel plate and phosphor screen. When photons interact with the photocathode at the inner side of the window, an electron is released, which then interacts with the wall of the microchannel plate (MCP) capillaries, causing an electron avalanche. These electrons interact with a phosphor screen and the phosphorescence light is collimated by a fiber optic bundle and then imaged by a CCD array. The electron cascade is fast, and so the minimum sequential spectrum period is ultimately controlled by the phosphorescence lifetime of the phosphor screen and the ICCD readout time. The phosphorescence lifetime (Figure 5) was characterized using a pulsed UV light-emitting diode (LED) light source (Marktech Optoelectronics, MT3650N3-UV) driven by a delay generator (Stanford research, DG535) with pulse length 10 μs. The shortest period between two sequential spectra for our ICCD is about 15 ms, which is mainly limited by the ICCD readout time; therefore, we acquire the reference 15 ms before the photolysis laser fires (e.g., t = 0 s, or t_0) and spectra at different delay times are obtained by changing the delay between frames. The ICCD MCP gate width (i.e., integration time) is adjustable and set to 47 μs to match the oscillation frequency of the LDLS for present studies in this work.

Both detectors are wavelength calibrated, using a Hg-Ar pen-ray lamp. The spectral resolution of the detectors is controlled by the entrance slit width (typically 150 μm), leading to a spectral resolution of 0.4 nm near 340 nm (based on a Gaussian fit to the Hg-Ar emission lines to determine the FWHM).

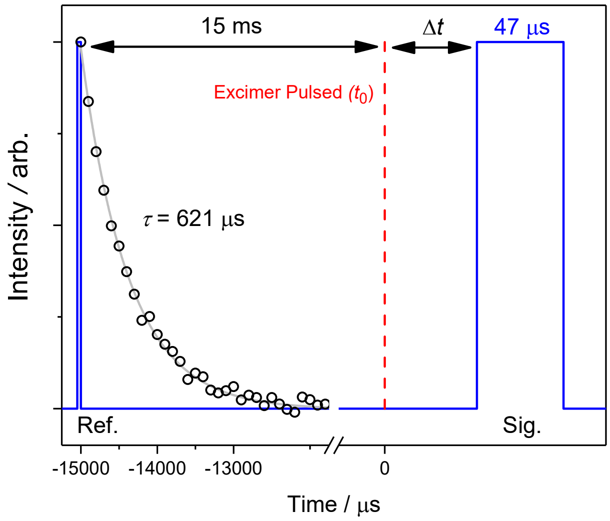

Figure 1.5. Time trace showing the exposure times of ICCD (47 μs, blue), the phosphorescence decay (black circles) and the excimer pulse (red). The gray line shows the fit of exponential function yielding a lifetime about 621 μs. Two exposures are required for one selected sample spectrum at a given Δt, the first is the reference, I_0 ($t_0 - 15$ ms) and second is the sample, I ($t_0 + \Delta t$) spectra.

It is worth mention that the complementary Metal-Oxide-Semiconductor (CMOS) detector is another alternative. The CCD cameras typically involve charge transfer across the entire sensor and have a single digital output, limiting their ability to quickly capture a series of images. Residual charge during this transfer can also introduce issues, requiring additional time to clear the pixels. However, the single digital output yields a uniform noise pattern, thereby enhancing overall image quality. The slower readout speed is also suitable for applying other image intensification techniques.

On the other hand, CMOS cameras have individual digitizers for each pixel, which greatly speeds up the readout process. However, this design introduces individual readout noise for each pixel, resulting in a fixed-pattern across the image. Moreover, commercial CMOS options are somewhat limited in their capabilities for deep-UV (200−300 nm) and IR detection (>1000 nm). While image intensification techniques can convert UV light to visible light, the associated decay time, e.g., phosphorescence decay shown on Figure 5, conflicts with the high-speed read out time of CMOS.

For kinetic measurements in the near-UV, Visible and near-IR spectral ranges (300−1000 nm), we recommend fast CMOS arrays as the best option due to their speed advantage over CCD arrays. However, ICCD cameras are more sensitive to weak signals, making them ideal for multipass systems where light intensity is generally low. In addition, our current setup is also capable of deep-UV measurements for future studies.

1.3.3—Data Acquisition

All components of the instrument are controlled and logged by LabView 2018. All gas flows, pressures and temperatures are continuously monitored through a National Instruments cDAQ-9174 controller at 1 Hz. The software also controls the data collection from the PMT and ICCD. The ICCD gate delay and photolysis laser trigger times are controlled through a digital delay generator (BNC model 565), and the software adjusts the ICCD delay times automatically to record spectra at several times post-photolysis.

During a typical data acquisition cycle with multiple ICCD delay times, the data from the PMT is continuously collected, which results in high signal-to-noise kinetic time profiles. For example, if five ICCD delay times are chosen with 200 photolysis laser shots each, a PMT dataset of 1000 co-added time traces are collected.

1.4—Instrument Characterization

1.4.1—Photolysis Laser “Background” Absorption

When the excimer laser fires, a positive absorption “background” is observed by both the PMT and ICCD detectors, caused by the photolysis laser interacting with the long-pass optic used to protect the White cell field optic. The “background” signal is broad (Figure 6A), decays with a fast and slow component (Figure 6B), and the intensity is proportional to the photolysis laser power (Figure 6C). The background absorption intensity is increased when the non-coated side of the long-pass optic faces the excimer laser beam, leading us to believe the observed signals are due to interaction of the high energy UV laser light with the optic substrate (figure S5). To account for this, a background spectrum is collected before experiments for subtraction, with the excimer laser firing and only bath gas present in the reactor. In other words, the reported spectra and temporal profiles were obtained by direct subtracting the background from the signals, recorded with precursors in the reactor. We are unaware of this phenomenon in the literature, but assume that similar systems using filters to separate photolysis and probe light beams might encounter this. At the time of writing, we have not tested the performance of any different optics.

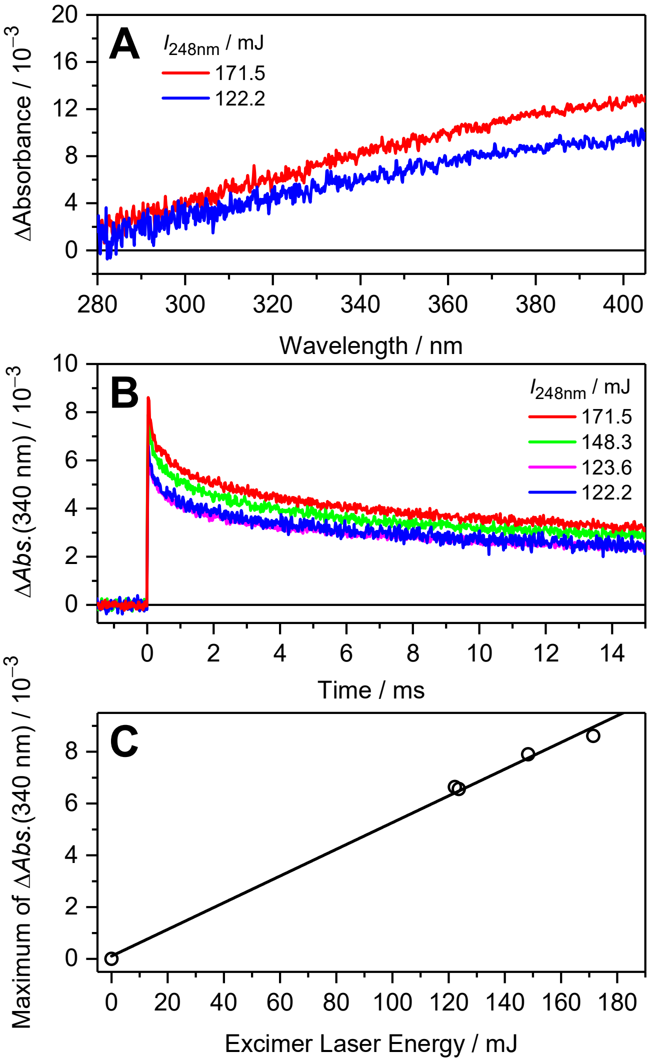

Figure 1.6. Observed excimer laser-induced background absorption from the long-pass filter used to separate photolysis and probe light beams. Data shown were collected with the uncoated side of the long-pass filter facing the incident excimer beam. (A) The background absorption spectrum induced by the excimer laser and the long-pass filter at delay time 50 μs, (B) The temporal profile of the background absorption recorded using the PMT recorded at different excimer laser energies, (C) Plot of the maximum absorption intensity from the PMT as a function of excimer laser energy; the solid line represents the linear fit to the data.

1.4.2—Purge Characterization

The effective single-pass absorption path length for the reactor is 45 ± 2 cm, and defined by the physical distance between the "purge arm" gas exhausts, as shown in Figure 1. The purge flow rates, F_{purge}, are set to 5% of the total gas flow rate, F_{total}, such that $F_{\mathrm{purge}}/F_{\mathrm{total}} = 0.05$ across all pressures. Purge and main reactor flow gases mix in the regions close to the reactor exhausts, which could alter the effective pathlength. Experiments using NO_2 as a known absorber (Figure 7) show the effective single-pass absorption path length converges to 43.6 ± 4.3 cm when $F_{\mathrm{purge}}/F_{\mathrm{total}} > 0.05$, validating the physical pathlength, within the uncertainties of the empirical measurement. As a result, we estimated the effective gas volume, $V_{\mathrm{eff}} \approx 565$ cm^3 (ID = 4 cm, $L = 45$ cm), for controlling the gas residual time in the reactor.

It is important to highlight that the White cell-type multipass system provides a total path length $L_{\mathrm{total}} = 14$ m over ten passes. However, the effective gas region only encompasses a segment of the probed beam path and is located near the field mirror (as depicted in Figure 3). Consequently, the single-pass absorption path length is limited to 45 cm, yielding an effective absorption path length $L_{\mathrm{eff}} = 4.5$ m for ten passes. This particular geometry offers the benefit of permitting a smaller divergence angle for the photolysis laser, maximizing the filling of the reactor and reducing the influences of inhomogeneous radical formations on kinetic measurements.

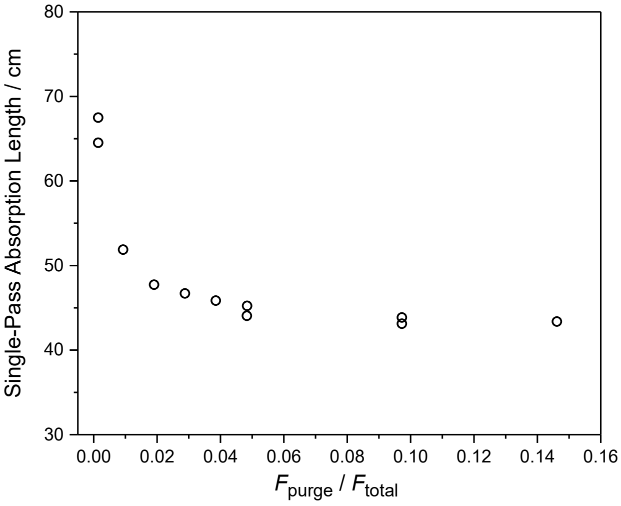

Figure 1.7. Estimation of the effective absorption path length as a function of the purge:total flow ratios ($F_{\mathrm{purge}}/F_{\mathrm{total}}$) recorded with ten probe-beam passes at 50 Torr, 292 K and F_{total} = 8200 sccm. Spectra of NO_2 were measured between 280 – 405 nm, and pathlengths were derived using the JPL recommended absorption cross-section (6.13×10^{-19} $cm^{2,}$ 380–410 nm, <3%) and $[NO_2] = (5.3\pm0.1)\times10^{14}$ cm^{-3}.[17] Uncertainties in the measurement are primarily from the flow stability.

We observe increased protection of the windows when the main reactor gas flow was introduced into the center and removed at either end. When the main gas flow is introduced at one end of the reactor and removed at the opposite end (a more typical approach), we observe increased deposition of photolysis products on the window closest to the gas inlet, even with the purges flowing. A low-level flow simulation using Solidworks 2021 (see SI for details) predicted only a small amount of the main flow will mix with the purge flow and that this mixing mainly occurs along the walls of the reactor. Interestingly, these simulations also highlight that that the gas input flow causes some turbulent mixing in the gas entrance region, with a uniform flow to the pump out region. The flow simulations also support our observations in the more typical flow reactor case, with input gas and purge gas mixing close to the purge arm output. Despite the low-level calculation, this simulation provides some useful insight into the mixing dynamics of a typical flow tube reactor and supports the observations of this work.

1.4.3—Axial Temperature Profile

1.4.3.1—Thermocouple Measurement

Temperatures are controlled in the reactor using a flow of chilled methanol around an external jacket that covers the reactor. The axial temperature profile of the flow reactor (i.e., in the direction of gas flow) is shown in Figure 8 for the lowest achievable temperature at 239 K. Reactor temperatures shown in Table S1 are determined as the mean temperature across the effective absorption pathlength (45 cm, or ± 22.5 cm in Figure 8), and respective uncertainties are the standard deviation to 2σ. As can be seen in the uncertainties shown in Table S1, the temperature profiles are more stable closer to room temperature (~293 K). The calibration curve to convert the chilled liquid temperature set-point to the respective reactor gas temperature is shown for reference in Figure S7. Based on the worst-case dataset at 235 K, we assign a conservative uncertainty on the overall temperature profile of ± 2 K (2σ).

The measured temperature is higher at input of the reactor (central region, 0 cm), because of the non-cooled O-ring connector between the precooled inlet and the reactor gas inlet. The measured temperature is also higher at the two ends of the reactor due to the mixing of cooled gas with room temperature purge flow gas. As shown in Figure 8, the distance between the warmer extremities agrees well with the effective single-pass absorption path length, which highlights negligible impact on the pathlength with decreasing temperature. The temperature profile can be made more uniform by increasing the total gas flow rate, which we suggest is because of a shorter residence time in the pre-cooled inlet interface region.

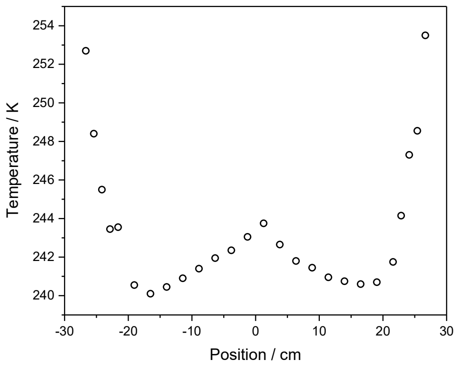

Figure 1.8. The temperature profile in the flow reactor under 500 Torr at temperature set-point = 235 K. Positions shown are relative to the center of the reactor (gas inlet) and the mean temperature here was determined to be = 239 ± 2 K. Temperatures were measured using a thermocouple probe introduced at one end of the reactor, replacing a window with an ultra-torr flange. The probe was kept as close to the center of the reactor diameter cross-section as possible. Temperatures were logged for 1 minute in each position, and the position was changed by sliding the probe through the reactor.

1.4.3.2—Equilibrium Constant between NO_2 and N_2O_4

To validate the temperature profile measurement, the thermocouple measurements are compared to spectroscopic NO_2/N_2O_4 measurements of the $NO_2 \rightleftharpoons N_2O_4$ equilibrium constant, K_p, between 239 - 267 K in Figure 9. Using this method, the error in temperature is estimated to be ±2 K at 243 K and ±1 K at 263 K, which includes the 30 % uncertainty in the derived K_P. Nevertheless, our measurements of K_p agree with the literature.

Following the literature,[18] we define the equilibrium constant, K_P, for the dissociation direction.

$$K_P = \frac{[NO_2]^2}{[N_2O_4]}$$

The UV-Vis spectrum of NO_2 has been well studied.[21–23] Measurements were conducted in a continuous flow of bath gas at 50.0 Torr. Samples of $[NO_2] = 1.3\%$ in N_2 were prepared by mixing 81.4 Torr of NO (Matheson, 99.5%) and 1324 Torr of O_2 (Airgas, 99.994%), then balanced to 6100 Torr in N_2, in a stainless-steel cylinder.[24] At each temperature, a small initial concentration of NO_2 was introduced into the reactor to record a reference NO_2 spectrum with minimized influence of N_2O_4. With N_2O_4 present (i.e., at higher $[NO_2]$), the spectrum shows a clear overlap between the fine structured spectrum of NO_2 and the broader feature from N_2O_4, which peaks near 340 nm (Figure 9A).[18] By fitting the NO_2 spectrum structures outside of the absorbance window for N_2O_4 (i.e., $\lambda > 400$ nm), $[NO_2]$ in the flow reactor was obtained. Using the mass balance, we obtain the relation between the initial NO_2 concentration, $[NO_2]_0$, and $[NO_2]$ and $[N_2O_4]$, where $[NO_2]_0$ was estimated from the NO_2 sample concentration and the ratio of flows and the reactor pressure.

$$[NO_2]_0 = [NO_2] + 2[N_2O_4] = [NO_2] + \frac{2}{K_P}[NO_2]^2$$

Figure 9B shows that the $[NO_2]_0$ as function of the $[NO_2]$ in the reactor, which follows a second-order polynomial at $T < 267$ K. The equilibrium constants could be obtained from the fit. However, as figure S14 shows that the difference spectrum at 267 K still possess small signal of N_2O_4. The equilibrium constant obtained from Figure 9B could be used to derive the absolute cross-section of N_2O_4. Plotting the average absorbance near 340 nm against $[NO_2]$, we found a pure quadratic function can well fit the data at different temperatures (figure S15). By assuming the N_2O_4 cross-section near 340 nm = 6.6×10^{-19} cm^2 (reported by Harwood et al.[18]), and an absorption length $L = 450$ cm, we derived the equilibrium constant at 267K. Comparison between equilibrium constant obtained from two methods are plotted in figure S16, and show excellent agreement, increasing confidence in the temperature profile measurements.

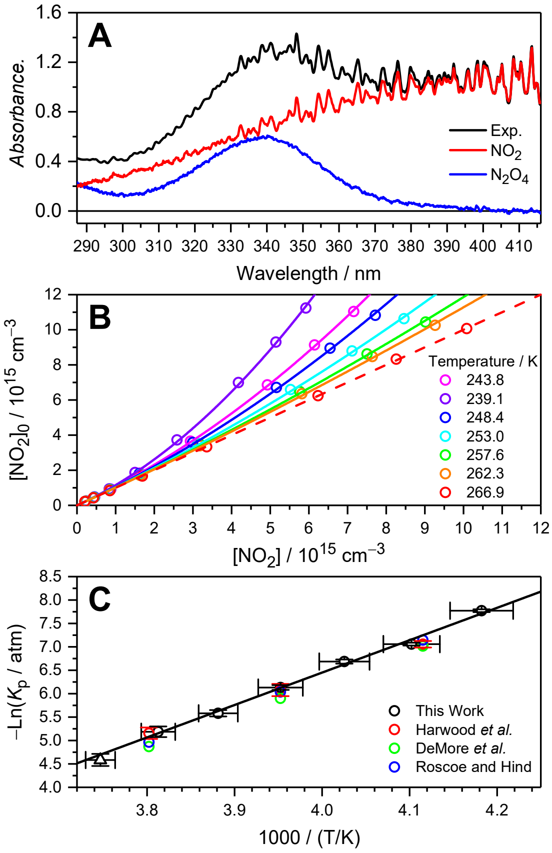

Figure 1.9. (A) The representative absorption spectrum recorded at 239 K. The N_2O_4 spectrum (blue) was obtained by subtracting the scaled NO_2 spectrum (red) recorded at low $[NO_2]$ to match the fine structure at $\lambda > 400$ nm. (B) Plot of the initial NO_2 concentration against the observed NO_2 concentration under different temperatures. The solid lines show the second-order polynomial fitting. The dashed red line indicates the 1-to-to1 relation. (C) The van't Hoff plot of the equilibrium constant and comparison with the literatures.[18–20] The error in temperature shows the maximum difference of inhomogeneity.

1.4.4—Chemical Kinetics System Characterization

1.4.4.1—CH_2OO Yields at Different Total Pressure

The photolysis of $CH_2I_2/O_2/N_2$ mixtures has been well studied since 2012,[25] since CH_2I_2 was identified as convenient precursor for the simplest Criegee intermediate, CH_2OO. Criegee intermediates have been shown to undergo fast reaction with SO_2 and could play important roles in the formation of secondary organic aerosols.[25–27] The CH_2OO intermediate is an isoelectronic molecule of ozone,[28] and as such, has a large absorption cross-section with a peak $\sigma_{CH2OO} = 1.2\times10^{-17}$ cm^2 near 340 nm with a weak vibrational progression towards the red end of the spectrum.[29] Based on the large absorption cross–section and known reaction rates with, e.g., SO_2 and NO_2, CH_2OO is an ideal candidate for characterization measurements in the UV-Vis spectroscopy.

The generation of CH_2OO from reaction between CH_2I and O_2 has been studied and the pressure dependent yields have been measured.[30] The CH_2I radical reacts with O_2 to form chemically activated ICH_2OO^*, which can either dissociate to form CH_2OO + I or, when the total pressure is higher than 60 Torr, be stabilized to form ICH_2OO. The competition between these two processes causes the CH_2OO yield to decrease with increasing reactor pressure, as observed experimentally. At pressures < 60 Torr, although the stabilization of ICH_2OO^* is dramatically reduced, the stabilization of CH_2OO is also less efficient. Chemically activated CH_2OO undergoes unimolecular reaction which causes the observed CH_2OO yields to decrease, as shown in scheme 1.

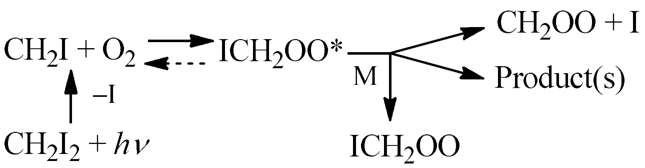

Scheme 1.1. Reaction mechanism of the formation of the simplest Criegee intermediates.

In our experiments, 5 Torr of O_2 was used to convert the CH_2I radical into CH_2OO within 10 μs ($k_{CH2I+O2} = 1.5\times10^{-12}$ cm^3 s^{-1}).[30] The CH_2I_2 was introduced to the reactor by flowing N_2 through a bubbler containing CH_2I_2 liquid . A Teflon needle valve (Gilmont instruments, GM-7100) was placed at exit of the bubbler to control the pressure. This served to both stabilize the CH_2I_2 concentration exiting the bubbler which can be perturbed by vigorous bubbling, and also to control the fraction of the bubbler flow that comprises CH_2I_2 vapor. The concentration of CH_2I_2 (Sigma-Aldrich, >99%) was directly measured in the reactor before addition of co-reactants and without the photolysis laser.

The spectra recorded at t = 50 μs were fit with the reported CH_2OO[29], CH_2I_2[31] and IO[32] literature spectra (Figure 10A), thus we could derive the yield of CH_2OO. Figure 10A shows the sample spectra across three different total N_2 pressures and the respective component spectra. The spectra in Figure 10 were averaged over 384 photolysis laser shots. The noise level is about $\pm1\times10^{-3}$ in absorbance, corresponding to a detection limit of CH_2OO about 3.7×10^{11} molecule cm^{-3} with an effective absorption length L = 450 cm. We found that the signal of CH_2OO, indeed, becomes smaller at higher pressures. Our observed yield of CH_2OO as a function of total reactor pressure (P_{total}) is shown in Figure 10B, and is in agreement with the literature.[30]

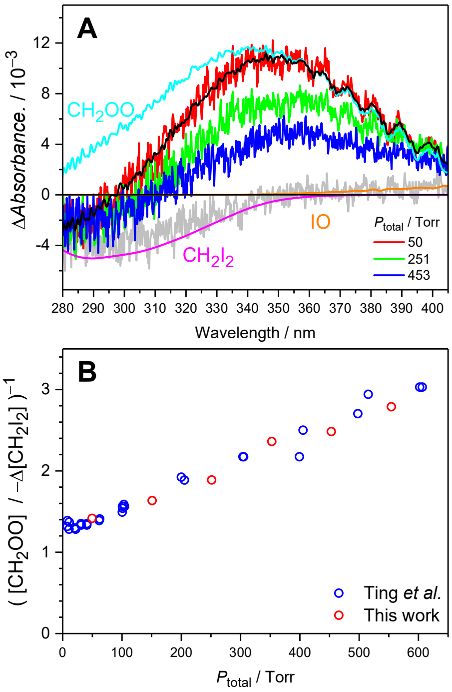

Figure 1.10. (A) Representative spectrum of the $CH_2I_2/O_2/N_2$ photolysis system recorded at 50 μs under different total pressures. The 50 Torr spectrum (red) was decomposed into contributions from CH_2OO (cyan), ΔCH_2I_2 (magenta) and IO (orange). The spectrum at long time (gray) shows the depletion of CH_2I_2, which agrees with the contribution at short delay time. (B) The pressure dependence of reciprocal of the CH_2OO yields (red) and comparison with the literature (blue).[30]

1.4.4.2—CH_2OO Reaction with SO_2 and NO_2

Previous studies have demonstrated that the reactions of CH_2OO with SO_2 and NO_2 reach their high-pressure limits above 10 Torr N_2 near room temperautre.[33] We performed kinetic measurements of $CH_2OO + SO_2$ and $CH_2OO + NO_2$ at 50 Torr and 295 K. Samples of NO_2 were prepared identically to those described in section 3.3.2. The 0.75 % SO_2 samples were prepared from a mixture of 38 Torr pure SO_2 (Airgas, 99.9%, UN1079) with N_2 to 5077

Torr total pressure. Figure 11 shows the sample spectra of the $CH_2I_2/O_2/N_2$ photolysis system in the absence (A) and presence (B) of SO_2. As anticipated, we observed that the signal of CH_2OO decayed faster in the presence of SO_2. We attribute the negative baseline observed at $\lambda < 350$ nm in both experiments to the photolytic depletion of CH_2I_2.

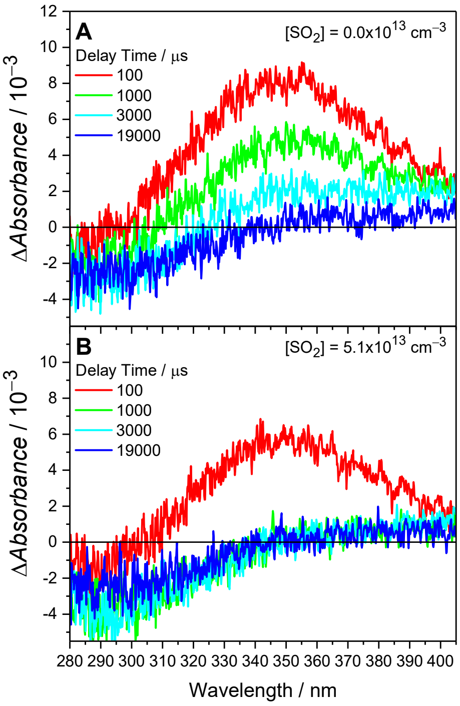

Figure 1.11. Representative spectra measured in the $CH_2I_2/O_2/N_2$ photolysis system with (A) and without (B) SO_2 at 50 Torr, 295 K.

Figure 12A shows the temporal absorbance profiles under different SO_2 concentrations recorded using the PMT detector (solid lines) and the ICCD at three discrete times (open circles). The data points recoded with the ICCD are in excellent agreement with the PMT temporal profiles. The data shown in Figure 12A is a result of averaging over 386 photolysis laser shots for each spectrum (4 spectra total) and 1544 laser shots (386×4) for each temporal profile. Considering the noise level in the PMT temporal profile and a typical experimental average over 1240 photolysis laser shots, the minimal observable absorption is ~6.5×10^{-4} (3 standard deviations of the noise), corresponding to a detection limit of $CH_2OO = 1.2 \times 10^{11}$ molecule cm^{-3} with an effective absorption path length, L = 450 cm.

Experiments were performed under pseudo-first-order condition, such that $[SO_2] >> [CH_2OO]$ and so we use an exponential function to model the temporal behavior. A baseline term, B_0, is added to model the depletion of CH_2I_2, which is observed as a constant offset on these short timescales (< 10 ms) Without SO_2, CH_2OO decays due the self-reaction and reaction with other species (such as I atoms); thus, we observe a deviation from the exponential fit for the $[SO_2] = 0$ case. This deviation has been observed previously and shown to not significantly affect the determination of k_0, and therefore the bimolecular rate coefficient.[4]

$$-\frac{d[\mathrm{CH_2OO}]}{dt} = \left(k_0 + k_{\mathrm{SO2}}[\mathrm{SO_2}]\right)[\mathrm{CH_2OO}] = k'[\mathrm{CH_2OO}]$$

$$Abs.(340\mathrm{nm}) = A_0 e^{-k't} + B_0$$

Figure 12B shows the bimolecular plot for $CH_2OO + SO_2$, and the slope yields a rate coefficient $k_{SO2} = (4.11 \pm 0.12) \times 10^{-11}$ cm^3 $molecule^{-1}$ s^{-1} which is in excellent agreement with the literature, $(4.1 \pm 0.3) \times 10^{-11}$ cm^3 $molecule^{-1}$ s^{-1}.[6,25,34] Quoted uncertainties are ±2σ, and error propagation is discussed in the supporting information. Figures S24-S26 show the spectra and temporal profiles for CH_2OO in the presence of NO_2, and the bimolecular plot (figure S23) yields $k_{NO2} = (1.77 \pm 0.11) \times 10^{-12}$ cm^3 $molecule^{-1}$ s^{-1}, again in good agreement with the literature, $(1.5 \pm 0.5) \times 10^{-12}$ cm^3 $molecule^{-1}$ s^{-1}.[33]

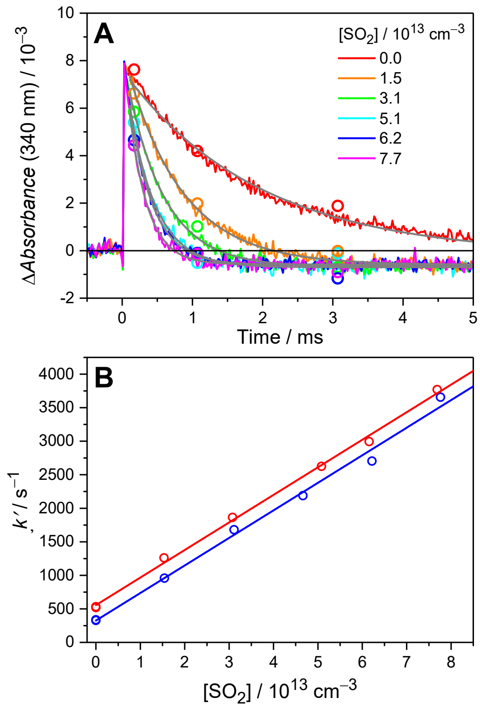

Figure 1.12. (A) The temporal profiles near 340 nm for the $CH_2I_2/O_2/N_2$ photolysis system at 50 Torr. The opened circles represent the absorption intensity recorded using the ICCD (Figure 11). The observed negative baselines are due to the photolytic depletion of CH_2I_2. The gray lines show the fit to an exponential function. (B) Pseudo-first-order plot of the observed decay rates, *k*', against $[SO_2]$. The red and blue datasets show measurements using $[CH_2I_2]_0 = 3.2\times10^{13}$ and 1.7×10^{13} molecule cm^{-3}, respectively. The linear regression yields the $CH_2OO + SO_2$ rate coefficient, $k_{SO2} = (4.11 \pm 0.12)\times10^{\ 11}$ cm^3 $molecule^{-1}$ s^{-1}.

1.4.5—Comparison with Literature Apparatus

Various research groups have developed experimental apparatus to study chemical kinetics in the UV-Vis region, specifically looking at Criegee intermediates. While the systems have general similarities (i.e., they all use multipass optics, laser photolysis and UV/Vis light detection), they differ in their design of these similar features.

One such apparatus uses a prism and large spherical mirror to form a unique multipass system with an effective absorption length of approximately 400 cm.[11] The combination of prism and large spherical mirror enables excellent overlap between the photolysis and probe beams. Different from our apparatus, the probe beam after the multipass cell is either directing into a spectrometer equipped with a camera or towards a balanced photodiode detector. The spectral measurements employ a range of cameras, including an ICCD,[29] Electron Multiplication CCD[35] (EMCCD, sequential imagine time resolution = 600 μs, limited by the read out speed) and an ultrafast CMOS camera[36] (sequential imagine time resolution = 200 μs, limited by the exposure time and data transfer rate), which are similar to our configuration, with similar sensitivities and detection limits. The balanced photodiode detector uses a band-pass filter (10 nm FWHM) to enable kinetic trace measurements with a superior signal-to-noise ratio (3 standard deviation of noise is $\sim 1\times10^{-4}$ in absorbance for 120 laser shots), decreasing the detection limit another order of magnitude compared to the spectral measurements. The optical filter/photodiode method leads to possible complications with measuring time-dependent traces at multiple wavelengths (i.e., interfering species decaying at different time constants within the 10 nm window). Additionally, their configuration does not allow for simultaneous collection of spectra and photodiode data; although it should be noted that based on the S/N of the photodiode, kinetic time traces can be recorded within 120 laser shots average.

Another multipass UV/Vis system[10] has been developed recently, named TRUVAS (Time-Resolved UV Absorption Spectrometer). The apparatus uses a unique rectangular shaped reactor that can operate over a wide range of pressures (10 – 800 Torr) at room temperature. The multipass optical arrangement is also unique, using fourteen independently aligned small circular mirrors, which can enable pathlengths up to 700 cm. Light is directed towards a fiber collimator that channels the light exciting the multipass system towards a spectrograph with a fast read CCD line camera (1 kHz). The system can measure wavelengths from ~200 – 800 nm simultaneously at a time resolution of ~780 μs (limited by the CCD integration time). While maintaining excellent signal-to-noise and detection limits, the system is more limited in the UV region. Fiber optic coupling of the probe light is convenient for spectrograph alignment, but results in light losses compared to direct light coupling. Additionally, while unique, the optical arrangement is more complex than a conventional multipass White cell arrangement and the cell is limited to studies at room temperature.

The three other apparatus discussed here use optical cavities, either single wavelength cavity ringdown[9] or broadband cavity-enhanced absorption.[6,7] The first uses broadband cavity-enhanced absorption,[5] with a temperature-controlled cell (room temperature up to 1000 K)[5] and a unique rotating mirror and a custom grating/CCD camera arrangement.[5,6] The rotating mirror is synchronized to the excimer laser pulse and rotates at a speed such that the image sweeps across the CCD, providing simultaneous temporal and spectral data (1.2 μs per pixel)[5]. This arrangement delivers remarkable time resolution and an impressively low detection threshold due to the optical cavity (a factor of ~10 enhancement in detection limit versus a multipass system). However, the effective absorption path length depends on the target concentrations, and careful treatment of the calibration factors and data analysis are needed. Additionally, this arrangement results in very low light intensity at each pixel and therefore many laser shots (>2000) for a suitable S/N is required, which presents a source of uncertainty based on the stability of chemical flow systems.

The second broadband cavity-enhanced absorption based instrument can also be temperature controlled (296 – 600 K) and uses a more conventional optical setup, directing output light from the cavity towards a spectrograph fitted with a fast CMOS array.[7] This arrangement covers a spectral range of ~160 nm (centered at 370 nm) and a sequential imagine time resolution 50 μs (20 kHz) owing to the fast readout speed of the CMOS. By directing all of the output light towards the CMOS array, they can achieve better detection limits that the other cavity-enhanced systems, at the expense of time resolution.[6] The complexity of cavity calibration remains in this experiment, and the CMOS array is only one pixel tall, so light filling the entrance slit overfills the array. However, this system has low flexibility for exploring different wavelength due to the CMOS detector (>30% quantum efficiency within 300–875 nm) and the high-reflectance broadband mirrors.

Finally, a monochromatic, pulsed cavity-ringdown apparatus has been developed and applied to the kinetics of Criegee intermediates at 355 nm.[8,37] The glass cell is jacketed and can be temperature controlled between 240 and 320 K.[38,39] The overall pathlength of the optical cavity is limited by the mirror reflectance at 355 nm (>99.9%)[8] which results in a short ring-down time and limits the detection sensitivity. By measuring the difference of ring-down time with and without samples, the data analysis procedure is easy compared with the broadband enhanced cavity apparatuses as only the overlap region of the probe and photolysis laser beams needs to be characterized. However, as the system operates only at a single wavelength, it is susceptible to interfering absorptions from secondary species

Our system strikes a harmonious balance amongst these other methods, offering a simplified optical design that is easy to align with reasonable signal-to-noise and detection limits. Due to the light splitting method and intensified detectors, our time resolution is comparable to other systems, but with a much shorter data averaging time, reducing the uncertainty from flow system fluctuations that could perturb other systems.

1.5—**Conclusions**

We introduce a new UV-Vis, pulsed-photolysis experimental apparatus for spectroscopy and chemical kinetic measurements. As shown, the system comprises a jacketed glass reactor that can operate over the 239 – 293 K temperature and 10 – 550 Torr pressure range. Inside the reactor, the UV pulsed-photolysis excimer laser beam is combined with the UV-Vis broadband probe light from a LDLS to measure the spectra and chemical kinetics of photochemical products.

Unique to this apparatus is the arrangement of White-cell-type multipass optic system, which has a 20 mm gap between the objective mirrors, allowing the photolysis laser beam to fully overlap with the UV-Vis probe beam inside the reactor. The setup allows better estimation on the effective absorption length, compared to an off-axis type apparatus.

Additionally, this arrangement reduces the number of dichroic optics in the probe-beam path from 2 to 1, compared to other co-aligned beam setups, which improves the flatness of the probed light and increases the probe-beam output light intensity from the White cell. Despite the reduction in light intensity due to the optics in the probe-beam path, the advantage of this optical arrangement is in the ease of alignment and well-defined absorption pathlength, compared to off-axis type experiments. Finally, also unique to this apparatus is the method of light collection onto an ICCD and PMT using a "half-height" mirror, allowing for simultaneous spectra and temporal profile collection. This method leverages the wavelength specificity of the monochromator, compared to optical filters, with the increased gain of a PMT, over a photodiode.

The theoretical and empirical characterization of the gas flow inside the reactor shows that, by introducing gas into the center and pumping it out at either end, only a small purge flow (>5% of total flow) is required to protect windows from contamination. Additionally, the flow setup displays a well-defined mixing region of the purge and main gas flows, resulting in a better estimation of absorption path length based on the physical distance between the two gas exhaust ports.

The reactor temperature profile across the probe-beam pathlength is ±2 K, defined by the worst-case at 239 K. Though a pre-cooled inlet is installed on the reactor, the small, uncooled distance between the condenser and the main flow reactor causes the input gas to have ~1.5 K higher temperature at the coldest temperature setpoint (239 K). The temperature profile is validated by measurements of the N_2O_4 equilibrium constant. Despite the ±2 K temperature profile, the measured equilibrium constant agrees with previous literature, validating the mechanical measurement (within uncertainty).

The overall performance of the reactor is presented through the measured spectra and kinetics of the simplest Criegee intermediate, CH_2OO, and its reactions with SO_2 and NO_2. The measured spectra and kinetics are in good agreement with the literature, validating the performance of this new apparatus. Both the spectra and temporal profile are recorded simultaneously, and under typical experiment conditions, we estimate a detection limit of

2×10^{-3} and 1×10^{-3} in absorbance for spectrum and temporal profile measurements, respectively.

1.6—References

1. Heinz-Helmut Perkampus. *UV-VIS Spectroscopy and Its Applications*. (Springer US, 1992).
2. Donald A. McQuarrie & John D. Simon. Molecular Spectroscopy. in *Physical Chemistry : a Molecular Approach* (Sausalito, Calif. :University Science Books, 1997).
3. Schoonheydt, R. A. UV-VIS-NIR spectroscopy and microscopy of heterogeneous catalysts. *Chem. Soc. Rev.* **39**, 5051 (2010).
4. Jr-Min Lin, J. & Chao, W. Structure-dependent reactivity of Criegee intermediates studied with spectroscopic methods. *Chem. Soc. Rev.* **46**, 7483–7497 (2017).
5. Sheps, L. & Chandler, D. *Time-Resolved Broadband Cavity-Enhanced Absorption Spectroscopy for Chemical Kinetics.* SAND2013-2664, 1095949, 463465 https://www.osti.gov/servlets/purl/1095949/ (2013) doi:10.2172/1095949.
6. Sheps, L. Absolute Ultraviolet Absorption Spectrum of a Criegee Intermediate CH_2 OO. *J. Phys. Chem. Lett.* **4**, 4201–4205 (2013).
7. Peltola, J., Seal, P., Inkilä, A. & Eskola, A. Time-resolved, broadband UV-absorption spectrometry measurements of Criegee intermediate kinetics using a new photolytic precursor: unimolecular decomposition of CH_2 OO and its reaction with formic acid. *Phys. Chem. Chem. Phys.* **22**, 11797–11808 (2020).

8. Chhantyal-Pun, R., Davey, A., Shallcross, D. E., Percival, C. J. & Orr-Ewing, A. J. A kinetic study of the CH_2OO Criegee intermediate self-reaction, reaction with SO_2 and unimolecular reaction using cavity ring-down spectroscopy. *Phys. Chem. Chem. Phys.* **17**, 3617–3626 (2015).
9. Buras, Z. J., Elsamra, R. M. I., Jalan, A., Middaugh, J. E. & Green, W. H. Direct Kinetic Measurements of Reactions between the Simplest Criegee Intermediate CH_2OO and Alkenes. *J. Phys. Chem. A* **118**, 1997–2006 (2014).
10. Lewis, T., Heard, D. E. & Blitz, M. A. A novel multiplex absorption spectrometer for time-resolved studies. *Review of Scientific Instruments* **89**, 024101 (2018).
11. Chao, W., Hsieh, J.-T., Chang, C.-H. & Lin, J. J.-M. Direct kinetic measurement of the reaction of the simplest Criegee intermediate with water vapor. *Science* **347**, 751–754 (2015).
12. Zhu, H. & Blackborow, P. LDLS sheds light on analytical-sciences applications. *LaserFocusWorld* 3 (2011).
13. Baum, W. A. & Dunkelman, L. Ultraviolet Radiation of the High Pressure Xenon Arc*. *J. Opt. Soc. Am.* **40**, 782 (1950).
14. Su, M.-N. & Jr-Min Lin, J. Note: A transient absorption spectrometer using an ultra bright laser-driven light source. *Review of Scientific Instruments* **84**, 086106 (2013).
15. Su, Y.-T., et al. Extremely rapid self-reaction of the simplest Criegee intermediate CH2OO and its implications in atmospheric chemistry. *Nature Chem* **6**, 477–483 (2014).

16. Chao, W., Jones, G. H., Okumura, M., Percival, C. J. & Winiberg, F. A. F. Spectroscopic and Kinetic Studies of the ClSO Radical from Cl_2 SO Photolysis. *J. Am. Chem. Soc.* **144**, 20323–20331 (2022).
17. Burkholder, J. B., et al. JPL Publication 19-5. Chemical Kinetics and Photochemical Data for Use in Atmospheric Studies. *JPL Publication* **19–5**, 2–7 (2020).
18. M. H. Harwood & R. L. Jones. Temperature dependent ultraviolet-visible absorption cross sections of NO2 and N2O4: Low-temperature measurements of the equilibrium constant for 2NO2 and N2O4. *Journal of Geophysical Research* **99**, 22955–22964 (1994).
19. DeMore, W B, et al. Chemical kinetics and photochemical data for use in stratospheric modeling. *JPL Publication* (1992).
20. Roscoe, H. K. & Hind, A. K. The Equilibrium Constant of N O 2 with N204 and the Temperature Dependence of the Visible Spectrum of NO2: A Critical Review and the Implications for Measurements of NO2 in the Polar Stratosphere. *Journal of Atmospheric Chemistry* **16**, 257–276 (1993).
21. Ndengué, S., Quintas-Sánchez, E., Dawes, R. & Osborn, D. The Low-Lying Electronic States of NO_2: Potential Energy and Dipole Surfaces, Bound States, and Electronic Absorption Spectrum. *J. Phys. Chem. A* **125**, 5519–5533 (2021).
22. Nizkorodov, S. A., Sander, S. P. & Brown, L. R. Temperature and Pressure Dependence of High-Resolution Air-Broadened Absorption Cross Sections of NO_2 (415−525 nm). *J. Phys. Chem. A* **108**, 4864–4872 (2004).

23. A. C. Vandaele, et al. High-resolution Fourier transform measurement of the NO2 visible and near-infrared absorption cross sections: Temperature and pressure effects. *Journal of Geophysical Research* **107**, 4348 (2002).
24. Winiberg, F. A. F., Zuraski, K., Liu, Y., Sander, S. P. & Percival, C. J. Pressure and Temperature Dependencies of Rate Coefficients for the Reaction OH + NO_2 + M → Products. *J. Phys. Chem. A* **124**, 10121–10131 (2020).
25. Welz, O., et al. Direct Kinetic Measurements of Criegee Intermediate (CH2OO) Formed by Reaction of CH2I with O2. *Science* **335**, 204–207 (2012).
26. Boy, M., et al. Oxidation of SO_2 by stabilized Criegee intermediate (sCI) radicals as a crucial source for atmospheric sulfuric acid concentrations. *Atmospheric Chemistry and Physics* **13**, 3865–3879 (2013).
27. Percival, C. J., et al. Regional and global impacts of Criegee intermediates on atmospheric sulphuric acid concentrations and first steps of aerosol formation. *Faraday Discuss.* **165**, 45 (2013).
28. Osborn, D. L. & Taatjes, C. A. The physical chemistry of Criegee intermediates in the gas phase. *International Reviews in Physical Chemistry* **34**, 309–360 (2015).
29. Ting, W.-L., Chen, Y.-H., Chao, W., Smith, M. C. & Lin, J. J.-M. The UV absorption spectrum of the simplest Criegee intermediate CH_2OO. *Phys. Chem. Chem. Phys.* **16**, 10438–10443 (2014).
30. Ting, W.-L., et al. Detailed mechanism of the CH_2I + O_2 reaction: Yield and self-reaction of the simplest Criegee intermediate CH_2OO. *The Journal of Chemical Physics* **141**, 104308 (2014).

31. Mössinger, J. C., Shallcross, D. E. & Anthony Cox, R. UV–VIS absorption cross-sections and atmospheric lifetimes of CH2Br2, CH2I2 and CH2BrI. *Faraday Trans.* **94**, 1391–1396 (1998).
32. Peter Spietz, Juan Carlos G´ omez Mart´ın, & John P. Burrows. Spectroscopic studies of the Isub2subOsub3sub photochemistry Part 2. Improved spectra of iodine o.pdf. *Journal of Photochemistry and Photobiology A: Chemistry* **176**, 50–67 (2005).
33. Stone, D., Blitz, M., Daubney, L., Howes, N. U. M. & Seakins, P. Kinetics of CH_2OO reactions with SO_2, NO_2, NO, H_2O and CH_3CHO as a function of pressure. *Phys. Chem. Chem. Phys.* **16**, 1139–1149 (2014).
34. Liu, Y., Bayes, K. D. & Sander, S. P. Measuring Rate Constants for Reactions of the Simplest Criegee Intermediate (CH_2OO) by Monitoring the OH Radical. *J. Phys. Chem. A* **118**, 741–747 (2014).
35. Lin, Y.-H., Li, Y.-L., Chao, W., Takahashi, K. & Lin, J. J.-M. The role of the iodine-atom adduct in the synthesis and kinetics of methyl vinyl ketone oxide—a resonance-stabilized Criegee intermediate. *Phys. Chem. Chem. Phys.* **22**, 13603–13612 (2020).
36. Lin, Y.-H., Yin, C., Takahashi, K. & Lin, J. J.-M. Surprisingly long lifetime of methacrolein oxide, an isoprene derived Criegee intermediate, under humid conditions. *Commun Chem* **4**, 12 (2021).
37. Chhantyal-Pun, R., et al. Direct Measurements of Unimolecular and Bimolecular Reaction Kinetics of the Criegee Intermediate $(CH_3)_2COO$. *J. Phys. Chem. A* **121**, 4–15 (2017).

38. Chhantyal-Pun, R., et al. Experimental and computational studies of Criegee intermediate reactions with NH_3 and CH_3NH_2. *Phys. Chem. Chem. Phys.* **21**, 14042–14052 (2019).

39. McGillen, M. R., et al. Criegee Intermediate–Alcohol Reactions, A Potential Source of Functionalized Hydroperoxides in the Atmosphere. *ACS Earth Space Chem.* **1**, 664–672 (2017).

Chapter 2—Spectroscopic and Kinetic Studies of the ClSO Radical from Cl_2SO Photolysis

This chapter is reprinted and adapted with permission from J. Am. Chem. Soc. 2022, 144, 20323 - 20331. Copyright 2022, American Chemical Society.

2.1—Abstract

Thionyl chloride (Cl_2SO) serves as a common Cl atom source in widespread applications of chlorine chemistry though little is known about the reactivity and spectroscopy of the ClSO radical after a Cl–S bond cleavage. We performed a pulsed-laser photolysis experiment to detect ClSO from Cl_2SO photolysis at 248 nm in a gas flow reactor by a time-resolved UV-Vis transient ab-sorption spectroscopy. A few chemical tests, using I_2 and NO_2, suggested the structured absorption band between 260–320 nm belonged to ClSO radical and the termolecular ClSO + Cl + M → Cl_2SO association reaction occurred. From EOMIP-CCSD/ano-pVQZ calculations, the ClSO band was assigned to the $1^2A'' \leftarrow X^2A''$ transition involving the $\pi^* \leftarrow \pi$ transition of the SO bond and the vibrational progression to the SO stretching mode of the 12A" state, with a maximum cross-section = $(2.0 \pm 0.5) \times 10^{-18}$ cm^2 near 286 nm (1σ uncertainty) and an average spacing of vibrational structure of 658 cm^{-1}. The rapid decay of the ClSO signal monitored near 303 nm could be fit to a second-order kinetic model over 10 - 90 Torr, which yields an effective bimolecular rate coefficient $k_{Cl+ClSO} = (1.48 \pm 0.42) \times 10^{-11}$ cm^3 molecule^{-1} s^{-1} at 292 K and 90 Torr (1σ uncertainty). This fast recombination reaction suggests that Cl-containing SO_x species might act as significant Cl atom reservoirs in sulfur-oxide-rich environments such as Venus' atmosphere. Moreover, the reported UV spectrum provides a new means for monitoring the ClSO radicals.

2.2—Introduction

Chlorine chemistry plays an important role in both the natural environment and our daily life.[1] Thionyl chloride (Cl_2SO) is not only a common chlorine source but also has direct chemical applications in battery science and organic synthesis. The lithium-thionyl chloride battery worked as a model battery in many applications[2,3] due to its high energy density despite the lack of rechargeability.[2] In organic chemistry, Cl_2SO is used as a standard reagent in converting –OH functional groups into –Cl; however, the exact mechanism is not yet known.[4] Reactive chlorine, in Earth's stratosphere, is most famous for the catalyzed destruction of ozone, which ultimately led to the ozone hole.[5] In Venus' mesosphere, Cl atoms have been proposed to catalyze the conversion of CO into CO_2 to remove oxygen[6] though Cl concentration could be strongly affected by the reactions with sulfur oxide to form Cl_2SO_2 as the ultimate reservoir.[7]

In the laboratory, Cl atoms are widely used to initiate oxidation reactions in atmospheric and combustion chemistry studies.[8] Molecular chlorine (Cl_2) and oxalyl chloride ($(ClCO)_2$) are common photolytic precursors due to their low reactivity photolysis co-products[9] and Cl atom quantum yields of ~2.[10] The small photolysis cross-sections of Cl_2 and $(ClCO)_2$ ($< 3 \times 10^{-19}$ cm^2 at 248 nm)[10,11] would typically lead to 1 - 2% of precursor depletion being photolyzed, which makes generating high Cl concentrations difficult without high precursor concentrations. However, high precursor concentrations can lead to experimental difficulties; for example, they can induce large background signals that hinder spectroscopic measurements.[12] In contrast, Cl_2SO has a large cross-section ($> 7 \times 10^{-18}$ cm^2) below 250 nm,[13] thus making it a high-yield photolytic source of Cl atoms for kinetic studies.[14–17]

The photolysis of Cl_2SO was studied by monitoring the spectroscopic and kinetic properties of sulfur monoxide (SO).[18] Previous studies in a collision-free environment[19,20] have suggested three photodissociation channels, including (1) a three-body dissociation channel, (2) a radical channel and (3) a molecular channel, as shown below:

$Cl_2SO \rightarrow 2Cl + SO$, $D_0 = 108.5 \pm 0.3$ kcal mol^{-1} (263.7 nm) (1)

$Cl_2SO \rightarrow Cl + ClSO$, $D_0 = 57.3 \pm 0.3$ kcal mol^{-1} (499.2 nm) (2)

$Cl_2SO \rightarrow Cl_2 + SO$, $D_0 = 51.3 \pm 0.3$ kcal mol^{-1} (557.6 nm) (3)

where the dissociation energies were calculated by Baum et al. using the JANAF Thermochemical Tables.[20] Although all three channels are energetically feasible after absorbing a photon below 250 nm, the dissociation dynamics depend strongly on the photolysis wavelength.[19–25]

At 193 nm, Cl_2SO is mainly excited through the $\sigma^*_{ClS} \leftarrow n_{Cl}$ transition[22] leading to a direct dissociation of two Cl atoms on a time scale faster than rotational motion[23] with the three-body channel (1, ~83%) dominating the radical (2, ~17%) and the molecular (3, <3%) channels.[20] At 235 nm, both $\sigma^*_{ClS} \leftarrow n_{Cl}$ and $\sigma^*_{ClS} \leftarrow n_S$ transitions are excited;[22] the three-body (1) and radical (2) channels yield both ground state $Cl(^2P_{3/2})$ and hot $Cl^*(^2P_{1/2})$ atom and a relative yield of $Cl^* = 0.35 \pm 0.06$ was reported.[22]

At 248 nm, calculations indicate that a mixture of $\sigma^*_{ClS} \leftarrow n_S$ and $\pi^*_{SO} \leftarrow n_S$ transitions are excited.[22] Previous theoretical work has predicted that the excited state, $\pi^*SO \leftarrow n_S$ transition, is not repulsive[23] and thus, that the radical dissociation pathway (2) dominates the main product channel (~96.8%) while the molecular channel (3) only contributes slightly (~3.2%).[20,21] No evidence of the three-body channel has been reported at 248 nm.[20,21] However, the laser-induced fluorescence spectrum of SO was observed; the SO yield of (13 ± 7)% under 1 Torr He,[21] was contributed to the unimolecular decomposition of the hot ClSO radicals.[21] Photofragment-translational spectroscopy showed that, after absorbing a photon, on average roughly half of the available energy (~104 cm^{-1}) stayed in the ClSO fragments[22] with a wide distribution, such that a small portion exceeded the dissociation threshold of Cl–SO ($D_0 = 17900 \pm 150$ cm^{-1}).[22,26] These calculations were validated by experimental data showing that the yield of SO was reduced at higher pressures.[18] The Cl* relative yield = 0.52 ± 0.03 at 248 nm was reported,[24] indicating that less than half of the ClSO radicals possess enough internal energy to dissociate.[22]

Although the product branching ratio and dynamics of Cl_2SO photolysis have been studied for decades, the main weak point of Cl_2SO as a Cl atom source is the unknown reactivity of ClSO radicals due to the lack of suitable methods for kinetic measurements. In the condensed phase, the ClSO solid-phase EPR spectrum has been investigated.[27] In the gas phase, the far-IR spectrum has been reported, but no analysis was done.[28] The microwave spectrum was mentioned in the literature without available data.[29] Chu et al.[30] has measured the IR spectrum of the nascent products from Cl_2SO photolysis at 248 nm and the ClSO radicals were identified by matching the simulation of the rotational resolved SO stretching band to experimental observations.[30] Only one kinetic measurement of the ClSO radical has been performed; using mass spectroscopy,[31] Blitz et al. reported a ClSO + NO_2 reaction rate coefficient of $(8.0 \pm 1.2)\times10^{-12}$ cm^3 $molecule^{-1}$ s^{-1} at 1 Torr He, but no products were found in the mass spectrum.[31]

Transient UV-Vis absorption spectroscopy is well suited for exploring the reactivity of ClSO under a wide range of conditions,[32] e.g., solving the debate of Cl_2SO photolysis behavior in tetrahydrofuran.[33,34] However, the UV-Vis spectrum of the ClSO radical is still unknown. Li performed the QCISD calculation on the lowest excited state of the ClSO radicals and predicted an adiabatic transition energy close to 2.4 eV.[35] This work aimed to obtain the gas phase UV-Vis spectrum of ClSO radicals generated from Cl_2SO photolysis at 248 nm and to explore the kinetics of its subsequent reactions by performing pulsed-laser photolysis (PLP) experiments with a time-resolved broad-band UV-Vis transient–absorption spectroscopy coupled with a flow reactor.

2.3—Experimental Setup

2.3.1—Chemical Preparation

Schematics of the experimental system are shown in Figures S1 and S2. The ClSO radicals were generated in a glass reactor (L = 50.8 cm, ID = 3.8 cm) with UV anti-reflection fused silica windows (Edmund, 36948), where the inner sides were purged by a small stream of the buffer gas to prevent contamination. The Cl_2SO/buffer mixture flowed into the reactor from the middle and was pumped out at the two ends, resulting in an effective gas length of 43.2 cm (Figure S2). Mass-flow controllers (MKS, GM50A and 1179A) metered the total flow, ensuring fully gas sample replacement between photolysis laser shots (repetition rate = 4 Hz for all experiments except where stated otherwise). A small stream of buffer gas carried Cl_2SO vapor (Sigma-Aldrich, >99%) out of a bubbler, immersed in a temperature-controlled water bath (Fisherbrand, Isotemp 4100). A glass/Teflon needle valve (Gilmont instruments, GM-7100), controlled the bubbler pressure. A similar bubbler setup introduced iodine into the reactor; however no needle valve was used due to the low vapor pressure of iodine (0.2 Torr at 20 °C).

A gas mixture of 0.66% NO_2 was prepared by premixing NO and O_2 (Matheson, 99.5%, and Airgas, 99.994%, respectively) in a 1:12 ratio, balance N_2 (5300 Torr total pressure) in a stainless cylinder and left overnight for fully mixing. The excess O_2 was added to ensure conversion of NO to NO_2.[36] All pressures in the reactor and bubblers were measured with diaphragm gauges (Baratron 127AA-01000A, 122AA-01000CB and MKS 127AA-00100A) A throttle valve (MKS, type 153) controlled the pressure of the reactor. The Cl_2SO concentrations were directly measured in the reactor with the UV spectrometer. Typical concentrations in the reactor were: $[Cl_2SO] = (0.5–2.4) \times 10^{14}$ molecule cm^{-3}, $[I_2] = (0–7.3) \times 10^{14}$ molecule cm^{-3}, $[NO_2] = (0–1.7) \times 10^{14}$ molecule cm^{-3} and N_2 (LN_2 evaporation), He (Airgas, 99.999%) or Ar (Matheson, 99.9995%) balanced (10–90 Torr). All the experiments were conducted at 292 K.

2.3.2—Optical Setup

The UV light from a laser driven light source (LDLS, Energetiq, EQ-99) was aligned through a multi-pass UV enhanced White cell (D = 25.4 cm, R = 140 cm, Acton Optics). After the White cell, the probed beam was focused into a spectrometer (Acton, SpectraPro 300i) with a gated image-intensified CCD array (Princeton Instruments, PI-MAX4, 1024 × 256) and a photomultiplier tube (PMT, Hamamatsu, R928). After the grating, a rectangular mirror reflected the bottom portion of the probe beam into the PMT, monitoring the absorbance change near the center wavelength (resolution ~1 nm), enabling simultaneous PMT and ICCD light collection. The spectrometer wavelength and resolution (~0.4 nm) were characterized using a mercury pen-ray lamp (Hg-Ar).

The excimer (Coherent, COMPex 205F, KrF) photolysis laser beam was aligned between the two White cell objective mirrors, spaced 15 mm apart, and directed towards the field mirror. A long-pass filter (Semrock, LP02-257RU-30×40) in front of the field mirror discriminated the 248 nm photolysis light from the probed beam path. The photolysis beam was focused horizontally at the gap between the two White cell objective mirrors so that the photolysis beam filled the entire volume of the reactor, maximizing the overlap with the probe-beam path. As the photolysis beam was diverging slightly ($\theta_{\mathrm{div}} \sim 6^{\circ}$) across the reactor, the divergence effect was tested by focusing the photolysis beam at distinct positions and monitoring the kinetics of the simplest Criegee intermediate.

2.3.3—Data Acquisition

The experiments were controlled by LabView 2018 and all pressure and flow values were recorded through a DAQ card (NI, cDAQ-9174). The excimer laser and DAQ cycle were synchronized by two delay generators (Stanford research DG535 and BNC Model 565), with the DG535 used as the primary controller, while ICCD was stepped controlled (gate width = 47, 70.5, 94, or 164.5 μs) via the program. The PMT output passed through a homemade transimpedance amplifier and was collected with a DAQ card (Gage, CS144002U, Sampling Rate = 200 kS s^{-1}). Typically, spectra were averaged over 256, 384 or 512 laser shots for a given delay time, while the PMT profile was averaged over all laser shots throughout the whole experiment. A small absorption background (< 0.3% at 303 nm depending on laser fluence) was observed after time zero (Excimer laser on). This background was observed with the reactor removed from the beam path and could be discriminated by misaligning the photolysis and probe beams, however this would have caused the photolysis beam to not pass through the reactor cleanly. As such, the background was suspected to be caused by the photolysis and probe-beam overlap at the long-pass filter. The photolysis laser power (Coherent, J-50MUV-248) was measured either at the reactor's exit or after the long-pass filter. All the presented data here were background subtracted.

2.4—Theoretical Methods

ClSO is an open-shell molecule with 22 core electrons and 19 valence electrons, which permits the use of coupled-cluster methods for highly accurate determinations of structural and energetic parameters. All quantum chemical calculations were performed using the CFOUR program suite,[37] with the exception of unrestricted LR-CCSDT[38] calculations (equivalent to EOMEE-CCSDT for energies),[39] which were performed using the MRCC package.[40] Atomic natural orbital (ANO) type basis sets have been shown to perform well for the prediction of harmonic frequencies,[41] prompting the use of the ano-pVXZ series of basis sets by Neese et al.,[42] which are one of the few non-relativistic ANO-type basis sets which cover the third period. As these basis sets are not optimized for the calculation of core correlation, computational cost was greatly reduced by invocation of the frozen-core approximation. Geometries and energies were calculated using two distinct references, as detailed below.

2.4.1—Unrestricted Reference

The ground state was optimized using CCSD/ano-pVQZ on an unrestricted Hartree-Fock (UHF) reference, while the $1^2A''$ excited state was optimized using EOMEE-CCSD/ano-pVQZ, also on a UHF reference. Vibrational frequencies were calculated at each geometry by finite difference of analytic gradients.[43–46] Excitation energies and oscillator strengths for the $1^2A''$, $1^2A'$, and $2^2A'$ states were calculated at both geometries. Energies of the X and $1^2A''$ states were refined by a term loosely analogous to the ΔEHLC term of the HEAT method,[47–49] using the difference between LR-CCSDT[38] and EOMEE-CCSD energies in a smaller basis (ano-pVDZ) to correct for the effect of connected triple excitations.

2.4.2—Restricted Reference

Both the ground state and $1^2A''$ excited state were optimized with the EOMIP-CCSD/ano-pVQZ method using the $ClSO^-$ anion as a closed-shell reference. Use of this reference allowed both states to be treated on equal footing at the same level of excitation. Frequencies for both states were calculated at the same level of theory by finite difference of analytic gradients.[50] Energies of the minima were refined by EOMIP-CCSDT/ano-pVQZ calculations, where the use of the large basis was made affordable by the use of the restricted Hartree-Fock (RHF) reference.

2.4.3—Spectral Simulation

A displaced harmonic oscillator stick spectrum, including overtone and combination bands as well as corrections for temperature, was simulated using the ezSpectrum package. Parameters for the simulation were taken from the restricted reference calculations.

2.5 – Results and Discussion

Figure 1A shows the difference absorption spectra of the Cl_2SO/N_2 photolysis system. Negative absorption below 280 nm was observed and attributed to the Cl_2SO depletion. A structured absorption features was observed below 320 nm; the temporal profiles (Figure 2) near 303 nm showed an instantaneous (<5 μs) formation following Cl_2SO photolysis, indicating the structured absorption was due to the primary photolysis products. As shown in Figure 1, the 303 nm wavelength was chosen for kinetic traces of the structured absorption to avoid interference from the Cl_2SO depletion.

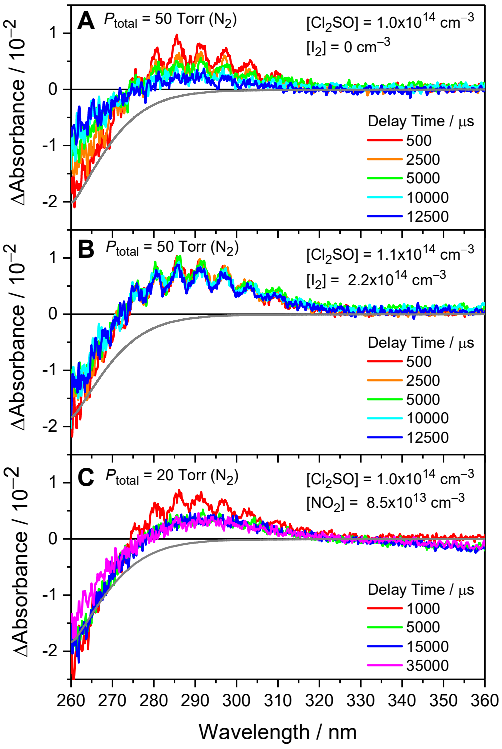

Figure 2.1. Representative transient-absorption spectra of the Cl_2SO/N_2 photolysis system at different delay times (gate width = 70.5 μs) recorded (A) without scavengers, (B) with I_2 and (C) with NO_2 for Exp# I-1, I-2, and N-5 (Tables S1 and S2), respectively. The photolysis laser sets time zero. The negative gray lines show the estimated initial Cl_2SO depletion.

Interestingly, the Cl_2SO depletion was observed to disappear after time zero (Figure 1A), on a timescale which was faster than the gas residence time (Figure S7−S8). We observed an isosbestic point near 275 nm (Figure S21), suggesting that Cl_2SO reformed through a chemical reaction from the origin of the structured spectrum (Figure S26−S27). Literature has shown that the primarily photolysis product channel of Cl_2SO at 248 nm is the radical channel (2), with the Cl atom and ClSO radical quantum yields close to unity.[20,21]

We proposed that the origin of the structured absorption spectrum is the ClSO radical and that recombination between the Cl atom and ClSO radical regenerates Cl_2SO, giving rise to the observed decay of ClSO and regeneration of Cl_2SO.

To test this hypothesis, first, we added iodine (I_2) as a Cl atom scavenger ($k_{\mathrm{I2+Cl}} = 2.5 \times 10^{-10}$ cm^3 molecule^{-1} s^{-1}).[51] Figure 1B shows that the lifetime of Cl_2SO depletion and the structured absorption was extended in the presence of I_2, i.e., in the absence of the Cl atoms. Second, we added NO_2 as a ClSO scavenger.[31] In the presence of NO_2 (Figure 1C), the structured absorption disappeared within 5 ms, while the Cl_2SO depletion survived. The negative absorption near 360 nm was attributed to NO_2 depletion through reaction with the origin of the structured spectrum. The same effect was observed by varying [I_2] (Figure S7−S9 and S18), [NO_2] (Figure S10−12 and S19), [Cl_2SO] and the total pressure (Table S1−S2). Although a broad product absorption feature was observed below 320 nm, both tests implied that the Cl_2SO reformation requires the presence of the origin of the structured spectrum.

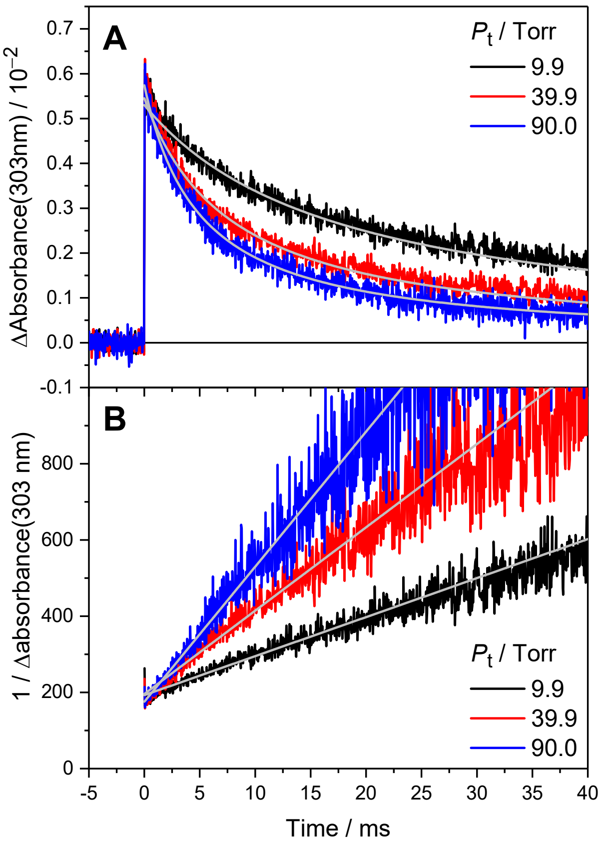

Figure 2.2. (A) Representative absorption temporal profiles near 303 nm of the Cl_2SO/N_2 photolysis system at different pressures for Exp# 1, 4 and 9 (Table S3). (B) The reciprocal of (A). The gray lines show a linear fit to 0.5–20 ms region only to lessen the impact from potential secondary reactions on the determination of the rate coefficient but good linearity was observed out to 40 ms. The gray lines in (A) are the reciprocal of linear fit in (B).

Additionally, Figure 2A shows that the decay rate of the structured absorption increased at higher pressures (Figure S13−17 and Table S3), implicating a possible recombination reaction or complex formation. Figure 2B shows the reciprocal of the temporal profiles; a linear regression was used to describe the data between 0.5–20 ms, suggesting the decay follows a second-order reaction. Figure S28 shows that similar slopes are observed for different initial intensity. This observation could be rationalized by noting that [Cl]:[ClSO] = ~1. The reaction rates of Cl atoms with NO_2, NO and O_2 depend on the total pressure[52] and are slow under our experimental conditions. This simple model describes most of the temporal profile but small amount of hot ClSO decomposition at short time and slight residual of ClSO at long time due to distinct loss rate of Cl and ClSO could cause deviations from the simple model.

The $Cl + Cl_2SO \rightarrow Cl_2 + ClSO$ reaction potentially breaks our hypothesis. However, we ruled out this possibility since the reaction rate coefficient of $Cl + Cl_2SO$ reaction is $k_{Cl+Cl2SO} = (6 \pm 4) \times 10^{-14}$ cm^3 molecule^{-1} s^{-1},[24] which is significantly slower than the decay rate of the structured absorption. We can neglect reactions of hot Cl*, which mainly undergoes rapid deactivation to form a ground-state Cl atom by colliding with Cl_2SO.[24]

Finally, we consider the possibility that the structured absorption was due to the formation of another photolysis/reaction product or impurity. Though they are not expected to form directly in this system, no evidence of SO_2, S_2O and OClO was observed based on their distinct vibronic structures. SO can be produced directly from the photolysis of Cl_2SO, but the lowest transition energy of SO = 37940 cm^{-1} (263.6 nm),[53] below our detection window. Molecular chlorine has an absorption maximum near 330 nm, close to structured spectrum; based on the small yield of the molecule channel, (3) from the Cl_2SO photolysis,[20,21] the small absolute cross-section of Cl_2, $\sigma_{Cl2}(330\text{ nm}) = 2.5 \times 10^{-19}$ cm^2,[11] and the slow Cl self-recombination at < 100 Torr ($< 1.7 \times 10^{-13}$ cm^3 molecule^{-1} s^{-1}),[54] we estimated an upper limit absorbance of Cl_2 < 0.05% near 330 nm. Considering that the ClSO radicals have been identified in the MIR-spectrum from Cl_2SO photolysis at 248 nm[30] and the Cl_2SO reformation was observed, we assigned the structured absorption to ClSO radicals.

2.5.1—Extraction of the ClSO Spectrum

The extraction of the ClSO spectrum relied on estimating the initial Cl_2SO depletion. We directly measured the Cl_2SO concentration in the reactor by monitoring its UV absorption; then, the Cl_2SO depletion was calculated from the absolute cross-section[13] and the photolysis laser fluence. Estimating radical concentration based on photolysis laser fluence alone has been challenging.[55] Therefore, this procedure was calibrated by conducting measurements on the photolytic depletion of CH_2I_2 and the formation of the simplest Criegee intermediate in the presence of O_2 under the same experimental setup (Figure S3). The laser power measured after the reactor systematically underestimated the Cl_2SO depletion. (See SI for details of estimating the $\Delta[Cl_2SO]$, initial [ClSO] and the error analysis).

As shown in Figure 1, the negative gray lines represent the estimated initial Cl_2SO depletion. The ClSO spectra, collected under distinct conditions, were obtained by subtracting the recorded data from the Cl_2SO depletion. While hot ClSO radicals were expected from the photolysis of Cl_2SO, the IR measurements at 22 Torr Argon showed that the rotational distribution of the SO vibrational band fit well to the simulation at a rotational temperature of 350 K in the spectrum recorded within 10–40 μs.[30] Therefore, we believed that the ClSO radicals were thermalized after 0.1 ms in our experiments, which was validated by the experimental ClSO spectra recorded within 0.1−1 ms, showing no significant difference under 10–90 Torr.

Figure 3 shows the ClSO spectrum collected across all pressure (gray lines); only the spectra, recorded within the first millisecond, were processed to minimize the influence of the Cl_2SO reformation (Figure S20–S25). The absolute cross-section was estimated by using the radical channel yield of 96% at 248 nm.[20,21] Because a small portion ($< 13\%$)[21] of the ClSO radicals may dissociate under our experimental conditions, this estimation may be treated as a lower bound of the ClSO absolute cross-section. Recall that the isosbestic point was observed near 275 nm; the Cl_2SO depletion dominated in the absorption change below 275 nm. The gray area in Figure 3 roughly shows the relative uncertainty.

The average ClSO spectrum (Figure 3, solid black line) was fitted using multiple Gaussian peaks and was analyzed using first derivative to obtain the peak positions of the observed structure (Figure S6). As shown in the Figure 3 inset, the structured absorption has an average spacing of 658 cm^{-1}. To get more insights into the observed band, we performed high-level ab initio calculations to estimate the transition energies and the corresponding harmonic vibrational frequencies of ClSO radical.

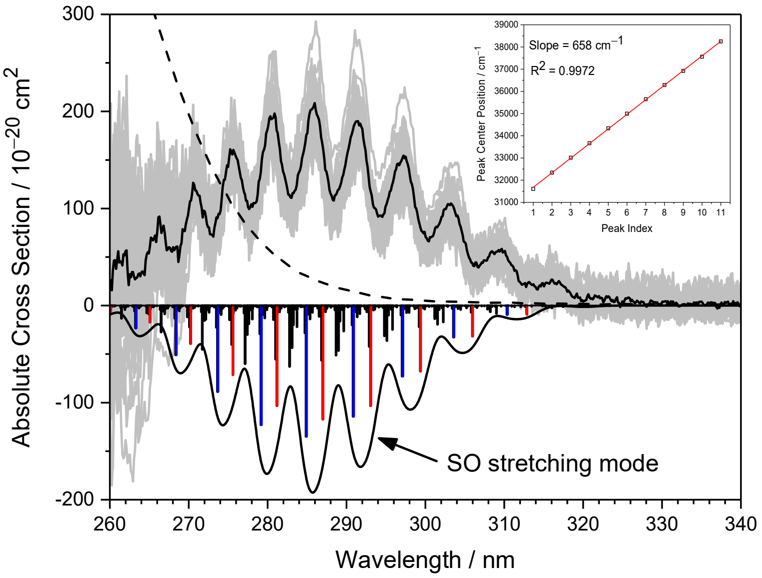

Figure 2.3. The black line is the average of all the ClSO spectra shown in gray (Table S3). The dotted line shows the cross-section of Cl_2SO for comparison. The stick diagram downward shows the calculated vibrational progression for the $1^2A''$ excited state. The red and blue bars are the SO stretching series with 0 and 1 quanta excitation of the bending mode and black line profile present the simulated spectrum (FWHM = 3 nm) of these two series (Table S6). Inset: liner fit to the observed peak centers.

2.5.2—Comparison with Theoretical Calculations

Table 1 summarizes all the calculation results. The electronic configuration of the X state has A" symmetry with the unpaired electron occupying the π* orbital, as suggested by the EPR spectrum.[27] Three low-lying excited states were identified, two with A' symmetry and one with A" symmetry in the C_s point group, which roughly corresponds to the alpha HOMO to LUMO (1^2A'), beta HOMO-2 to HOMO (2^2A') and beta HOMO-1 to HOMO transition (1^2A"), respectively. Figure 4 shows the natural density difference orbitals for these transitions. We noted that the predicted transition oscillator strengths to the two A' excited states are very small, where in contrast, the A" excited state has a stronger oscillator strength. Furthermore, the vertical transition energies to the two A excited states are close to 3.3 eV; Li et al.[35] have predicted an adiabatic transition energy to the 2^2A' excited state ~2.3 eV, which is significantly smaller than the observed band position. Considering the predicted vertical transition energy is lower than the experimental observation and the small predicted oscillator strengths, we did not further consider the two A' states in this work.

The diabatic transition energy of the 1^2A" state is 4.17 eV at EOMEE-CCSD/ano-pVQZ level. Further correction connected triples in a smaller basis set lowers the adiabatic transition energy to 3.90 eV (317.8 nm). The zero point energy correction (ZPE) yields a 0–0 transition energy of 320.1 nm. We compare this result to the adiabatic transition energy calculated at the EOMIP-CCSDT/ano-pVQZ//EOMIP-CCSD/ano-pVQZ level, which agrees within 100 cm^{-1}, with a final 0-0 transition energy agreeing within 10 cm^{-1} due to fortuitous cancellation between differences in predicted adiabatic transition energies and ZPE corrections. Nevertheless, the close agreement in adiabatic transition energies reinforces confidence in the accuracy of both calculations.

The excitation to the 1^2A" state is attributed to the $\pi^* \leftarrow \pi$ transition along the SO bond (Figure 4). EOMIP-CCSD predicts that the equilibrium SO bond length increases from 1.463 Å to 1.676 Å in the 1^2A" excited state while the bond angle becomes slightly smaller, with no significant change in the ClS bond length. Moreover, we found the vibrational frequency changes from 321 cm^{-1}, 542 cm^{-1}, and 1190 cm^{-1} to 259 cm^{-1}, 480 cm^{-1} and 720 cm^{-1} for the bending, ClS stretching and SO stretching modes, respectively. Notably, the SO stretching mode at the $1^2A''$ excited state is slightly larger than the observed average spacing.

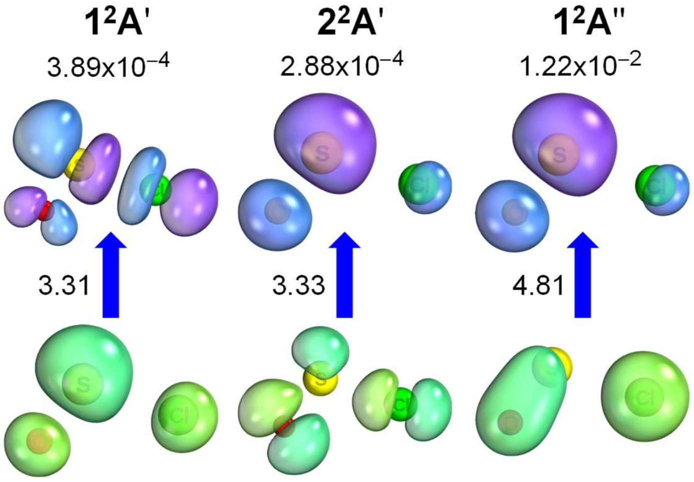

Figure 2.4. The calculated oscillator strength, vertical excitation energies (in eV) and the natural density difference orbitals (top view) for the $1^2A'$, $2^2A'$ and $1^2A''$ excited states calculated at EOMEE-CCSD/ano-pVQZ level and the ground-state geometry.

The Franck-Condon factors are calculated by assuming a displaced harmonic oscillator model and 300 K Boltzmann weighting for hot bands to compare the observed vibrational structures (Figure 3). For the SO stretching (red bar), the strongest peak occurs at the $\nu_{SO} = 5 \leftarrow 0$ transition (Table S6), and a similar result was observed for the SO series with one quantum bending excitation (blue bars). The adiabatic 0-0 transition is computed to be 320.1 nm but is predicted to have no Franck-Condon overlap. From the predicted spectrum, we extrapolate the experimental progression suggests an origin between 316 and 324 nm.

By assuming Gaussian for each transition, the simulation spectrum (Figure S29) indicates that the broad feature originates from the combination bands and hot bands. Note that the simulation does not include the rotational structures, which could make the overlap region more diffuse and make the strong SO stretching series (red bar and blue bar) overlap.

We assign the observed band to the $1^2A'' \leftarrow X\ ^2A''$ transition, and the vibronic structure to the SO stretching mode. This assignment is similar to the C ← X transition in S_2O where a similar vibronic structure has been observed and mainly attributed to the SS stretching mode.[56] For ClSO, due to the low resolution of the experimental spectra, the contributions from rotational structure and combination/hot bands are unresolved and we could not determine the anharmonic parameter. We expect anharmonicity in the $1^2A''$ state to be insignificant, given that both SO and SS stretching modes in the analogous C state of S_2O exhibit small anharmonicities.[56]

Table 2.1. The (EOM-)CCSD and CCSDT calculation of ClSO for geometries, energies relative to the optimized ground state ΔE, harmonic vibrational frequencies, and the 1^{2}A"← X ^{2}A" transition energies.

SCF Reference		UHF/EOMEE		RHF/EOMIP (Anion)	
Geometry Optimized		X ^{2}A" state	1^{2}A" state	X ^{2}A" state	1^{2}A" state
Geometry[a]	r(Cl–S) / Å	2.046	2.011	2.034	2.009
	r(S–O) / Å	1.461	1.662	1.463	1.676
	∠(ClSO) / degree	109.25	102.91	109.42	100.89
ΔE / cm^{-1}	1^{2}A"	38795	33596 (31465)[b]	36833[c]	31536[c]
	2^{2}A'	26892	-		
	1^{2}A'	26701	-		
	X^{2}A"	0	6037	0	-
Frequencies / cm^{-1}	ClSO bending	316	254	321	259
	ClS stretching	516	503	542	480
	SO stretching	1200	831	1190	720
Adiabatic transition energy / cm^{-1}		31465 (317.8 nm)[d]		31536 (317.1 nm)[d]	
0-0 transition energy / cm^{-1}		31244 (320.1 nm)[d]		31239 (320.1 nm)[d]	

[a] Optimization at the CCSD/ano-pVQZ level.

[b] After correction ΔE$_{HLC}$ = CCSDT/ano-pVDZ – CCSD/ano-pVDZ

[c] At EOMIP-CCSDT/ano-pVQZ level

[d] The corresponding wavelength is shown in the parentheses.

2.5.3—The Pressure Dependence of the Cl + ClSO Reaction

By assuming, the initial concentrations of the Cl atoms and ClSO radicals were similar and their loss rates through other pathways were slow compared to the recombination reaction; as a result, the rate equation of a simple second-order reaction was obtained. The integration form yields the time behavior of the absorbance change in this second-order model [1].

$$\Delta Abs=\frac{A_0}{1+A_0\frac{k_{\mathrm{Cl+ClSO}}}{\sigma L}t} \qquad [1]$$

where $\triangle Abs$ denotes the absorption change, A_0 denotes the peak absorption, σ denotes the ClSO absorption cross-section, and L denotes the effective path length. By substituting the concentration to absorbance, the recombination rate coefficient was obtained once L and σ are known.

The second-order model [1] well described the observed temporal profiles measured at 303 nm to long times even though the fitting was performed within 0.5–20 ms (Figure S13−S17). The good linear behavior of the reciprocal absorption indicated that the perturbations from other reactions were small in our time window. Figure 5 shows the recombination rate coefficients, $k_{\mathrm{Cl+ClSO}}$, measured at different pressures using three buffer gases (He, N_2 and Ar). The recombination rate coefficients seem to reach the high-pressure limit near 90 Torr. In addition, no clear difference was observed for He, Ar and N_2 though it may be due to the data scattering.

Scheme 2.1. Proposed mechanism of Cl + ClSO → Cl_2SO reaction

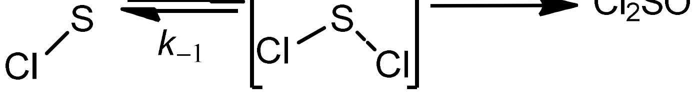

We proposed (Scheme 1) that Cl and ClSO may form a hot [Cl---ClSO]* complex, k_1, which could dissociate back to the reactants, k_{-1}, or collide with a third body, and be stabilized into a well to eventually form Cl_2SO, k_s[M]. Applying the steady-state approximation to the hot Cl_2SO^* leads to equation [2] for the recombination rate coefficients.

$$k_{\mathrm{Cl+ClSO}} = \frac{k_1[M]}{\frac{k_{-1}}{k_s} + [M]} \qquad [2]$$

This model reasonably described our data in Figure 5 (red line) The extrapolation of equation [2] yields rate coefficients for the high-pressure limit $k_\infty = (2.58 \pm 0.72) \times 10^{-11}$ cm^3 $molecule^{-1}$ s^{-1} and for the low-pressure limit $k_0 = (1.21 \pm 0.44) \times 10^{-29}$ cm^6 $molecule^{-2}$ s^{-1} (1σ uncertainty). These parameters are valid over 10 - 90 Torr only. Measurements over a wider pressure range are needed to give better estimations.

Due to the relative high uncertainty (1σ = 23.9%) at 10 Torr, we may consider that other bi-molecular reactions dominates under low pressure, similar to the case of the hydroperoxyl radical self-reaction, to cause a non-zero intercept at low-pressure limit.[57] Possible candidates includes $Cl + ClSO \rightarrow Cl_2 + SO$ ($\Delta H_0(0) = -6.0$ kcal mol^{-1}), $2ClSO \rightarrow Cl_2 + 2SO$ ($\Delta H_0(0) = -45.2$ kcal mol^{-1}) and $2ClSO \rightarrow Cl_2SO + SO$ ($\Delta H_0(0) = -6.1$ kcal mol^{-1}). Because $k_{\mathrm{Cl+ClSO}}$ increased by a factor of three from 10 Torr to 90 Torr, the isosbestic point in the spectrum should change significantly without Cl_2SO formation; however, the spectra showed no clear changes in the isosbestic point (Figure S20). In addition, we found that the ClSO decay rate was roughly four times slower in the presence of I_2 (Table S1 and Figure S7–S8), indicating the ClSO self-reaction and loss rates are negligible. Possible contributions from the mixing of gases, as they enter in and pump out from the reactor, were also excluded by performing measurements at refresh rates = 4 Hz, 2 Hz and 1 Hz. Considering the reaction energy change, calculated from bond dissociation energies, the Cl + ClSO reaction has the strongest exothermicity forming Cl_2SO, supporting that it is the main decay pathway.

Although we excluded some potential effects that influence measurements from directly monitoring the decay of ClSO radicals at low pressure, it is hard to figure out all possibilities. For example, large deviation has been reported in the studies of the CH_3 recombination reaction and the secondary reactions in different photolysis system were suspected.[58]

Note that the rate coefficient $k_{Cl+ClSO}$ at 90 Torr is ~400 times faster than recombination of the Cl atoms, but a small amount of Cl_2SO depletion residual was observed when the ClSO radicals disappeared (Figure S24-S25), implying other reactions involving the Cl atom and ClSO radical occurred. The hot Cl* atom was quickly (lifetime = ~100 μs under 90 Torr N_2)[59] quenched by buffer gas to form the ground-state Cl atom and the lifetime of Cl atom could be long without the co-reactants.[24] Thus, other reactions between the ClSO radicals and unknown impurities might have contributions.

The solid angle analysis yielded an estimation of the higher-pressure limit $k_\infty = 7 \times 10^{-11}$ cm^3 $molecule^{-1}$ s^{-1} by considering the ClSO ground-state geometry ($360^\circ - 109.25^\circ = 250.75$ $^\circ$) and a gas collision rate of 10^{-10} cm^3 $molecule^{-1}$ s^{-1}. The recombination rate coefficient at low pressure was expected to be faster than similar reactions, such as the Cl + NO_2 reactions, because Cl_2SO has more low-frequency modes and smaller rotational constants than either ClONO or $ClNO_2$,[60] indicating a higher energy transfer efficiency and suggesting $k_{Cl+ClSO}$ is significantly larger than 3×10^{-13} cm^3 $molecule^{-1}$ s^{-1} at 10 Torr.52 Indeed, our measurements fall between these two limits.

Potential Implications. As shown previously, a broad product absorption feature was observed in the presence of NO_2 (Figure 1C) and decayed slowly, indicating the origin of this broad feature is different from ClSO. While we were not certain about the identity of the origin of spectrum, we found that it is not similar to possible side products (e.g., Cl_2,

NO_2, N_2O_5) and so we speculate this could be due to the adduct of ClSO and NO_2 (Figure S10–S12). Besides, the far-infrared and rotational spectra were assigned to the ClSO radicals based on several chemical tests, including formation from the Cl + SO reaction.[28,29] It seems that SO and ClSO have the potential to be the Cl atom reservoirs by forming Cl_2SO, which was not mentioned in Venus' atmospheric models.[61,62] Furthermore, the ClSO radicals may be a general radical reservoir through recombination reactions under high pressure, which is worth further studying. This work also suggested that the Cl atom yield from Cl_2SO photolysis in the solution phase or solid phase could be even smaller than in the gas phase due to the cage effect and the high energy transfer efficiency to the environment due to the rapid Cl + ClSO → Cl_2SO reaction.

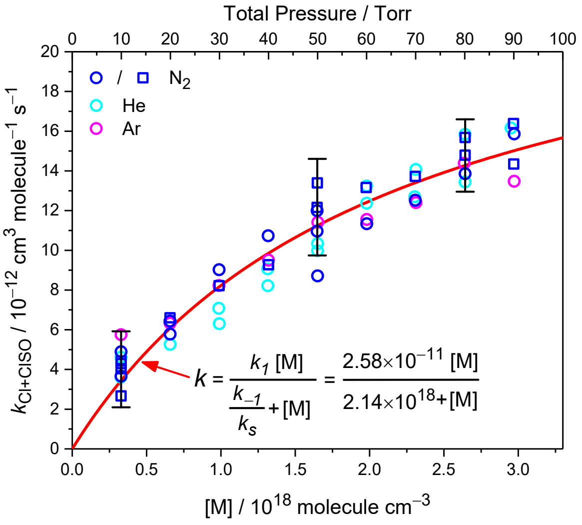

Figure 2.5. The observed rate coefficient as a function of the total pressure (assuming σClSO(303 nm) = 1.0×10^{-18} cm^2 and L = 431.8 cm). The red line shows the fit to all the experimental data on the figure using proposed mechanism in Scheme 1. Black error bars present 2σ of the blue circles distribution. The circle (Exp #1–9 and 23–48) and square (Exp #10–22, Rep. Rate = 1 or 2 Hz, Table S3) symbol presents measurements with distinct gas refresh rates.

2.6—Conclusions

In this work, the UV spectrum of the ClSO radical was identified from the Cl_2SO photolysis at 248 nm using a time-resolved broadband UV-Vis transient-absorption spectroscopy coupled with a PLP flow reactor. The ClSO absorption band showed clear vibronic structures with an average vibrational spacing of 658 cm^{-1}. The band maximum was observed near 286 nm with a cross-section of $(2.0 \pm 0.5) \times 10^{-18}$ cm^2 (1σ uncertainty). In addition, high-level ab initio calculations were performed for the excited states of ClSO at EOMEE-CCSD/ano-pVQZ level. Three low-lying excited states with two A' and one A" symmetry were identified. The predicted vertical transition energies of the two A' (3.3 eV) are significantly smaller than the ClSO band position and the predicted oscillator strengths are small; in contrast, the A" has a large oscillator strength. The $1^2A" \leftarrow X\ ^2A"$ transition was described by the $\pi^* \leftarrow \pi$ transition of the SO bond, resulting in longer SO bond length and a SO stretching frequency of 720 cm^{-1}. The 0-0 transition energy at EOMIP-CCSDT/ano-pVQZ//EOMIP-CCSD/ano-pVQZ level agrees well with the experiments. The Franck-Condon factors were calculated, which is similar to the overall profile of the experimental observation.

Additionally, the $Cl + ClSO \rightarrow Cl_2SO$ reaction was investigated by using the observed spectrum between 10–90 Torr (N_2, He and Ar). This recombination reaction showed a strong pressure dependence, $k_{Cl+ClSO} = (2.58 \pm 0.72) \times 10^{-11}$ cm^3 $molecule^{-1}$ s^{-1})[M] / (2.14×10^{18} molecule cm^{-3} + [M]) at 292 K (1σ uncertainty), which was not strongly affected by the buffer gases. This observation, combined with other literature data implies that ClSO might be a Cl atom reservoir in Venus' atmosphere. It also provided necessary data for designing a chemical system by using Cl_2SO photolysis as a Cl atom precursor. Most importantly, the observed UV spectrum offers a new approach to studying the reactivity of the ClSO radicals under a wide range of experimental conditions, including at high pressure or in the solution phase.

2.7—References

1. Finlayson-Pitts, B. J. Chlorine chronicles. *Nature Chem* **5**, 724–724 (2013).
2. Zhu, G., et al. Rechargeable Na/Cl2 and Li/Cl2 batteries. *Nature* **596**, 525–530 (2021).
3. Gangadharan, R., Namboodiri, P. N. N., Prasad, K. V. & Viswanathan, R. THE LITHIUM-THIONYL CHLORIDE BATTERY—A REVIEW. *Journal of Power Source* 1–9 (1979).
4. El-Sakka, I. A. & Hassan, N. A. Synthetic uses of thionyl chloride. *Journal of Sulfur Chemistry* **26**, 33–97 (2005).
5. Space Studies Board, Division on Engineering and Physical Sciences, & National Academies of Sciences, Engineering, and Medicine. *Thriving on Our Changing Planet: A Decadal Strategy for Earth Observation from Space: An Overview for Decision Makers and the Public*. 25437 (National Academies Press, Washington, D.C., 2019). doi:10.17226/25437.
6. Pernice, H., et al. Laboratory evidence for a key intermediate in the Venus atmosphere: Peroxychloroformyl radical. *Proc. Natl. Acad. Sci. U.S.A.* **101**, 14007–14010 (2004).
7. Mills, F. P. & Allen, M. A review of selected issues concerning the chemistry in Venus' middle atmosphere. *Planetary and Space Science* **55**, 1729–1740 (2007).
8. Osborn, D. L. Reaction Mechanisms on Multiwell Potential Energy Surfaces in Combustion (and Atmospheric) Chemistry. *Annu. Rev. Phys. Chem.* **68**, 233–260 (2017).
9. Baklanov, A. V. & Krasnoperov, L. N. Oxalyl ChlorideA Clean Source of Chlorine Atoms for Kinetic Studies. *J. Phys. Chem. A* **105**, 97–103 (2001).

10. Ghosh, B., Papanastasiou, D. K. & Burkholder, J. B. Oxalyl chloride, ClC(O)C(O)Cl: UV/vis spectrum and Cl atom photolysis quantum yields at 193, 248, and 351 nm. *The Journal of Chemical Physics* **137**, 164315 (2012).
11. Gibson, G. E. & Bayliss, N. S. Variation with Temperature of the Continuous Absorption Spectrum of Diatomic Molecules: Part I. Experimental, The Absorption Spectrum of Chlorine. *Phys. Rev.* **44**, 188–192 (1933).
12. Pope, F. D., Hansen, J. C., Bayes, K. D., Friedl, R. R. & Sander, S. P. Ultraviolet Absorption Spectrum of Chlorine Peroxide, ClOOCl. *J. Phys. Chem. A* **111**, 4322–4332 (2007).
13. Uthman, A. P., et al. Photoabsorption spectra of gaseous methyl bromide, ethylene dibromide, nitrosyl bromide, thionyl chloride, and sulfuryl chloride. *J. Phys. Chem.* **82**, 2252–2257 (1978).
14. Langer, S., McGovney, B. T., Finlayson-Pitts, B. J. & Moore, R. M. The dimethyl sulfide reaction with atomic chlorine and its implications for the budget of methyl chloride. *Geophys. Res. Lett.* **23**, 1661–1664 (1996).
15. Cabanas, B., et al. Study of reaction processes of furan and some furan derivatives initiated by Cl atoms. *Atmospheric Environment* **39**, 1935–1944 (2005).
16. Villanueva, F., et al. Primary product distribution from the Cl-atom initiated atmospheric degradation of furan: Environmental implications. *Atmospheric Environment* **41**, 8796–8810 (2007).
17. Szori, M., Csizmadia, I. G., Fittschen, C. & Viskolcz, B. Theoretical Study on Reactions of HO_2 Radical with Photodissociation Products of Cl_2SO (ClSO and SO). *J. Phys. Chem. A* **113**, 9981–9987 (2009).

18. Donovan, R. J., Husain, D. & Jackson, P. T. Spectroscopic and kinetic studies of the SO radical and the photolysis of thionyl chloride. *Trans. Faraday Soc.* **65**, 2930 (1969).

19. Kawasaki, M, et al. Photodissociation of Cl2SO at 248 and 193 nm in a molecular beam. *Chemical Physics* 285–291 (1984).

20. Baum, G., Effenhauser, C. S., Felder, P. & Huber, J. R. Photofragmentation of thionyl chloride: competition between radical, molecular, and three-body dissociations. *J. Phys. Chem.* **96**, 756–764 (1992).

21. Wang, H., Chen, X. & Weiner, B. R. Laser photodissociation dynamics of thionyl chloride: concerted and stepwise cleavage of S-Cl bonds. *J. Phys. Chem.* **97**, 12260–12268 (1993).

22. Roth, M., Maul, C. & Gericke, K.-H. Competitive channels in the photodissociation of thionyl chloride. *Phys. Chem. Chem. Phys.* **4**, 2932–2940 (2002).

23. Chichinin, A., et al. Photodissociation dynamics of $SOCl_2$. *Phys. Chem. Chem. Phys.* **7**, 301–309 (2005).

24. Rakhymzhan, A. & Chichinin, A. Excited Cl($^2P_{1/2}$) Atoms: Yield from the Photodissociation of $SOCl_2$ and Collisional Deactivation by NO_2 , CCl_3H, C_2H_4 , C_3H_6 , and $SOCl_2$. *J. Phys. Chem. A* **114**, 6586–6593 (2010).

25. Abulimiti, B., Hao, Q., Qin, C., Xiang, M. & Zhang, B. Three-Body photodissociation of thionyl chloride. *Chinese Journal of Chemical Physics* **31**, 257–262 (2018).

26. Lindquist, B. A. & Dunning, T. H. The nature of the SO bond of chlorinated sulfur–oxygen compounds. *Theor Chem Acc* **133**, 1443 (2014).

27. Ffrancon Williams & Koichi Nishikida. Electron Spin Resonance Spectra of OSeCI, OSCl, and OSBr. *Journal of Magnetic Resonance* **14**, 348–357 (1974).

28. Harrison E. Radford, F. David Wayne, & John M. Brown. Far Infrared Laser Magnetic Resonance Spectra of the ClSO and FSO Radicals in the Gas Phase. *Journal of Molecular Spectroscopy* **99**, 209–220 (1983).
29. Hirota, E. & Saito, S. Spectroscopy and structures of free radicals and molecular ions. *Res Chem Intermed* **7**, 353–388 (1987).
30. Chu, L.-K., Lee, Y.-P. & Jiang, E. Y. Detection of ClSO with time-resolved Fourier-transform infrared absorption spectroscopy. *The Journal of Chemical Physics* **120**, 3179–3184 (2004).
31. Blitz, M. A., Goddard, A., Ingham, T. & Pilling, M. J. Time-of-flight mass spectrometry for time-resolved measurements. *Review of Scientific Instruments* **78**, 034103 (2007).
32. Jr-Min Lin, J. & Chao, W. Structure-dependent reactivity of Criegee intermediates studied with spectroscopic methods. *Chem. Soc. Rev.* **46**, 7483–7497 (2017).
33. Shih, M.-C. & Chu, L.-K. Does Tetrahydrofuran (THF) Behave like a Solvent or a Reactant in the Photolysis of Thionyl Chloride (Cl_2SO) in Cyclohexane? A Transient Infrared Difference Study. *J. Phys. Chem. A* **122**, 5401–5408 (2018).
34. Korth, H.-G. Comment on “Does Tetrahydrofuran (THF) Behave like a Solvent or a Reactant in the Photolysis of Thionyl Chloride (Cl_2SO) in Cyclohexane? A Transient Infrared Difference Study”. *J. Phys. Chem. A* **123**, 7892–7894 (2019).
35. Li, Z. Ab Initio Study of the Electronic Structure of XSO and XSO_2 (X = F, Cl) Radicals. *J. Phys. Chem. A* **101**, 9545–9550 (1997).

36. Winiberg, F. A. F., Zuraski, K., Liu, Y., Sander, S. P. & Percival, C. J. Pressure and Temperature Dependencies of Rate Coefficients for the Reaction OH + NO_2 + M → Products. *J. Phys. Chem. A* **124**, 10121–10131 (2020).

37. Matthews, D. A., et al. Coupled-cluster techniques for computational chemistry: The CFOUR program package. *J. Chem. Phys.* **152**, 214108 (2020).

38. Kállay, M. & Gauss, J. Calculation of excited-state properties using general coupled-cluster and configuration-interaction models. *The Journal of Chemical Physics* **121**, 9257–9269 (2004).

39. Stanton, J. F. & Bartlett, R. J. The equation of motion coupled-cluster method. A systematic biorthogonal approach to molecular excitation energies, transition probabilities, and excited state properties. *The Journal of Chemical Physics* **98**, 7029–7039 (1993).

40. Kállay, M., et al. The MRCC program system: Accurate quantum chemistry from water to proteins. *J. Chem. Phys.* **152**, 074107 (2020).

41. McCaslin, L. & Stanton, J. Calculation of fundamental frequencies for small polyatomic molecules: a comparison between correlation consistent and atomic natural orbital basis sets. *Molecular Physics* **111**, 1492–1496 (2013).

42. Neese, F. & Valeev, E. F. Revisiting the Atomic Natural Orbital Approach for Basis Sets: Robust Systematic Basis Sets for Explicitly Correlated and Conventional Correlated *ab initio* Methods? *J. Chem. Theory Comput.* **7**, 33–43 (2011).

43. Gauss, J., Stanton, J. F. & Bartlett, R. J. Coupled-cluster open-shell analytic gradients: Implementation of the direct product decomposition approach in energy gradient calculations. *The Journal of Chemical Physics* **95**, 2623–2638 (1991).

44. Stanton, J. F. Many-body methods for excited state potential energy surfaces. I. General theory of energy gradients for the equation-of-motion coupled-cluster method. *The Journal of Chemical Physics* **99**, 8840–8847 (1993).
45. Stanton, J. F. & Gauss, J. Analytic energy gradients for the equation-of-motion coupled-cluster method: Implementation and application to the HCN/HNC system. *The Journal of Chemical Physics* **100**, 4695–4698 (1994).
46. Stanton, J. F. & Gauss, J. Analytic energy derivatives for the equation-of-motion coupled-cluster method: Algebraic expressions, implementation and application to the S1 state of HFCO. *Theoret. Chim. Acta* **91**, 267–289 (1995).
47. Tajti, A., et al. HEAT: High accuracy extrapolated *ab initio* thermochemistry. *The Journal of Chemical Physics* **121**, 11599–11613 (2004).
48. Bomble, Y. J., et al. High-accuracy extrapolated *ab initio* thermochemistry. II. Minor improvements to the protocol and a vital simplification. *The Journal of Chemical Physics* **125**, 064108 (2006).
49. Harding, M. E., et al. High-accuracy extrapolated *ab initio* thermochemistry. III. Additional improvements and overview. *The Journal of Chemical Physics* **128**, 114111 (2008).
50. Stanton, J. F. & Gauss, J. Analytic energy derivatives for ionized states described by the equation-of-motion coupled cluster method. *The Journal of Chemical Physics* **101**, 8938–8944 (1994).
51. Baklanov, A. V., Chesnokov, E. N. & Chichinin, A. I. Rate constants for the reactions of molecular iodine with Cl, SiCl3, and SiH3 at 298 K. *Int. J. Chem. Kinet.* **29**, 25–33 (1997).

52. Burkholder, J. B., et al. JPL Publication 19-5. Chemical Kinetics and Photochemical Data for Use in Atmospheric Studies. *JPL Publication* **19–5**, 2–7 (2020).

53. Sarka, K. & Nanbu, S. Total Absorption Cross Section for UV Excitation of Sulfur Monoxide. *J. Phys. Chem. A* **123**, 3697–3702 (2019).

54. Baulch, D.L., Duxbury, J, Grant, S.J., & Montague, D.C. Evaluated kinetic data for high temperature reactions. Volume 4 Homogeneous gas phase reactions of halogen- and cyanide- containing species. *J. Phys. Chem. Ref. Data* **10**, 1–129 (1981).

55. Groß, C. B. M., Dillon, T. J., Schuster, G., Lelieveld, J. & Crowley, J. N. Direct Kinetic Study of OH and O_3 Formation in the Reaction of $CH_3C(O)O_2$ with HO_2. *J. Phys. Chem. A* **118**, 974–985 (2014).

56. Müller, T., Vaccaro, P. H., Pérez-Bernal, F. & Iachello, F. The vibronically-resolved emission spectrum of disulfur monoxide (S2O): An algebraic calculation and quantitative interpretation of Franck–Condon transition intensities. *The Journal of Chemical Physics* **111**, 5038–5055 (1999).

57. Sander, S. P., Peterson, M., Watson, R. T. & Patrick, R. Kinetics studies of the hydrogen dioxide + hydrogen dioxide and deuterium dioxide + deuterium dioxide reactions at 298 K. *J. Phys. Chem.* **86**, 1236–1240 (1982).

58. Wang, B., Hou, H., Yoder, L. M., Muckerman, J. T. & Fockenberg, C. Experimental and Theoretical Investigations on the Methyl−Methyl Recombination Reaction. *J. Phys. Chem. A* **107**, 11414–11426 (2003).

59. Geoffrey S. Tyndall, John J. Orlando, & Carla S. Kegley-Owen. Rate Coefficients for Quenching of Cl(2P1/2) by Various Atmospheric Gases. *J. Chem. Soc. Faraday Trans.* **91**, 3055–3061 (1995).

60. Golden, D. M. The Reaction $Cl + NO_2 \rightarrow ClONO$ and $ClNO_2$. *J. Phys. Chem. A* **111**, 6772–6780 (2007).

61. Krasnopolsky, V. Chemical kinetic model for the lower atmosphere of Venus. *Icarus* **191**, 25–37 (2007).

62. Zhang, X., Liang, M. C., Mills, F. P., Belyaev, D. A. & Yung, Y. L. Sulfur chemistry in the middle atmosphere of Venus. *Icarus* **217**, 714–739 (2012).

Chapter 3—A-Band Spectrum of the ClSO Radical: Electronic Structure of the Sulfinyl Group

This chapter is reprinted and adapted with permission from J. Phys. Chem. A 2023, 127, 8374 - 8382. Copyright 2023, American Chemical Society.

3.1—Abstract

Sulfinyl radicals (RSO) play a critical role in fields ranging from biology to atmospheric chemistry, particularly in aerosol formation. We utilized gas-phase transient-absorption spectroscopy to record the UV-Vis absorption spectrum of the ClSO radical generated from the pulsed-laser photolysis of thionyl chloride at 248 nm (40 Torr and 292 K). We detected a weak absorption spectrum from 350–480 nm with a peak at 385 nm, partially resolved vibronic bands with a spacing of 226 cm^{-1}, and a peak cross-section σ(385 nm) = (7.6 ± 1.9) × 10^{-20} cm^2. From *ab initio* calculations at the EOMEE-CCSD/ano-pVQZ level, we assigned this band to both the $1^2A' \leftarrow X^2A''$ and $2^2A' \leftarrow X^2A''$ transitions. We modeled the spectrum as a sum of a bound-to-free transition to the $1^2A'$ state and a bound-to-bound transition to the $2^2A'$ state, with similar oscillator strengths; the prediction agreed well with the observed spectrum. We attributed the vibronic structure to a progression in the bending vibration of the $2^2A'$ state. Further calculations at the XDW-CASPT2 level predicted a conical intersection between the excited $1^2A'$ and $2^2A'$ potential energy surfaces near the Franck-Condon region. The geometry of the minimum energy conical intersection was similar to the ground-state geometry. The lack of structure on blue side could be evidence of a short excited state lifetime arising from the strong vibronic coupling. From simplified molecular orbital analysis, we attributed the ClSO spectrum to transitions involving the out-of-plane π/π^* orbitals along the SO bond and the in-plane orbital possessing σ/σ^* character along the SCl bond. We hypothesized that these orbitals are common to other sulfinyl radicals RSO, which would share a combination of a strong and a weak transition in the UV (near 300 nm) and visible (400 - 600 nm) regions.

3.2—Introduction

The oxidation of sulfur-oxide species (RSO_x), generated through reactions between oxygen and sulfinyl radicals (RSO), is important in many fields, including biology,[1,2] organic synthesis[3,4], and atmospheric chemistry[5]. For instance, an important source of sulfate aerosols in the Earth's atmosphere is believed to be regulated by RSO_x oxidation, with HSO[6] and SO_2[7,8] as intermediates in the formation of sulfates.[9] However, in the middle atmosphere of Venus, condensed sulfuric acid clouds have been observed[10] despite extremely low oxygen levels. The sulfate aerosol formation is attributed to the catalytic role of chlorine, involving in the oxidation of CO and SO to form CO_2 and SO_2.[11] To comprehend the mechanism of chlorine-catalysis of sulfinyl radical oxidation, direct kinetic measurements of sulfur species and chlorine in the laboratory need to be conducted along with theoretical calculations to provide chemical insights.

The sulfinyl chloride radical, ClSO, is the smallest sulfinyl radical containing a chlorine atom and represents an ideal system for high-level *ab initio* calculations.[12] Although the ClSO radical can be easily generated through the photolysis of thionyl chloride (Cl_2SO),[13,14] available spectroscopic measurements are limited to ground-state properties such as infrared (IR),[15] far-IR,[16] and electron paramagnetic resonance[17] spectra. Furthermore, relevant theoretical studies are scarce.[18] In the absence of suitable detection methods, kinetic investigations were limited to mass spectrometric detection.[19]

Recently, we observed a strong ultraviolet absorption spectrum of the ClSO radical in the gas phase near 300 nm range, which we assigned to the $1^2A'' \leftarrow X^2A''$ transition of the ClSO radical. We used the strong UV absorption to monitor ClSO and study the kinetics of the $ClSO + Cl \rightarrow Cl_2SO$ reaction at pressures ranging from 10 to 90 Torr at 292 K.[12]

Previous studies in cryogenic matrices[20–24] have shown that a few sulfinyl radicals exhibit both strong UV absorption near 300 nm and weak features near 400 nm, indicating that analogous weak features might also exist for ClSO. The goal of this work was to search for a longer wavelength spectrum of gas-phase ClSO by transient-absorption spectroscopy. We employed the same apparatus used to detect the shorter wavelength spectrum, a White-cell-based transient UV-Vis absorption spectrometer coupled into a flow reactor.[12] Radicals were generated by pulsed-laser photolysis and transient-absorption spectra were recorded in the 300–580 nm window. Low-lying excited electronic states were computed using Coupled-Cluster and Complete Active Space Perturbation Theory (CASPT2) methods. The observed spectra were then assigned by comparison with the results from the *ab initio* calculations. Additionally, a molecular orbital (MO)-based analysis was performed to provide chemical insight into the role of the Cl atom and the sulfinyl electronic structure in the ClSO radical.

3.3—Experimental Methods

The experimental instrument and the theoretical methods have been previously reported.[12] In short, a small stream of nitrogen (evaporated from liquid nitrogen) flowed through a bubbler containing Cl_2SO (Sigma-Aldrich, > 99%) held in a temperature-controlled bath at 292 K (Fisherbrand, Isotemp 4100). This mixture was then introduced into a flow reactor, whose pressure was monitored by a capacitance gauge (MKS 127AA-00100A) and controlled by a throttle valve (MKS type 153). The gas refreshing rate (MKS GM50A and 1179A) was slightly faster than the repetition rate of the photolysis laser (Coherent COMPex 205F, KrF). A broadband Xe plasma light source (LDLS, Energetiq EQ-99) was directed into a White cell (R = 140 cm, Acton Optics, ten passes, $L_{\mathrm{eff}} \approx 450$ cm). The light was then projected into a two-exit grating spectrograph (Acton SpectraPro 300i), which allowed both an image-intensified CCD (Princeton Instruments PI-MAX4, 1024 × 256) and a photomultiplier tube (Hamamatsu R928) to collect transmitted light simultaneously. A long-pass filter (Semrock LP02-257RU-30 × 40) was used to separate the photolysis beam from the probed beam to reduce background absorbance. For measurements longer than 520 nm, a long-pass filter (Thorlabs FEL0450) was placed in front of the entrance slit of the spectrometer to remove the second-order diffraction. The concentrations of Cl_2SO ranged from $(0.4–3) \times 10^{15}$ cm^{-3} and were balanced with N_2 for a total pressure of 40 Torr at a temperature of 292 K.

3.4—Theoretical Methods

All equation of motion coupled cluster (EOM-CCSD) calculations were performed using the CFOUR program suite,[25] with the exception of the unrestricted reference LR-CCSDT,[26] which was performed using the MRCC package.[27] All calculations made use of the ano-pVQZ basis set[28] which has coverage from H-Ar, as the use of atomic natural orbital (ANO) basis sets have been found to be exceptionally effective for calculating harmonic frequencies.[29] The frozen-core approximation was applied to all calculations since the ano-pVXZ basis sets were not optimized for core correlation. The ground state was optimized using CCSD with an unrestricted Hartree-Fock (UHF) reference, while the $1^2A'$ and $2^2A'$ excited states were optimized using EOMEE-CCSD. To explore the possible effects of spin contamination, we also employed restricted Hartree-Fock (RHF) references to optimize the $1^2A'$ and $2^2A'$ excited states using the EOMEA ($ClSO^+$ cation reference) and EOMIP ($ClSO^-$ anion reference) approaches, respectively. The ground state was also optimized using these two methods for calculations of the adiabatic transition energies.

Although the combination of EOM-CCSD and EOM-CCSDT provide a highly accurate treatment of dynamic correlation in the excited state, they fail to describe the behavior of the adiabatic states in a very small region about the conical intersection, yielding complex-valued energies due to the non-Hermitian character of the effective Hamiltonian.[30] To characterize the splitting of the adiabatic states in the vicinity of the conical intersection, we turned to multireference perturbation theory, in particular XDW-CASPT2.[31] While CASPT2 is ultimately a perturbation theory and describes dynamic correlation less accurately than coupled-cluster-based methods, its extended multistate variants (e.g., XDW-CASPT2 and XMS-CASPT2) correctly describe the topology of conical intersections. XDW-CASPT2 is especially suited for this purpose, as it interpolates between a state-specific and state-averaged Fock operators as the adiabatic states approach each other and mix.

The minimum energy conical intersection (MECI) between the $1^2A'$ and the $2^2A'$ states was located via XDW-CASPT2 calculations based on a CASSCF(7,5) reference averaged over the three lowest electronic states as implemented in OpenMolcas.[32–34] The conical intersection was located using the projected constrained optimization approach,[35,36] in which the average energy of the two states is minimized subject to the constraints[37] that the adiabatic energy difference is zero and a dummy constraint which prevents motion along the analytically computed[38] derivative coupling vector. An imaginary shift of 0.05 eV was applied for all calculations to avoid intruder states. The weighting factor used for the dynamically weighted Fock matrix was as described in Ref. 39, corresponding to the OpenMolcas keywords of DWType = 3 and DWMS = 1.0. The conical intersection was characterized in the branching plane by displaced geometries in the plane defined by the x and y vectors, which span the same plane as the g and h vectors and are related to them by rotation.[37] The displacements formed a grid in polar coordinates, with a spacing of 0.05 Å in R and 20° in θ. Parallel computations were aided by the use of GNU parallel.[40]

The absolute cross-section as a function of wavelength was simulated in a rough approximation neglecting coupling between the 1^2A' and 2^2A' states as the sum of two independent spectral contributions. Franck-Condon factors for the 2^2A' ← X^2A" transition at 0 K including Duschinsky rotation effects were calculated using the ezFCF package,[41] using vibrational frequencies and 0-0 transition energies taken from the EOMEE-CCSD/ano-pVQZ calculations. The absolute contribution to the cross-section is given by

$$\sigma_{2^2A'}(\bar{\upsilon}) = \frac{2\pi^2}{3hc\varepsilon_0 n_r \bar{\nu}} \left|\boldsymbol{\mu}_{i,f}\right|^2 \sum_k \bar{\nu}_k^2 |\langle\chi_0|\chi_k\rangle|^2 \frac{1}{\sigma\sqrt{2\pi}} e^{\frac{-(\bar{\nu}-\bar{\nu}_k)^2}{2\sigma^2}}$$

where σ is an empirical broadening parameter chosen to correspond to a full-width half-maximum of 100 cm^{-1}. The 1^2A' contribution to the spectrum was estimated using a multidimensional extension of the reflection principle,[42] and is given by

$$\sigma_{1^2A'}(\bar{\upsilon}) = \frac{2\pi^2}{3hc\varepsilon_0 n_r} \left|\boldsymbol{\mu}_{i,f}\right|^2 \sqrt{\frac{\beta}{\pi}}\, \bar{\nu}\, exp\left(-\beta\left(\Delta E_{vertical} - \frac{\sum_i \bar{\nu}_i}{4} - \bar{\nu}\right)^2\right)$$

where β-1 is the norm of the gradient of the upper state in cm-1 (see Ref 42), and the $\bar{\nu}_i$ are the ground-state vibrational frequencies (expressed in cm-1). EOMEE-CCSD was used for the vertical excitation energy, excited state gradient, and transition dipole moment. The ground state CCSD vibrational frequencies were used for the $\bar{\nu}_i$.

Orbitals were visualized with the IboView package,[43] while vibrational arrow diagrams were generated with the PyVibMS plugin[44] to pymol.[45]

3.5—Results

3.5.1—Experimental ClSO A-Band Spectrum

Figure 1 shows the representative spectra of the Cl_2SO/N_2 photolysis system at 40 Torr, recorded at a delay time of 100 μs. We have previously reported the strong absorption below 320 nm, which has a maximum at 303 nm, and assigned it to the $1^2A'' \leftarrow X^2A''$ transition, the B-Band of the ClSO radical.[12]

We found another weak absorption, with a maximum peak position near 385 nm and exhibiting a series of vibronic bands. The apparent threshold of this weak absorption feature is around 480 nm. The slight variations in baseline above 500 nm show the uncertainty in baseline under high [Cl_2SO]. The precursor may also have a small absorption (Figure S1). A fit to the partially resolved vibrational progression observed in the experiment yielded an average spacing of 226 cm^{-1}. The progression was linear over the range observed; as shown in Figure 1, fitting to a quadratic function was not a statistically significant improvement.

The weak absorption band centered near 385 nm has a decay behavior identical to the absorption near 303 nm to within the experimental uncertainty (Figure S2). The intensity was found to be proportional to the concentration of Cl_2SO in the reactor (Figure S3−S4) when [Cl_2SO] < 1.3×10^{15} molecule cm^{-3}. The concentrations of Cl_2SO used in this experiment were quite high ([Cl_2SO] ≈ 3×10^{15} molecules cm^{-3}) to ensure a large enough transient signal. However, this high concentration also resulted in strong absorption of the photolysis laser (σ(248nm) = 7.05×10^{-18} cm^2,[46] L = 45 cm, T = 37.7%), leading to inhomogeneous radical formation throughout the flow reactor along the excimer path (Figure S4). As a result of these conditions, we did not attempt a quantitative kinetic analysis of the time-dependent data to obtain rate constants. Based on the concentration dependence and temporal behavior at distinct wavelengths, we tentatively assigned the origin of the weak band to ClSO radicals.

We calibrated the absolute cross-section of the weak band near 385 nm from the absorbance of the $1^2A'' \leftarrow X^2A''$ transition in the 310–320 nm range, which has a peak cross-section, $\sigma(303\ \mathrm{nm}) = (2.0 \pm 0.5) \times 10^{-18}\ \mathrm{cm}^{-2}$.[12] Figure S5 demonstrates that the weak band has a maximum absorption cross-section $\sigma(385\ \mathrm{nm}) = (7.6 \pm 1.9) \times 10^{-20}\ \mathrm{cm}^2$ near 385 nm (1 standard deviation).

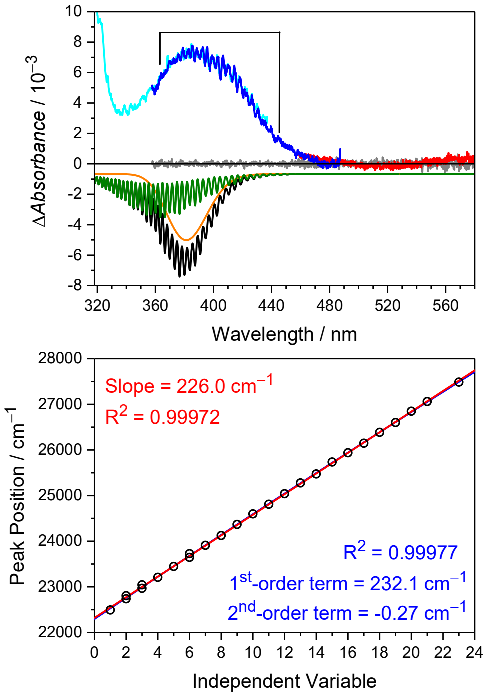

Figure 3.1. (Upper Panel) The recorded spectra of the Cl_2SO/N_2/248 nm system at 100 μs after pulsed laser (exposure time = 117.5 μs, averaged for 12,288 shots) at 40 Torr and 292 K. Cyan, blue, and red lines represent spectra at different grating angles (center wavelengths of 370 nm, 420 nm, and 520 nm), while the gray lines show the background noise without Cl_2SO. The black simulated spectra downward is the sum of contributions from both the $1^2A'$ (orange) and $2^2A'$ (olive, stick spectra convoluted with a Gaussian function with FWHM = 100 cm^{-1}) states. The comparison between experimental and theoretical absolute cross-sections is shown in Figure S5. (Lower Panel) Linear and quadratic fits to the observed positions of the vibrational peaks, within the marked region.

3.5.2—EOM-CCSD Calculations

Table 1 summarizes the results of coupled-cluster point calculations for the X^2A'' ground state and the two lowest lying $^2A'$ excited states. The $1^2A'$ state arises from the alpha singly occupied molecular orbital (SOMO)-LUMO transition, and the $2^2A'$ state from the beta SOMO-1 to SOMO transition. All three states have bound minima. The adiabatic transition energy of the $2^2A'$ state was found to be 20463 cm^{-1}, higher than that of the $1^2A'$ state (16122 cm^{-1}); there was thus no change in the energy ordering of the $^2A'$ excited states. The minimum energy of the $2^2A'$ state is predicted to be higher than the bond dissociation energy D_0(Cl–SO) = 19048 cm^{-1} using the HEAT-345(Q) method[47–50] (see Table S1), while the minimum of the $1^2A'$ state is predicted to be below D_0(Cl–SO). The observed absorption band lies well above dissociation.

The $1^2A'$ excited state is characterized by a large ClSO angle and a longer ClS bond length than those of the X^2A'' state. The $2^2A'$ excited state has an almost 90° ClSO angle and a longer SO bond length and is closer to the geometry of the ground state. Both $^2A'$ excited states have lower bending frequencies (214 cm^{-1} and 227 cm^{-1}) than the ground state (316 cm^{-1}). The $1^2A'$ state has a lower ClS stretching frequency (333 cm^{-1}) than the ground state, while $2^2A'$ has a lower SO stretching frequency (735 cm^{-1}); both results are consistent with the respective bond length changes. Further calculations utilizing closed-shell references produced results that were similar to the EOMEE calculations, suggesting minimal spin contamination effects.

Table 3.1. Summary of the calculations of ClSO for Geometries, Harmonic Frequencies, Adiabatic Transition Energies Δ*E* Relative to the Ground State, and the 0-0 Transition Energies.

SCF Reference		UHF/EOMEE			RHF/EOMIP(Anion)		RHF/EOMEA(Cation)	
Geometry Optimized		X ^{2}A''	2 ^{2}A'	1 ^{2}A'	X ^{2}A''	2 ^{2}A'	X ^{2}A''	1 ^{2}A'
Geometry [a]	*r*(S–O) / Å	1.461	1.672	1.459	1.464	1.643	1.453	1.460
	r(Cl–S) / Å	2.046	2.013	2.276	2.034	2.012	2.035	2.259
	∠(ClSO) / degree	109.25	91.50	152.69	109.42	90.19	109.57	149.78
Frequency [a] / cm^{-1}	ClSO bending	316.3	226.5	214.3	320.6	221.0	323.1	232.9
	ClS stretching	515.5	550.7	333.3	541.8	544.6	533.8	345.1
	SO stretching	1199.5	735.4	1197.7	1190.3	802.8	1248.3	1195.4
Δ*E* / cm^{-1}	CCSD/ano-pVQZ	0	20697 (20742)[b]	18517 (16759)[b]	0	21027 (20463)[c]	0	17558 (16122)[c]
0–0 transition energy/cm^{-1} [nm]		-	20482 [488.2]	16616 [601.8]	-	20221 [494.5]	-	15956 [626.7]

[a] Optimization and frequency at the CCSD/ano-pVQZ level.

[b] Correction for the triples by ΔE_{HLC} = CCSDT/ano-pVDZ – CCSD/ano-pVDZ similar to Ref. 47

[c] At CCSDT/ano-pVQZ level.

3.5.3—Assignment of 385 nm Spectrum

Both low-lying A' excited states are predicted to have similar vertical excitation energies consistent with the observed band at 385 nm.[12] The transition to the 1^2A' state is dissociative, while the transition to the 2^2A' is bound. The observed cross-section is within a factor of two of the theoretical absolute cross-section maximum, $\sigma_{\mathrm{the}}(377\ \mathrm{nm}) = 1.8 \times 10^{-19}\ \mathrm{cm}^2$. The cross-section relative to that of the strong B-Band is consistent with the oscillator strengths that we previously predicted. We found $f(1^2\mathrm{A}') = 3.89\times10^{-4}$, $f(2^2\mathrm{A}') = 2.88\times10^{-4}$ and $f(1^2\mathrm{A}'') = 1.22\times10^{-2}$ for transition to the higher excited states.[12] The ratio of the predicted oscillator strengths is $(f(1^2\mathrm{A}'')/(f(1^2\mathrm{A}') + f(2^2\mathrm{A}'))= 18.0$, consistent with the ratio of the observed absolute cross-sections at the peaks, $\sigma(305\ \mathrm{nm})/\sigma(385\ \mathrm{nm}) = 2.0\times10^{-18}\ \mathrm{cm}^{-2}/ 7.6\times10^{-20}\ \mathrm{cm}^{-2} = 26.3$.

The bending frequencies predicted for both ^{2}A' states agree well with the experimentally observed vibrational progression of 266 cm^{-1} (see Figure 1). In addition, Figure 2 shows doublet peaks at 422 nm, 435 nm, and 439 nm, which may be attributed to the difference between the SO stretching frequency and three times the bending frequency of 2^2A' state. For instance, the doublet peak at 435 nm could correspond to the $(4,2,0) \leftarrow (0,0,0)$ and $(3,5,0) \leftarrow (0,0,0)$ transitions, leading to an estimated frequency for the SO stretching mode of 755 cm^{-1}. From the calculated Franck-Condon contour, we extrapolated the origin to be roughly near 490 nm (20400 cm^{-1}), which is consistent with the 0–0 transition energy of the 2^2A' state shown in Table 1.

The observed vibrational structure disappears on the blue side, while the simulated spectrum exhibits a clear vibrational progression of 2^2A' state across the whole band. The peak broadening on the blue side might be due to congestion and anharmonicity or decreases in the lifetime of the 2^2A' excited state caused by internal conversion (*vide infra*, see "Influence of the Conical Intersection").

A few peaks within the 320–360 nm range (Figure S6) were also observed, which have a small spacing of approximately 367 $\mathrm{cm^{-1}}$ and large spacing of 1060 $\mathrm{cm^{-1}}$. These energy differences are close to the calculated ClS stretching and SO stretching frequencies of the $1^2A'$ state and may warrant further theoretical investigation.

As a first-order approximation, we modeled the spectrum with the EOMEE-CCSD/ano-pVQZ results, assuming that the spectrum was the incoherent sum of the $1^2A' \leftarrow X^2A''$ and $2^2A' \leftarrow X^2A''$ transitions weighted by the computed oscillator strengths (see Figure 1). We treated the bound-to-bound transition to the $2^2A'$ state as two independent displaced harmonic oscillator models based on the minimum energy geometries of the X^2A'' and $2^2A'$ states adopted from the EOMEE-CCSD/ano-pVQZ calculations including Duschinsky rotation and thermal effects at 0 K (Figure S7). We simulated the $1^2A' \leftarrow X^2A''$ transition using a multidimensional extension of the reflection principle. The two states had roughly equal contributions.

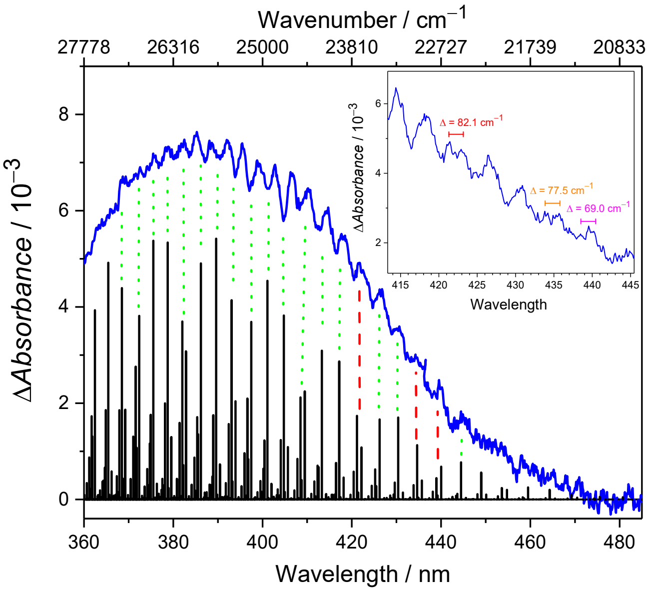

Figure 3.2. A closer look at the structure of the weak absorption band in the 360–480 nm range. A few doublet peaks were observed, yielding an average spacing of 76 cm^{-1}. The stick spectrum displays the intensities predicted for excitation to the $2^2A'$ state, incorporating Franck-Condon factors and thermal population effects at 0 K. The energy of the computed transition origin has been shifted to the red by 870 cm^{-1} for alignment with the vibronic progression of experimental spectrum (green dotted lines), while the red dashed lines indicate predicted doublets. Inset is a magnification of the spectrum between 415 and 445 nm.

3.5.4—Prediction of a Conical Intersection between the $1^2A'$ and $2^2A'$ States

Our previous calculations found that the vertical excitation energies of the two $^2A'$ states were very close in energy. This result suggested that a conical intersection between $1^2A'$ and $2^2A'$ states might exist near the ground state geometry. To investigate this phenomenon, we generated a cut of the bending potential energy curve by linearly connecting the geometries of the X^2A'', $1^2A'$ and $2^2A'$ states (Figure S8). We employed the EOMIP and EOMEA approaches to treat the $1^2A'$ and $2^2A'$ independently (Figure S9). In addition, the EOMEE/ano-pVTZ calculation failed to converge at the upper state (Figure S10).

Table 3.2. Summary the geometries and energy difference relative to the ground state, ΔE, calculated at the XDW-CASPT2(7,5) level.

Geometry Optimized		$X\,^2A''$	$1\,^2A'$	$2\,^2A'$	MECI
Geometry	r(S–O) / Å	1.446	1.480	1.688	1.593
	r(Cl–S) / Å	2.007	2.259	1.997	2.010
	∠(ClSO) / degree	111.8	156.1	93.0	119.2
	x (Branching Space) / Å	−0.0283	−0.4444	0.2473	0
	y (Branching Space) / Å	−0.0549	0.1769	−0.1508	0
	z (Seam Space) / Å	0.1611	−0.4138	0.3517	0
ΔE / cm^{-1}		0	14431	23198	26414

To locate the conical intersection, we explored the lowest three potential energy surfaces (PES) of the ClSO radical using XDW-CASPT2[31,39] with seven electrons in five orbitals CASSCF reference. The active orbitals at the ground state equilibrium geometry are pictured in Figure 5. The resulting equilibrium geometries and relative energies are summarized in Table 2.

We found a sloped-type conical intersection of the $1^2A'$ and $2^2A'$ states, as depicted in Figure 3, with a minimum energy conical intersection (MECI) at 26414 cm^{-1}, close to the peak of the absorption. The geometries of the MECI and the ground state are similar with the SO bond slightly longer. Indeed, we found the change between the X^2A'' and MECI in the branching space is small (0.06 Å, Table 2) with a larger change in seam space, indicating that the two $^2A'$ excited state PES do cross near the Franck-Condon region, although the MECI is slightly far away from the ground-state geometry.

The corresponding motions of the **x** and **y** vectors[37] in the branching space as well as the motions in seam space are also illustrated in Figure 4. Motion along the **x** vector (large contribution from the anti-symmetric stretch) on the lower surface lowers the energy, presumably leading to the 1A' well (contracting the SO bond and elongating the SCl bond). Motion along the **y** vector mainly consisted of the symmetric stretching.

The bending mode is the primary motion along the seam space (Figure 4), *i.e.*, the degeneracy of the conical intersection is preserved as the molecule bends. The bending motion thus has the weakest vibronic coupling among the three vibrational modes. As a result, we expect the lifetimes of the bending vibronic excited states to be longer than other modes, consistent with the observation of the bending motion as the most prominent structural feature in the experimental spectrum.

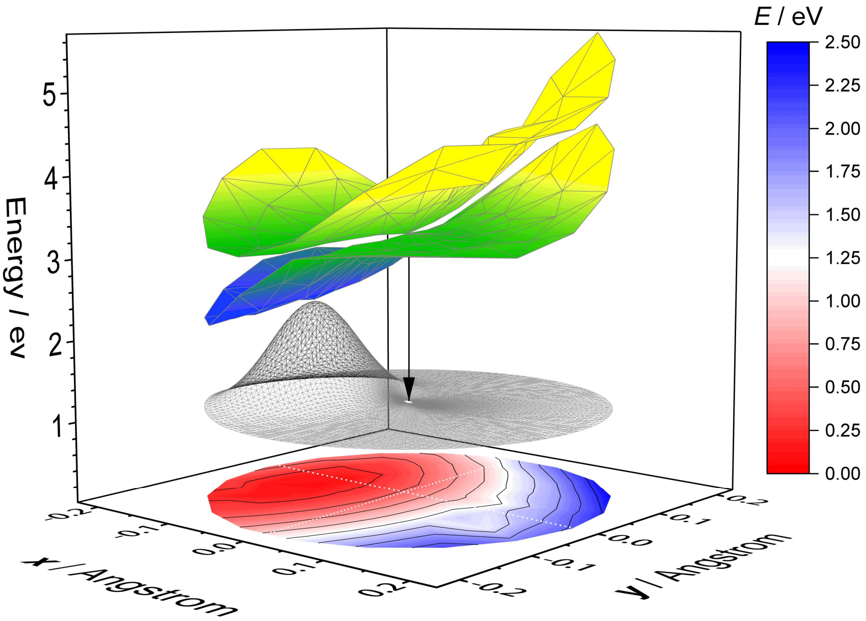

Figure 3.3. The adiabatic potential energy surface of the ground state and two excited $^2A'$ states of the ClSO radical in the 2D branching space (x, y; see Figure 4) computed at the XDW-CASPT2(7,5)-3SA level near the MECI geometry (x = 0, y = 0). The meshed line shows the profile of the ground-state vibrational wavefunction. The black arrow shows the vertical transition from the MECI to the ground-state PES (which is flattened for clarity; the color bar to the right gives the energy scale of the ground-state PES contours).

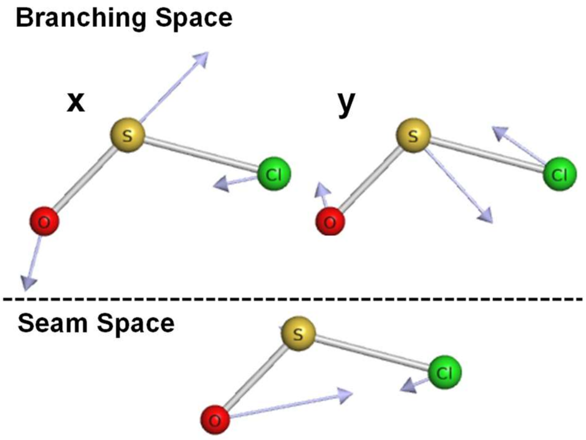

Figure 3.4. The corresponding vibrational motions of the seam space (the set of geometries where the 1^2A' and 2^2A' states are degenerate) and the branching space (the complement of seam space) near the MECI geometry.

3.6—Discussion

3.6.1—Influence of the Conical Intersection

Our current time-independent, low-resolution absorption spectrum does not provide more information about the interactions between both A' states near the conical intersection. We attributed the observed structure to the 2^2A' ← X^2A" state, but both the 1^2A' and 2^2A' states contribute to the observed band. While we simulated the spectrum as an incoherent excitation of the two adiabatic states, the true excitation process produces a superposition of the two states, and the coefficients of each state vary with energy, in part due to changing vibronic coupling across the band. Additionally, the excited wave packet would undergo non–adiabatic dynamics on the coupled 1^2A' and 2^2A' states, especially near conical intersection, resulting in a shorter lifetime and account for the loss of vibrational structure toward the blue side of the band.

The predominant Franck-Condon active mode in the vibrational progression of the observed spectrum is the ClSO bending, consistent with the prediction of the bending mode as the motion along the seam space. However, broadening on the blue side and observation of the bending progression can result from other effects, and can provide only circumstantial evidence for the presence of a conical intersection.

The fate of the excited state is unclear. The molecule excited to the $2^2A'$ state could relax to the lower $1^2A'$ state via the conical intersection along the **x** branch; subsequent collisions could further relax the molecule below the dissociation limit into the bound $1^2A'$ well, at which point the molecule could reach the ground state by internal conversion, collisional quenching or fluorescence.

To quantitatively predict the effects from the conical intersection on the observed spectrum is a challenging question and goes beyond the scope of this study. Use of a single-shot vibronic coupling model based on EOM-CCSD in the spirit of Ichino et al.[51] is complicated by the lack of a single, closed-shell, non-interacting reference state. Furthermore, the two electronic states share the same irreducible representation, leading to orbital mixing at the SCF level resulting in diabats which hold little chemical significance.

3.6.2—Molecular Orbital Diagram of ClSO Radical

Figure 5 summarizes the valence electronic structure of the ClSO radical. To construct this MO diagram, we used the ionization energies of the SO molecule (10.3 eV)[52] and Cl atom (13.0 eV)[53] to establish the relative energy positions.

Figure S11 depicts the nine MO resulting from the combination of 6σ, 2π, 2π*, and 7σ orbitals of SO, along with the 3*p* orbitals of the Cl atom under C_s symmetry. These orbitals can be broadly classified as bonding, anti-bonding, and non-bonding. The term non-bonding here is used loosely, referring to orbitals which exhibit both bonding and anti-bonding characteristics simultaneously along distinct chemical bonds.

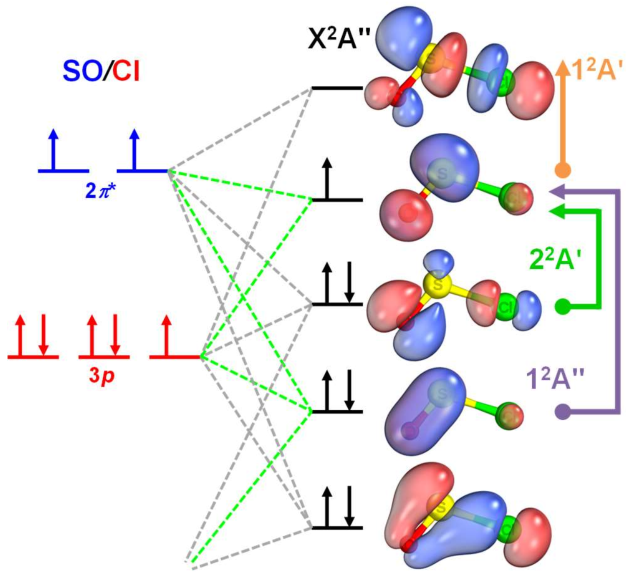

Figure 3.5. Schematic MO diagram showing the active space orbitals of the ClSO radical (top view) used in the XDW-CASPT2 calculation. Vertical and horizontal arrows indicate transitions to excited states for alpha and beta electrons. The green lines connect orbitals with the out-of-plane orientation.

For instance, the second occupied molecular orbital (SOMO-1) is a combination of an in-plane π* orbital along the SO bond and a σ orbital along the ClS bond. This can be interpreted as the SO moiety being stabilized by donating electrons from a π* orbital into the 3*p* orbital of the Cl atom. We may expect that the reactivity of the ClSO radical does not change significantly respect to the SO molecule, supported by the nearly identical SO bond length compared to free SO molecules (r_{SO} = 1.48 Å).[54] Since the ClSO + Cl → Cl_2SO reaction has been reported,[12] we expect that the association reaction of SO + Cl → ClSO also occurs.

This MO analysis of the ClSO radical provides insights into the electronic structure of other sulfinyl radicals. This is because the ionization energy of the 3*p* orbitals of the Cl atom is similar to the ionization energies of H, C, N, and O atoms;[55] also, a radical species usually possesses seven electrons around the radical center, occupying three perpendicular orbitals similar to those of the Cl atom.

We predict that transitions from the SOMO-1 to the SOMO orbital are likely to occur commonly in other sulfinyl radicals and will resemble the $2^2A' \leftarrow X^2A''$ transition observed in ClSO radicals. Furthermore, a strong $\pi^*_{SO} \leftarrow \pi_{SO}$ transition will also be present, similar to the ClSO $1^2A'' \leftarrow X^2A''$ transition. Indeed, the literature has reported the presence of these two distinct transitions in certain sulfinyl radicals, as summarized in Table 3.

Table 3.3 Summary of the UV-Vis absorption band positions of distinct sulfinyl radicals (RSO).

Unit / nm	$\pi^*_{SO} \leftarrow \pi_{SO}$	SOMO ← SOMO-1	Sample Phase
SO	190 – 240	-	Gas[56]
H–SO		520 – 960[a]	Gas[57]
HO–SO	~270	300 – 500	Ne-matrix[21]
H_3C–SO	260 – 300	450 – 635	Ar-matrix[20]
F_3C–SO	250 – 300	490 – 610	Ar-matrix[23]
C_6H_5–SO	260 – 350 ~300	410 – 470 ~450	Ar-matrix[22] Solution(C_6H_{12})[58]
$H_2CC(H)$–SO	240 – 310	350 – 490	N_2-matrix[24]
Cl–SO	260 – 320	350 – 460	Gas

[a] Chemiluminescence Emission Spectrum

Peroxyl radicals (RO_2) are approximately isoelectronic molecules of sulfinyl radicals. Experiments have shown that two transitions within the near-IR and UV-Vis regions are commonly observed in peroxyl radicals. Weisman and Head-Gordon[59] have successfully explained the observed trend in band positions using a MO picture.

Building upon similar concepts, we have concluded that the $\pi^*_{SO} \leftarrow \pi_{SO}$ transition in sulfinyl radicals occurs at a similar band position due to the minimal mixing of orbital character from the substitution group. Conversely, the band positions of SOMO ← SOMO-1 transitions cover a wide range of wavelengths because the energy of the SOMO-1 orbital dependents on the characteristics of the substitution groups.

It is noteworthy that the chemiluminescence spectrum of HSO has been detected[57] in the visible range for the SOMO ← SOMO-1 transition,[60] which suggests that ClSO radical might fluoresce after excitation to the A-band and could work as a better tool to study the chemical reactivity and kinetics

3.7—**Conclusions**

In this work, we recorded the UV-Vis absorption spectrum of the ClSO radical in the gas phase, in the 320 - 500 nm range at 40 Torr and 292K, denoted the A-Band. We observed a new, weak band having a partially resolved vibrational progression with an average spacing of 226 cm^{-1}. We determined the peak cross-section by calibrating with the cross-section of the much stronger B-Band at 303 nm.

We assigned the band as an excitation to the continuum of the $1^2A'$ excited state and the bound $2^2A'$ excited state. Using the EOM-CCSD/ano-pVQZ method, we calculated the properties of the two doublet excited states in this region, both with A' symmetry in the C_s point group. Both states could contribute to the absorption intensity since they have similar vertical excitation oscillator strengths. The $1^2A'$ excited state had a minimum below the dissociation limit and possessed a larger bond angle and longer ClS bond length, while the $2^2A'$ excited state lying above the dissociation limit exhibited a nearly 90° bond angle and a longer SO bond length. We simulated the spectrum as a sum of the bound-free $1^2A' \leftarrow X^2A''$ transition and the bound-bound $2^2A' \leftarrow X^2A''$ transition. By comparing the calculated harmonic frequency and predicted 0-0 transition energy, we assigned the observed vibronic progression to the bending mode of the $2^2A' \leftarrow X^2A''$ transition.

We conducted XDW-CASPT2 calculations and identified a conical intersection between the $1^2A'$ and $2^2A'$ excited states. The geometry of the MECI was found to be similar to the ground-state geometry, indicating that the conical intersection was near the Franck-Condon region of the A-Band transition, suggesting that the two $^2A'$ excited states will mix due to strong vibronic coupling; a short lifetime of the $2^2A'$ state is expected and could account for the unresolved vibrational progression on the blue side of the band.

The observed spectrum provides only indirect evidence for the presence of this conical intersection. A complete theoretical understanding of the spectroscopic effects of this phenomenon will require accurate descriptions of the PES, vibronic couplings, and dynamical effects. Experimentally, the existence of the conical intersection could be demonstrated by high-resolution spectra, fluorescence spectra, and probes of possible photodissociation dynamics (e.g., molecular-beam photofragment-translational spectroscopy or stimulated Raman spectroscopy).

Finally, we have constructed a simplified MO diagram to illustrate our understanding of the electronic structure of the ClSO radical, which also highlights similarities to other sulfinyl radicals. This diagram serves as a useful tool in understanding the trends of the observed band positions, considering the effects of substitution groups on the orbital characteristics. In general, species containing the sulfinyl group can be anticipated to display strong absorption around 300 nm, while weaker bands with distinct features are expected within the range of 400 - 600 nm.

3.8—References

1. Bonini, M. G. & Augusto, O. Carbon Dioxide Stimulates the Production of Thiyl, Sulfinyl, and Disulfide Radical Anion from Thiol Oxidation by Peroxynitrite. *Journal of Biological Chemistry* **276**, 9749–9754 (2001).
2. Schöneich, C. Sulfur Radical-Induced Redox Modifications in Proteins: Analysis and Mechanistic Aspects. *Antioxidants & Redox Signaling* **26**, 388–405 (2017).
3. El-Sakka, I. A. & Hassan, N. A. Synthetic uses of thionyl chloride. *Journal of Sulfur Chemistry* **26**, 33–97 (2005).
4. Zhang, Z., Wang, X., Sivaguru, P. & Wang, Z. Exploring the synthetic application of sulfinyl radicals. *Org. Chem. Front.* **9**, 6063–6076 (2022).
5. Mardyukov, A. & Schreiner, P. R. Atmospherically Relevant Radicals Derived from the Oxidation of Dimethyl Sulfide. *Acc. Chem. Res.* **51**, 475–483 (2018).
6. Iraqi, M., Goldberg, N. & Schwarz, H. Structural Characterization of the Atmospherically Important Sulfur Compounds HSO.bul. and SOH.bul. by Charge Reversal and Neutralization-Reionization Mass Spectrometry. *J. Phys. Chem.* **98**, 2015–2017 (1994).
7. Wallace, P. J. & Edmonds, M. The Sulfur Budget in Magmas: Evidence from Melt Inclusions, Submarine Glasses, and Volcanic Gas Emissions. *Reviews in Mineralogy and Geochemistry* **73**, 215–246 (2011).
8. Visioni, D., Pitari, G. & Aquila, V. Sulfate geoengineering: a review of the factors controlling the needed injection of sulfur dioxide. *Atmos. Chem. Phys.* **17**, 3879–3889 (2017).
9. Saxena, P. & Seigneur, C. On the oxidation of SO2 to sulfate in atmospheric aerosols. *Atmospheric Environment (1967)* **21**, 807–812 (1987).

10. Zhang, X., Liang, M. C., Mills, F. P., Belyaev, D. A. & Yung, Y. L. Sulfur chemistry in the middle atmosphere of Venus. *Icarus* **217**, 714–739 (2012).

11. DeMore, W. B. & Yung, Y. L. Catalytic Processes in the Atmospheres of Earth and Venus. *Science* **217**, 1209–1213 (1982).

12. Chao, W., Jones, G. H., Okumura, M., Percival, C. J. & Winiberg, F. A. F. Spectroscopic and Kinetic Studies of the ClSO Radical from Cl_2SO Photolysis. *J. Am. Chem. Soc.* **144**, 20323–20331 (2022).

13. Baum, G., Effenhauser, C. S., Felder, P. & Huber, J. R. Photofragmentation of thionyl chloride: competition between radical, molecular, and three-body dissociations. *J. Phys. Chem.* **96**, 756–764 (1992).

14. Wang, H., Chen, X. & Weiner, B. R. Laser photodissociation dynamics of thionyl chloride: concerted and stepwise cleavage of S-Cl bonds. *J. Phys. Chem.* **97**, 12260–12268 (1993).

15. Chu, L.-K., Lee, Y.-P. & Jiang, E. Y. Detection of ClSO with time-resolved Fourier-transform infrared absorption spectroscopy. *The Journal of Chemical Physics* **120**, 3179–3184 (2004).

16. Harrison E. Radford, F. David Wayne, & John M. Brown. Far Infrared Laser Magnetic Resonance Spectra of the ClSO and FSO Radicals in the Gas Phase. *Journal of Molecular Spectroscopy* **99**, 209–220 (1983).

17. Ffrancon Williams & Koichi Nishikida. Electron Spin Resonance Spectra of OSeCI, OSCl, and OSBr. *Journal of Magnetic Resonance* **14**, 348–357 (1974).

18. Li, Z. Ab Initio Study of the Electronic Structure of XSO and XSO_2 (X = F, Cl) Radicals. *J. Phys. Chem. A* **101**, 9545–9550 (1997).

19. Blitz, M. A., Goddard, A., Ingham, T. & Pilling, M. J. Time-of-flight mass spectrometry for time-resolved measurements. *Review of Scientific Instruments* **78**, 034103 (2007).

20. Reisenauer, H. P., Romański, J., Mlostoń, G. & Schreiner, P. R. Matrix isolation and spectroscopic properties of the methylsulfinyl radical CH3(O)S˙. *Chem. Commun.* **49**, 9467 (2013).

21. Lu, B., et al. Spectroscopic Characterization of $HSO_2^{\bullet}$ and $HOSO^{\bullet}$ Intermediates Involved in SO_2 Geoengineering. *J. Phys. Chem. A* **125**, 10615–10621 (2021).

22. Xu, J., et al. Phenylsulfinyl Radical: Gas-Phase Generation, Photoisomerization, and Oxidation. *J. Am. Chem. Soc.* **140**, 9972–9978 (2018).

23. Wu, Z., et al. The Trifluoromethyl Sulfinyl and Oxathiyl Radicals. *Chem. Eur. J.* **24**, 1505–1508 (2018).

24. Wu, Z., et al. Spectroscopic characterization and photochemistry of the vinylsulfinyl radical. *Phys. Chem. Chem. Phys.* **23**, 16307–16315 (2021).

25. Matthews, D. A. *et al.* Coupled-cluster techniques for computational chemistry: The CFOUR program package. *J. Chem. Phys.* **152**, 214108 (2020).

26. Kállay, M. & Gauss, J. Calculation of excited-state properties using general coupled-cluster and configuration-interaction models. *The Journal of Chemical Physics* **121**, 9257–9269 (2004).

27. Kállay, M., et al. The MRCC program system: Accurate quantum chemistry from water to proteins. *J. Chem. Phys.* **152**, 074107 (2020).

28. Neese, F. & Valeev, E. F. Revisiting the Atomic Natural Orbital Approach for Basis Sets: Robust Systematic Basis Sets for Explicitly Correlated and Conventional Correlated *ab initio* Methods? *J. Chem. Theory Comput.* **7**, 33–43 (2011).

29. McCaslin, L. & Stanton, J. Calculation of fundamental frequencies for small polyatomic molecules: a comparison between correlation consistent and atomic natural orbital basis sets. *Molecular Physics* **111**, 1492–1496 (2013).
30. Köhn, A. & Tajti, A. Can coupled-cluster theory treat conical intersections? *The Journal of Chemical Physics* **127**, 044105 (2007).
31. Battaglia, S. & Lindh, R. Extended Dynamically Weighted CASPT2: The Best of Two Worlds. *J. Chem. Theory Comput.* **16**, 1555–1567 (2020).
32. Fdez. Galván, I., et al. OpenMolcas: From Source Code to Insight. *J. Chem. Theory Comput.* **15**, 5925–5964 (2019).
33. Li Manni, G., et al. The OpenMolcas *Web*: A Community-Driven Approach to Advancing Computational Chemistry. *J. Chem. Theory Comput.* acs.jctc.3c00182 (2023) doi:10.1021/acs.jctc.3c00182.
34. Aquilante, F., et al. Modern quantum chemistry with [Open]Molcas. *J. Chem. Phys.* **152**, 214117 (2020).
35. Anglada, J. M. & Bofill, J. M. A reduced-restricted-quasi-Newton–Raphson method for locating and optimizing energy crossing points between two potential energy surfaces. *Journal of Computational Chemistry* **18**, 992–1003 (1997).
36. De Vico, L., Olivucci, M. & Lindh, R. New General Tools for Constrained Geometry Optimizations. *J. Chem. Theory Comput.* **1**, 1029–1037 (2005).
37. Fdez. Galván, I., Delcey, M. G., Pedersen, T. B., Aquilante, F. & Lindh, R. Analytical State-Average Complete-Active-Space Self-Consistent Field Nonadiabatic Coupling Vectors: Implementation with Density-Fitted Two-Electron Integrals and Application to Conical Intersections. *J. Chem. Theory Comput.* **12**, 3636–3653 (2016).

38. Nishimoto, Y., Battaglia, S. & Lindh, R. Analytic First-Order Derivatives of (X)MS, XDW, and RMS Variants of the CASPT2 and RASPT2 Methods. *J. Chem. Theory Comput.* **18**, 4269–4281 (2022).
39. Battaglia, S. & Lindh, R. On the role of symmetry in XDW-CASPT2. *J. Chem. Phys.* **154**, 034102 (2021).
40. Tange, O. GNU Parallel 20230422 ('Grand Jury') released. Zenodo https://doi.org/10.5281/zenodo.7855617 (2023).
41. Gozem, S. & Krylov, A. I. The *EZSPECTRA* suite: An easy-to-use toolkit for spectroscopy modeling. *WIREs Comput Mol Sci* **12**, 1–22 (2022).
42. Lee, S. Y., Brown, R. C. & Heller, E. J. Multidimensional reflection approximation: application to the photodissociation of polyatomics. *J. Phys. Chem.* **87**, 2045–2053 (1983).
43. Knizia, G. & Klein, J. E. M. N. Electron Flow in Reaction Mechanisms-Revealed from First Principles. *Angew. Chem. Int. Ed.* **54**, 5518–5522 (2015).
44. Tao, Y. PyVibMS: a PyMOL plugin for visualizing vibrations in molecules and solids. *J Mol Model* **26**, 290 (2020).
45. The PyMOL Molecular Graphics System, Version 2.5.0 Schrödinger, LLC.
46. Uthman, A. P., et al. Photoabsorption spectra of gaseous methyl bromide, ethylene dibromide, nitrosyl bromide, thionyl chloride, and sulfuryl chloride. *J. Phys. Chem.* **82**, 2252–2257 (1978).
47. Bomble, Y. J., et al. High-accuracy extrapolated *ab initio* thermochemistry. II. Minor improvements to the protocol and a vital simplification. *The Journal of Chemical Physics* **125**, 064108 (2006).

48. Tajti, A., et al. HEAT: High accuracy extrapolated *ab initio* thermochemistry. *The Journal of Chemical Physics* **121**, 11599–11613 (2004).
49. Harding, M. E., et al. High-accuracy extrapolated *ab initio* thermochemistry. III. Additional improvements and overview. *The Journal of Chemical Physics* **128**, 114111 (2008).
50. Thorpe, J. H., et al. High-accuracy extrapolated *ab initio* thermochemistry. IV. A modified recipe for computational efficiency. *J. Chem. Phys.* **150**, 224102 (2019).
51. Ichino, T., Gauss, J. & Stanton, J. F. Quasidiabatic states described by coupled-cluster theory. *The Journal of Chemical Physics* **130**, 174105 (2009).
52. Norwood, K. & Ng, C. Y. Photoion-photoelectron coincidence spectroscopy of the transient molecules SO and S2O. *Chemical Physics Letters* **156**, 145–150 (1989).
53. Radziemski, L. J. & Kaufman, V. Wavelengths, Energy Levels, and Analysis of Neutral Atomic Chlorine (Cl i). *J. Opt. Soc. Am.* **59**, 424 (1969).
54. Powell, F. X. & Lide, D. R. Microwave Spectrum of the SO Radical. *The Journal of Chemical Physics* **41**, 1413–1419 (1964).
55. Politzer, P., Murray, J. S., Grice, M. E., Brinck, T. & Ranganathan, S. Radial behavior of the average local ionization energies of atoms. *The Journal of Chemical Physics* **95**, 6699–6704 (1991).
56. Sarka, K. & Nanbu, S. Total Absorption Cross Section for UV Excitation of Sulfur Monoxide. *J. Phys. Chem. A* **123**, 3697–3702 (2019).
57. Schurath, U., Weber, M. & Becker, K. H. Electronic spectrum and structure of the HSO radical. *The Journal of Chemical Physics* **67**, 110–119 (1977).

58. Darmanyan, A. P., Gregory, D. D., Guo, Y. & Jenks, W. S. Generation and Decay of Aryl Sulfinyl and Sulfenyl Radicals: A Transient Absorption and Computational Study. *J. Phys. Chem. A* **101**, 6855–6863 (1997).
59. Weisman, J. L. & Head-Gordon, M. Origin of Substituent Effects in the Absorption Spectra of Peroxy Radicals: Time Dependent Density Functional Theory Calculations. *J. Am. Chem. Soc.* **123**, 11686–11694 (2001).
60. Yoshikawa, T., Watanabe, A., Sumiyoshi, Y. & Endo, Y. Laser spectroscopy of the 2A'−2A" system for the HSO radical. *Journal of Molecular Spectroscopy* **254**, 119–125 (2009).

Chapter 4—The Catalytic Role of Chlorine Atoms in CO + O_2 Reaction below Room Temperatures

4.1—Abstract

Carbonyl chloride radicals (ClCO) were generated from photolysis of oxalyl chloride, $(ClCO)_2$, in the presence of CO. The UV-Vis spectrum of ClCO radicals exhibits a peak near 350 nm and an averaged spacing of vibronic progressions of 409 cm^{-1}. This band was attributed to the $1^2A'' \leftarrow X^2A'$ transition via *ab initio* calculations at EOMEE-CCSD/ano-pVQZ level. The electronic structure of ClCO can be summarized by a simple molecular orbital diagram, showing donation of an unpaired electron from the Cl atom to the π^* orbital of CO. For the ClCO + O_2 reaction rate coefficients, a positive pressure dependency (20−100 Torr) and a negative temperature dependency (236−255 K) was observed: $k_{ClCO+O2}(0) = (9.0 \pm 2.3) \times 10^{-32}$ cm^6 s^{-1} at 236 K and an Arrhenius activation energy $E_a = -(2.5 \pm 1.0)$ kcal mol^{-1}. Additionally, chamber studies confirmed the increasing catalytic efficiency of Cl atom with lower temperatures.

4.2—Introduction

Chorine (Cl) chemistry plays an important role across a wide range of industrial applications, from water treatment[1] and drug discovery[2] to the development of photovoltaic materials[3,4] organic synthesis,[5] and air pollution control. [6] This is largely due to the unique properties of the chlorine atom, such as its strong tendency to fulfill the octet rule, its moderate electron energy level, and its relatively large atomic radius. These characteristics facilitate the formation of Cl-containing intermediates, which undergo diverse and intriguing reactions. One well-known example is the role of Cl atoms in the catalytic degradation of ozone in Earth's stratosphere, described in work that led to the awarding of the 1995 Nobel Prize.[7]

Beyond Earth, chlorine chemistry could play an important role in Venus' mesosphere.[8] Current photochemical models are unable to explain the surprisingly high CO_2 and low O_2 levels observed by the Venera probes in the 1960s.[9,10] However, this contrasts with the observed night glow of excited oxygen, suggesting O_2 formation from CO_2 photo-dissociation and subsequent oxygen atom recombination.[11] Chlorine atoms have been proposed to catalyze the transformation of CO into CO_2,[12] consuming O_2 at rates required to explain observations due to the significant barrier drop as shown in Figure 1.

The Cl atoms act as a catalyst for the oxidation of CO via formation of carbonyl chloride radicals (ClCO) and peroxychloroformyl radicals ($ClC(O)O_2$).[12] Under the mean conditions of Venus' mesosphere ([Cl] = 1×10^{10} cm^{-3} and 222 K)[8], we estimated an effective free energy barrier of 9 kcal mol^{-1} for ClCO formation considering the entropy cost to combine Cl atom and CO.[13] Due to the lack of water vapor, and consequently the low [OH], the oxidation of CO is expected to be dominated by the Cl catalytic reactions but not the OH + CO reaction (See SI for details). More importantly, the significant barrier drops suggests that the efficiency of CO oxidation by Cl atoms will increase with decreasing temperature, contrasting to common understanding of an oxidation reaction.

To accurately model the oxidation efficiency of CO due to Cl atoms, the equilibrium constant for the ClCO formation (K_{ClCO}) and the ClCO + O_2 reaction rate coefficients ($k_{ClCO+O2}$) are critical parameters. Unfortunately, estimates of both parameters are currently poorly constrained. Nicovich et al.[14] measured the ClCO equilibrium constant by monitoring the disappearance of Cl atoms at various CO concentrations. However, significant uncertainties exist for K_{ClCO} (a factor of ± 3 at the 95% confidence level), which leads to a wide range of predicted oxygen levels (10^9–10^{13} cm^{-3}) in current simulations of the Venus atmosphere.[15] Furthermore, the rate coefficient for the ClCO + O_2 reaction has only been indirectly investigated from the rate of CO depletion, yielding a reaction rate coefficient of $k_{\mathrm{ClCO+O2}}$(1 atm, 298 K) = $(4.3 \pm 3.2)\times10^{-13}$ cm^3 s^{-1}.[16] In addition to the notable experimental uncertainty in the reported rate coefficient, the experiments were conducted at conditions vastly different from those of the Venusian mesosphere.

Understanding of the electronic structure and reactivity of the ClCO radicals helps us to evaluate their kinetics and dynamics. Existing spectroscopic measurements of ClCO radicals have focused mainly on the ground state, including the electron spin resonance (EPR) spectroscopy[17], and mid-infrared (IR) measurements in an Ar-matrix[18] and in gas phase near 1885 cm^{-1}. [19]

In this work, we measured the UV-Vis absorption spectrum of gas phase ClCO radicals using a multipass UV-Vis spectrometer coupled with a pulsed-laser photolysis flow reactor.[20] High-level *ab initio* calculations were performed to elucidate the bonding structure and simulate the recorded spectrum. Additionally, we investigated the kinetics of the ClCO + O_2 reaction by monitoring the ClCO absorption signals at conditions relevant to Venus' atmosphere. Finally, chamber experiments, using a large White-cell-FTIR setup have been performed to verify the predicted temperature dependence of the catalytic efficiency of Cl atom.

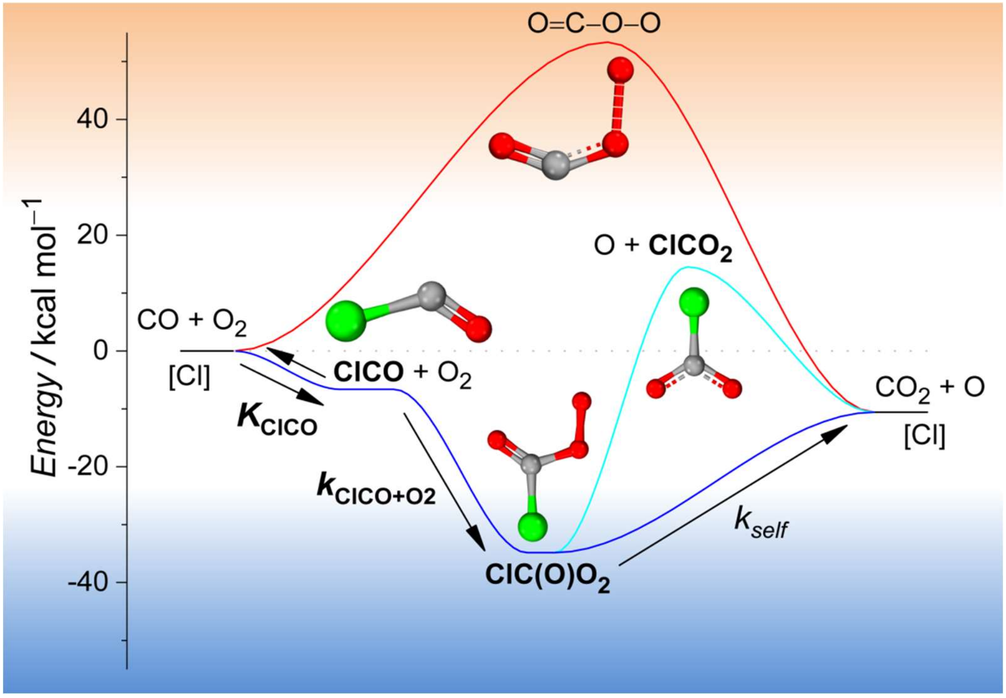

Figure 4.1. Potential energy diagram of the CO oxidation in the presence (blue) and absence (red) of Cl atoms.

All the structures were optimized at CCSD/ano-pVQZ level and the energies were refined at CCSD(T)/ano-pVQZ level. Representative geometries of the Cl-containing intermediates as well as the transition state are shown.

4.3—Results and Discussions

4.3.1—The UV-Vis Absorption Spectrum of ClCO Radicals

For this part of the study, oxalyl chloride, $(ClCO)_2$, was photolyzed at 193 nm producing two Cl atoms and two CO molecules with yield of unity,[21] thus creating a simple chemical system at 236 K and total pressure of 50 Torr. We estimate an equilibrium lifetime of approximately 60 μs at 50 Torr of CO based on the reported forward and backward rate coefficients of ClCO formation (3.2×10^{-33} cm^6 s^{-1} and 1.5×10^{-15} cm^3 s^{-1}, respectively). As a result, we anticipated a prompt formation of ClCO absorption signal, peaking near 100 μs.

The available energy after $(ClCO)_2$ decomposition (~247 kJ mol^{-1}) distributes 13% in the Cl atoms and 87% in the CO molecules,[22] leading to highly excited CO molecules. These hot CO molecules are stabilized either via collision with the buffer gas (in this case CO) or via emission to form the ground-state CO.[23] To achieve a good ClCO absorption, high concentrations of $(ClCO)_2$ were used (9.9×10^{15} cm^{-3}), leading to strong absorption of the 193 nm photolysis photons and inhomogeneous radical formation along the flow reactor ($\sigma_{(ClCO)2}$(193 nm)[24] = 3.8×10^{-18} cm^2, $L = 45$ cm, $T = 18\%$).

The spectra of the $(ClCO)_2$ photolysis system in pure N_2 and CO at 50 Torr and 236 K are displayed in Figure 2A. The negative absorption below 360 nm was attributed to the $(ClCO)_2$ photo-depletion, $\Delta(ClCO)_2$, which assisted in estimating the [Cl]. The introduction of CO made new spectral features, forming two series of vibrational progressions within the 360–475 nm range. As discussed below we assign these features to the formation of ClCO. The rate of formation based on the absorption signal monitored near 390 nm (Figure 2B) increased as the CO concentration increased, leading to a shorter equilibrium lifetime than the previously reported values (Figure S2). Additionally, stronger signals were observed at lower temperatures as shown in Figure 2C. Assuming a rapid equilibrium at 50 Torr CO, this temperature dependence suggests an enthalpy change for the ClCO equilibrium of −(5.50 ± 0.75) kcal mol^{-1}, consistent with previous measurements within the large uncertainty.[14]

The observed product spectrum was obtained by subtracting the absorption spectra recorded with CO from that with N_2 (Figure 2D). The resulting spectrum displays a clear vibrational progression, with the overall shape closely matching the simulated spectrum of ClCO. At wavelengths > 340 nm, similar vibronic progressions were observed using both $(ClCO)_2$ and thionyl chloride (Cl_2SO) as Cl atom precursors at 248 nm (Figure 2E). Interference of an unknown absorber was observed in the Cl_2SO photolysis case, which we ascribe to observed differences in the collected spectra (Figure S3). These two series of vibronic progressions have average spacing of 409 and 408 cm^{-1} (Figure 2F) for the strong and weak intensity series, respectively. A consistent difference of 215 cm^{-1} between these two series in our detection window suggests another vibrational mode with frequency of 624 cm^{-1}.

Based on variation of experimental conditions as described above and theoretical simulations, we assigned the obtained spectrum to the ClCO radical. Below 330 nm, significant deviations on the recorded spectra (Figure 2A) were observed from the estimated $\Delta(ClCO)_2$. Although the origin of this deviation is not clear, we have confidence to assign this new feature to ClCO radicals above 330 nm.

Using the reported equilibrium constant,[14] we estimated the absorption cross-section of the ClCO radical near 350 nm to be in the range of $(1–16) \times 10^{-20}$ cm^2, which is smaller than the peak absorption cross-section of 2.5×10^{-19} cm^2 at 345 nm in our simulated spectrum. However, using our smaller equilibrium constant inferred from the observed CO dependence and temperature effects, a cross-section in the order of 10^{-19} cm^2 is our best estimate.

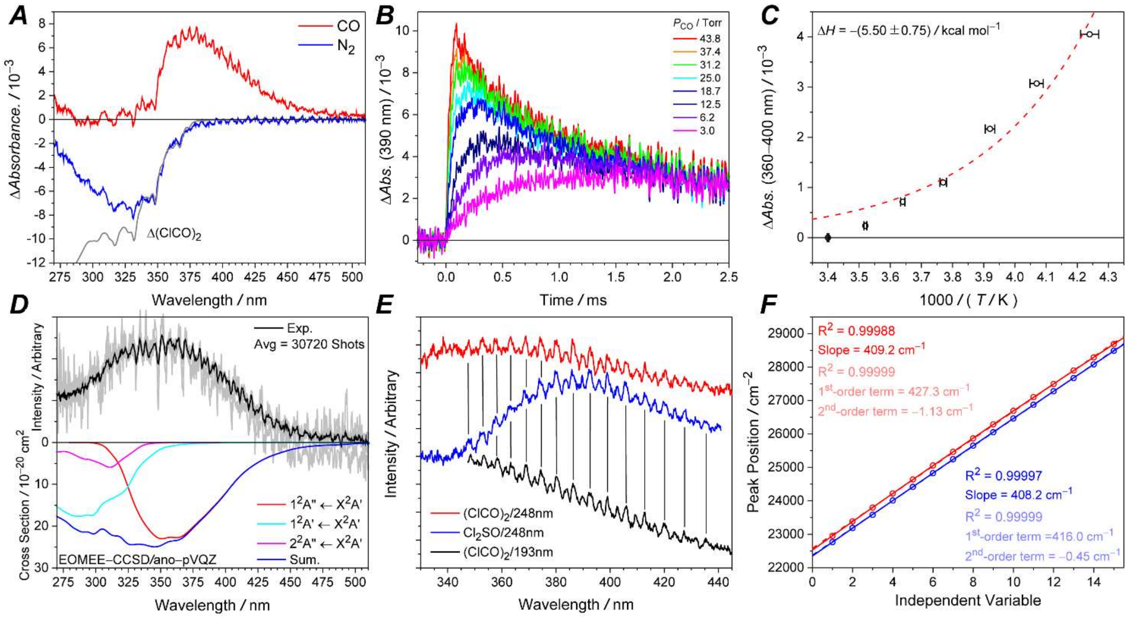

Figure 4.2. The recorded spectrum of ClCO from the 193 nm photolysis of $(ClCO)_2/N_2/CO$ mixture.

(**A**) Representative spectra of pure CO or N_2 as the buffer gas at delay time = 0.072 ms, 50 Torr and 236 K for averaging of 12,266 laser shots.
(**B**) Representative time trace for various CO concentrations balanced by N_2 to 50 Torr and 236 K.
(**C**) The recorded absorption intensities as function of temperatures for pure CO at 50 Torr. The red line shows the exponential fit assuming that the Cl atoms have reached the equilibrium at delay time = 0.1 ms.
(**D**) The experimental (black) and simulated (blue) spectrum of ClCO radicals. Contributions from distinct excited states (red, cyan and magenta) are also shown. The simulated spectrum was constructed using the nuclear ensemble approach by sampling the ground-state geometry based on a Wigner distribution with 5000 structures and calculating the vertical excitation energies and oscillator strength for each geometric structure at the EOMEE-CCSD/ano-pVQZ level of theory.
(**E**) Spectra recorded using a 300 grooves/mm grating for different chlorine atom precursors and different photolysis wavelengths shows the same vibrational progression near 380 nm.
(**F**) Linear and quadratic fits to the observed positions of the vibrational progressions. Red circles represent the strong series indicated in panel E.

4.3.2—The Electronic Structure of ClCO Radical

Table 1 summarizes the results of the ClCO calculations. The ground state geometry optimization yielded a structure with a C–O bond length of 1.15 Å, a Cl–C bond length of 1.80 Å, and a bending angle of 129.1 degrees, in agreement with previous calculations.[25,26] The harmonic vibrational frequencies were 367 cm^{-1}, 606 cm^{-1}, and 1963 cm^{-1} for the bending, ClC stretching, and CO stretching modes, respectively. These values align with previous IR measurements.[18] Additionally, the singularly occupied molecular orbital (SOMO) displayed similar contributions from both the chlorine 3*p* orbitals and the in-plane π* orbital of CO, as suggested by EPR measurements.[17] Four low-lying excited states were identified with orbital transition shown in Table S1 and S2.

Table 4.1. Summary of Calculations of Geometries, Harmonic Frequencies, Vertical Transition Energies, Adiabatic Transition Energies, and the 0-0 Transition Energies of ClCO.

Geometry Optimized		X^{2}A'		1^{2}Π	
Geometry[a]	r(C–O) / Å	1.153		1.192	
	r(Cl–C) / Å	1.796		1.611	
	∠(ClCO) / degree	129.07		180	
Frequency[a] / cm^{-1}	ClCO bending	367.1		411.4 (1514.3***i***)[a]	
	ClC stretching	605.7		733.7	
	CO stretching	1962.5		2013.6	
Vertical Transition Energies[b] / eV		1^{2}A'	4.34 (1.62×10^{-3})[c]	1^{2}Π	0.0
		2^{2}A'	5.91 (4.43×10^{-2})	1^{2}Σ	1.05
		1^{2}A"	3.45 (1.67×10^{-3})		
		2^{2}A"	4.55 (2.21×10^{-4})	2^{2}Π	6.91
Adiabatic Transition Energies / cm^{-1}		0		15820 (15948)[d]	
0–0 transition energy/cm^{-1} [nm]		–		16266 [614.8]	

[a] Imaginary frequency along the bending potential to the X^{2}A' state.

[b] Excited state properties calculated at EOMEE-CCSD/ano-pVQZ level.

[c] Oscillator strength indicated in parentheses.

[d] Calculated at CCSDT/ano-pVQZ level.

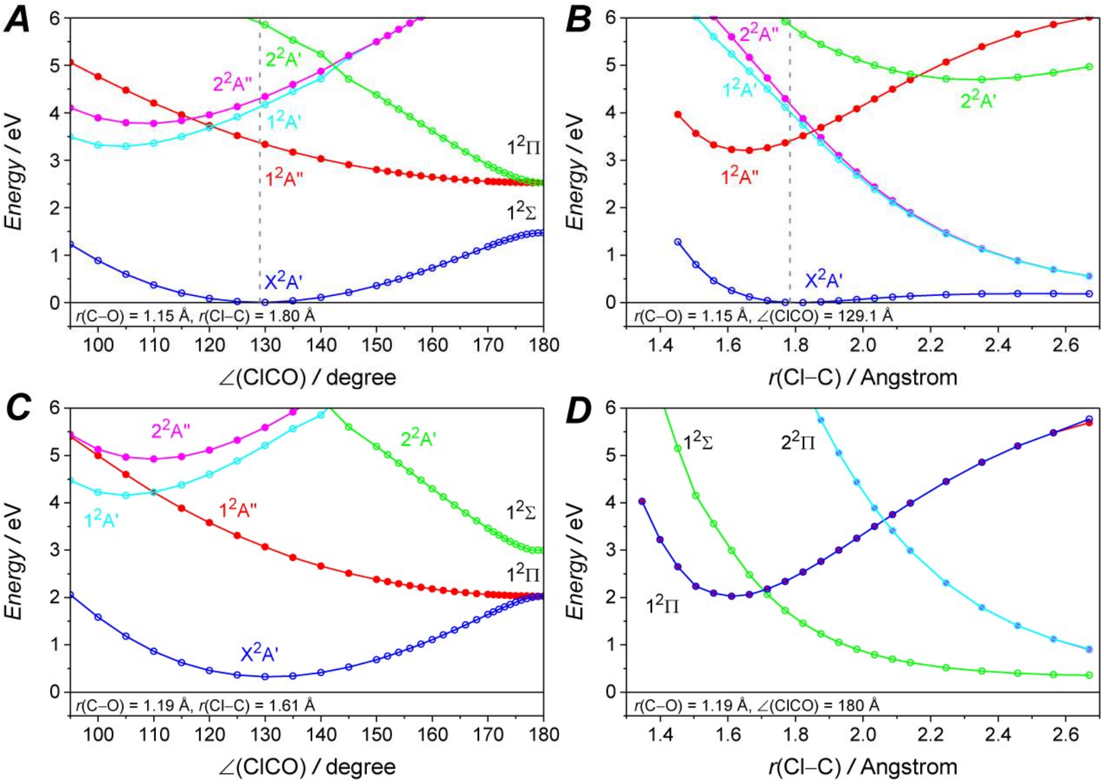

Figure 4.3 Potential energy surface of the ClCO radicals.

Panel A/C and panel B/D shows the potential energy curve along the bending angle and Cl–C bond length with the other degrees of freedom were fixed at the X^2A' geometry and the $1^2\Pi$ geometry for panel A/B and panel C/D, respectively.

We generated four representative slices of the potential energy surface of ClCO radicals along either the bending (∠ClCO) or the Cl–C (*r*(Cl–C)) coordinates, utilizing MR-EOM-CC calculations with an “11 electron in 8 orbital CASSCF” reference. First, all four excited states lie well above the dissociation energy D_0(Cl–CO) = 2226 cm^{-1} as calculated by the HEAT-345(Q) method (Table S3). Second, we note that only the $1^2A''$ state is bonded along *r*(Cl–C) (Figure 3B) and becomes degenerate with the $2^2A'$ state, (Figure 3A), indicating that the $1^2A''$ state has the lowest minimum energy at linear geometry. Third, the energy orders of $1^2\Pi$ state and $1^2\Sigma$ state depends on the *r*(Cl–C) at linear geometry (Figure 3D), indicating the existence of a conical intersection due to the complex interaction among X^2A', $1^2A''$ and $2^2A'$ states (See "Analysis of the ClCO Electronic Structure" in SI for details).[27]

The electronic structure of the ClCO radical can be described using simple molecular orbital (MO) diagram as shown in Figure 4. The diagram suggests that the SOMO correlates with the 2π orbital of CO, as the $1^2\Pi$ state is the ground state when *r*(Cl–C) < 1.7 Å. The occupation of π* orbitals weaken the CO triple bond, thereby increasing the reactivity of CO as the carbon atom becomes the reactive center (Figure S5). The MO diagram supports the expectation that the Cl atom can significantly enhance the reaction of O_2 with the CO moiety. In addition, these findings imply that the catalytic effect is more pronounced at lower temperatures.

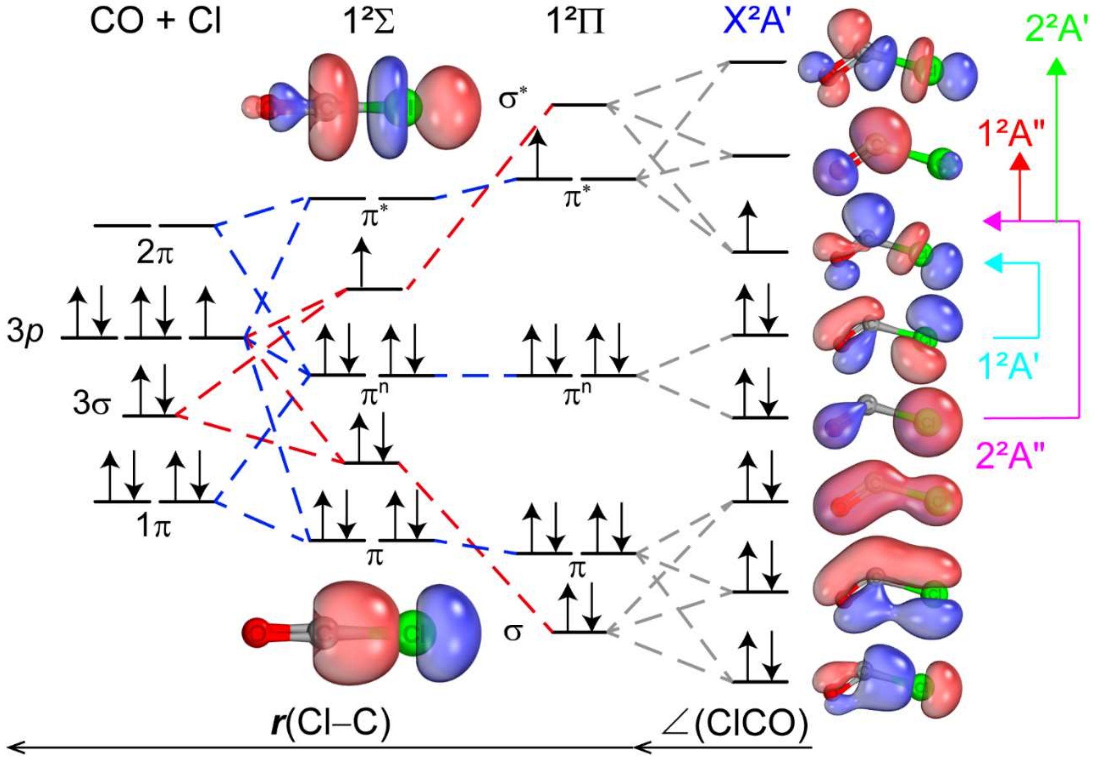

Figure 4.4. Molecular orbital correlation diagram showing the valence electronic structure of ClCO radical.

The *p* orbital of chlorine atom (3*p*) and five MO of CO molecule (1π, 3σ and 2π) are considered. The red dashed and blue dashed lines connect orbitals with σ and π bonding character along the Cl–C bond at linear structure. The gray dashed lines connect orbitals between linear and bend structure. The vertical and horizontal arrows indicate the alpha and beta electron transitions from the X^{2}A' ground state.

4.3.3—Kinetics of the ClCO + O_2 Reaction

The ClCO + O_2 reaction rate coefficient, $k_{ClCO+O2}$, was investigated by monitoring the absorption signals of ClCO radicals near 380 nm. This wavelength was chosen to avoid interference from $(ClCO)_2$ depletion. We employed a photolysis wavelength of 248 nm to prevent the photodissociation of O_2. After introduction of $(ClCO)_2$, the photolysis laser intensity was attenuated by roughly 10%, indicating approximately homogeneous radical generation along the reactor due to the smaller absorption cross-section of cross-section of $(ClCO)_2$ at 248 nm ($\sigma_{(ClCO)2}$(248 nm) = 3.1×10^{-19} cm^2)[28].

In representative spectra of the $(ClCO)_2/CO/N_2$ mixture, we observed significant formation of Cl_2 at a delay time of 3 ms, resulting in a small shift in absorption baseline ($<5 \times 10^{-4}$ absorbance units) on the time traces. Introducing oxygen led to notable deviations in the spectra below 300 nm at a delay time of 3 ms as shown in Figure 5A. As anticipated, we observed that the ClCO absorption signals decreased with increasing temperature while no new features were recorded on the observed spectra.

Figure 5B displays typical time traces of ClCO at various O_2 concentrations. We fitted a single exponential decay function to the time trace to determine the observed decay rate coefficient (k_{obs}). The decay rate coefficients without O_2 (k_0) represent the base decay, accounting for the loss rates of both ClCO and Cl, under the assumption of rapid equilibrium in our experimental conditions. The fitting ranges from 0.15 ms to five lifetimes and was iteratively conducted until the changes in k_{obs} were less than 1%.

As depicted in Figure 5C, the decay rate increased with higher O_2 concentrations. The data obtained under pseudo-first-order conditions were fitted linearly to give the ClCO + O_2 reaction rate coefficients ($k_{ClCO+O2}$). The $k_{ClCO+O2}$ increased linearly with total pressure, suggesting that the ClCO + O_2 reaction was still in the fall-off region below 100 Torr (Figure 5D). Linear least-squares fits yield the termolecular reaction rate coefficients at the low-pressure limit, $k_{ClCO+O2}(0)$ of $(9.0 \pm 2.3) \times 10^{-32}$, $(6.4 \pm 2.8) \times10^{-32}$, and $(6.0 \pm 3.1) \times 10^{-32}$ cm^6 s^{-1} at 236, 246, and 255 K, respectively. The measured low-pressure rate coefficients are 25 times faster than the Cl + O_2 reaction ($k_{Cl+O2}(0) = 3.6\times10^{-33}$ cm^6 s^{-1} at

236 K), indicating that the decay of ClCO absorption signal was not due to the disappearance of Cl atoms.

Our data shows a weak temperature dependence of $k_{\mathrm{ClCO+O2}}(0)$ with an Arrhenius activation energy of $-(2.5 \pm 1.0)$ kcal mol^{-1}, as shown in Figure 5E. The positive pressure dependence and negative temperature dependence suggested a barrierless reaction (Figure S5) and the formation of $ClC(O)O_2$ radicals as the primary product. Considering the pressure dependence of similar reactions ($R + O_2 \rightarrow RO_2$, R = CH_3,[29] CCl_3,[30] and $H_3CC(O)$[31]), the ClCO + O_2 reaction might be in the fall-off region at conditions (< 240 Torr) of Venus' mesosphere.

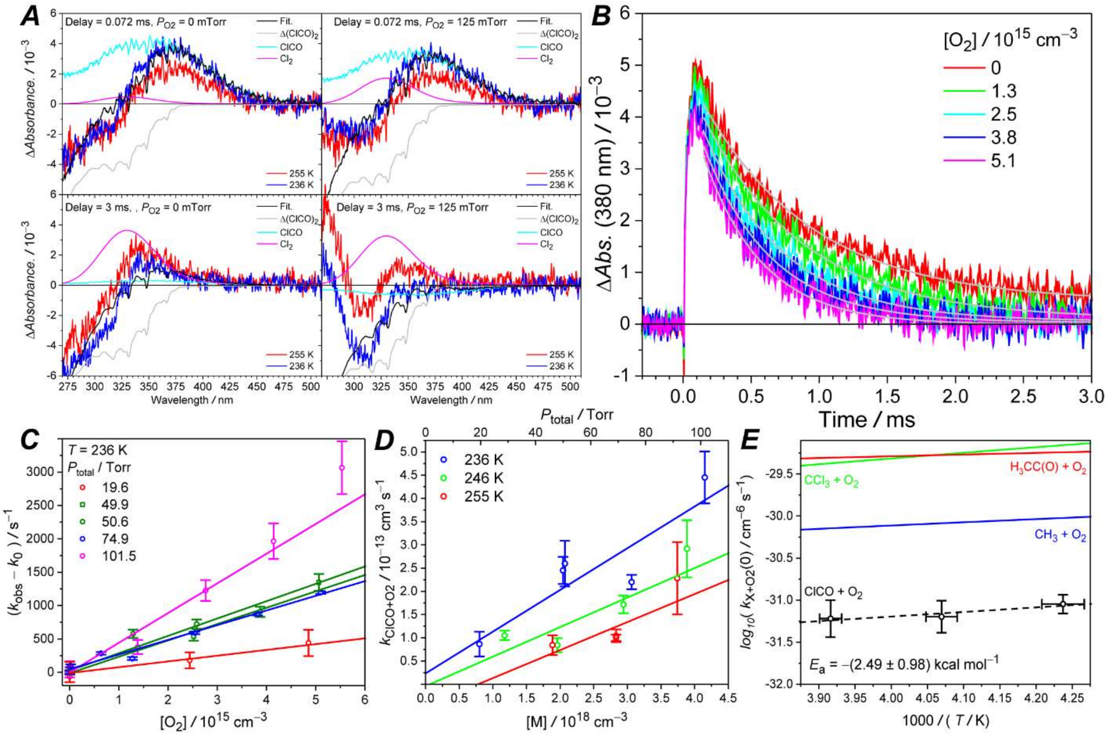

Figure 4.5. Representative data for the kinetic analysis of the ClCO + O_2 reaction.

(**A**) Representative spectra of $(ClCO)_2/CO/N_2/O_2$/248 nm mixtures at various delay times, O_2 concentrations and temperatures at $[(ClCO)_2] = 8.6\times10^{15}$ cm^{-3}, P_{CO} = 31.0 Torr, and P_{total} = 74.9 Torr. The spectra at 236 K (blue) were fitted to the contributions of ClCO (cyan), Cl_2 (magenta) and $\Delta(ClCO)_2$ (gray). The black lines show the fitted results.

(**B**) Representative time trace at various O_2 concentrations balanced by N_2 to 75 Torr and 236 K. Gray lines show the single exponential decay fit to the time traces.

(**C**) Plot of the change of observed decay rate coefficient ($k_{obs} - k_0$) as a function of $[O_2]$ at distinct total pressure and 236 K. Solid lines are linear fit which yields the ClCO + O_2 reaction rate coefficients, $k_{ClCO+O2}$.

(**D**) Plot of $k_{ClCO+O2}$ as a function of total pressure. Solid lines show the linear fit and the slopes are the low-pressure limit for the ClCO + O_2 reaction rate coefficients $k_{ClCO+O2}(0)$.

(**E**) Arrhenius plot of low-pressure limit reaction rate coefficients for the CCl_3, $H_3CC(O)$, CH_3 and ClCO with O_2. Dashed line is linear fit to the measured $k_{ClCO+O2}(0)$. All error bars (±1σ) in Figure 5 only presents the uncertainty from the statistic fit.

4.3.4—Chamber Experiments

The ClCO radical kinetics measurements and the *ab initio* calculations described above suggest a stronger catalytic effect below room temperature. To compliment the fundamental studies outlined above, we designed relative rate chamber experiments to examine the catalysis efficiency as a function of temperature. These experiments were carried out using 340 nm UV-photolysis of molecular chlorine as the Cl atom source. The kinetics of reaction of Cl atoms with CO was measured relative to that of difluoromethane (CH_2F_2).

$$Cl + CH_2F_2 \rightarrow \text{Product(s)} \qquad , k_{CH2F2+Cl}$$

$$Cl + CO \rightarrow \text{Product(s)} \qquad , k_{CO+Cl(observed)}$$

We note that CO is not a product of Cl oxidation of CH_2F_2, thus avoiding any potential interference in our CO depletion measurements. Figure 6A shows typical data obtained from the experiments. Depletion of CO and CH_2F_2, as well as the formation of CO_2, was monitored by observing their respective strong absorption bands in 2036–2236 cm^{-1} (CO), 1088 cm^{-1} (CH_2F_2), and 666 cm^{-1} for CO_2. The broad absorption band observed close to 2000 cm^{-1} is due to COF_2, the sole oxidation product of the reaction of Cl atoms with CH_2F_2.

Assuming that the observed consumptions of CO and CH_2F_2 are solely due to reactions initiated by the chlorine atoms, it can be shown that for a particular temperature:

$$Ln\left(\frac{[CO]_{t_0}}{[CO]_t}\right) = \frac{k_{CO+Cl\,(observed)}}{k_{CH_2F_2+Cl}} \times Ln\left(\frac{[CH_2F_2]_{t_0}}{[CH_2F_2]_t}\right) \qquad (I)$$

where $[CO]_{t0}$, $[CO]_t$, $[CH_2F_2]_{t0}$ and $[CH_2F_2]_t$ are the concentrations of CO and the CH_2F_2 at times zero and t. Equation (I) describes a straight line with a slope equal to the ratio of the rate constants for the reaction of CO with Cl atoms and that of CH_2F_2. The observed CO depletion rate constant, $k_{CO+Cl\,(observed)}$, can thus be obtained from the relative rate constant ratio using the known Cl + CH_2F_2 reaction rate coefficient, $k_{CH2F2+Cl} = 7.6\times10^{-12}$ exp(-1630/T).[29] The excellent linearity for the data shown in figures 6B and 6C supports the effectiveness of our simple model in describing the chamber system.

With repeated UV exposures of the mixtures, we observed a linear increase in CO_2 signal as expected. The linear least-squares fit to the data shown in Figure 6D gives a (98 ± 3) % molar yield of CO_2 from CO, suggesting that the sole end-product of the reaction of Cl + CO is CO_2. To extract relevant reaction rate coefficients from the relative rate experiments, we employed the following model.

$$Cl + CO \rightarrow ClCO \qquad ,k_+$$

$$ClCO \rightarrow Cl + CO \qquad ,k_-$$

$$ClCO + O_2 \rightarrow \text{Product(s)} \qquad ,k_{O2}$$

where k_+ and k_- denote the forward and backward reaction rate coefficients of Cl + CO reaction at 700 Torr of N_2; k_{O2} denotes the reaction rate of ClCO + O_2 reaction at 700 Torr of N_2. Furthermore, applying the steady-state approximation to [ClCO] (See SI for details), we can deduce formula (II).

$$\frac{1}{k_{CO+Cl\,(observed)}} = \frac{k_-}{k_+ k_{O2}} \frac{1}{[O_2]} + \frac{1}{k_+} = \frac{1}{K_{ClCO} k_{O2}} \frac{1}{[O_2]} + \frac{1}{k_+} \qquad \text{(II)}$$

By plotting the reciprocal of $k_{CO+Cl(observed)}$ as a function of the reciprocal of $[O_2]$, we can obtain an effective termolecular rate coefficient ($k_{eff} = K_{ClCO} k_{O2}$), which may serve as a measure of the Cl catalytic efficiency.

Figure 6D shows the O_2 dependence plot for the observed CO rate constant, $k_{CO+Cl(observed)}$. Notably, the linear slope for the lower temperature data is smaller than for the higher temperature data, suggesting a higher catalysis effect at colder conditions. The effective termolecular rate coefficients, k_{eff}, can be determined from the inverse of the slope as $(5.04 \pm 0.07)\times10^{-32}$ cm^6 s^{-1} and $(6.92 \pm 0.53)\times10^{-32}$ cm^6 s^{-1}, at (292.7±0.2) and (278.4±0.2) K, respectively. This finding provides direct evidence that the Cl catalysis effect is stronger at lower temperatures.

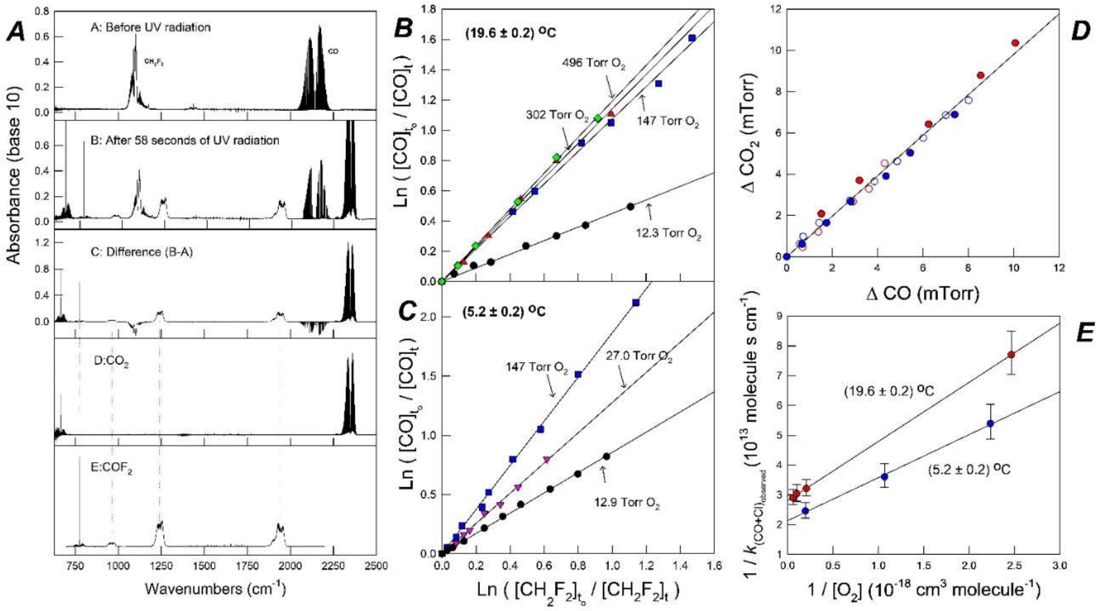

Figure 4.6. Representative data for the chamber experiments on the catalysis role of Cl atom in the CO oxidation. Made by Dr. Mads P. Sulbaek Andersen.

(A) IR spectra obtained before (Panel A) and after (Panel B) 58 seconds of UV-B irradiation of 4.96 × 10^{14} cm^{-3} CO, 2.61 × 10^{14} cm^{-3} CH_2F_2 and 4.54 × 10^{15} cm^{-3} Cl_2 in 12.9 Torr of O_2 in 700 Torr total pressure of N_2. The consumption of CO was 32%. Panel C shows the difference spectrum. Panel D and E are reference spectra for COF_2 and CO_2, respectively.

(B) Decay of CO versus CF_2H_2 at (292.7±0.2) K in the presence of Cl atoms and 12.3 Torr (circles), 147 Torr (squares), 302 Torr (triangles) and 496 Torr (diamonds) Torr of O_2 in 700 Torr total pressure of N_2.

(C) Decay of CO versus CF_2H_2 at (278.4±0.2) K in the presence of Cl atoms and 12.9 Torr (circles), 27.0 Torr (triangles), and 140 (squares) Torr of O_2 in 700 Torr total pressure of N_2.

(D) Yield of CO_2 as a function of consumption of CO obtained at (292.7±0.2) K (red symbols) and (278.4±0.2) K (blue symbols) at high (140 496 Torr, solid symbols) and low (12.3 - 12.9 Torr, open symbols) concentrations of O_2.

(E) O_2 dependence plot for the reaction of Cl + CO for the data obtained at (292.7±0.*2*) and (278.4±0.*2*) K. The error bars represent the propagated errors for the CH_2F_2 reference rate constant (2 sigma) and the statistical error (2 sigma) from the measured relative rate constant ratios.

4.4—Conclusions

In this study, we reported the UV absorption spectrum of the ClCO radical using a multipass broadband UV-Vis transient-absorption spectrometer coupled with a temperature-controlled flow reactor. The ClCO radical exhibited two bands of vibronic progressions near 380 nm, comprising a strong and a weak intensity series with an average spacing of 409 cm^{-1} and a shift of 215 cm^{-1}. The observed spectrum has a peak near 350 nm, with a cross-section on the order of 10^{-19} cm^2.

High-level *ab initio* calculations for ClCO were performed, and four low-lying excited states were identified. The potential energy surface was explored using the MR-EOM-CC method on a CASSCF(11, 8)-5SA reference. Our findings indicated that the 1^2A', 2^2A', and 2^2A" excited states were repulsive, unlikely to exhibit clear vibronic progression. In contrast, the 1^2A" state had a vertical transition energy of 3.45 eV, matching the observed band maximum and has a linear equilibrium geometry. Harmonic calculations yielded a bending frequency of 411 cm^{-1}, which is consistent with the observed spacing. Spectrum simulation further demonstrated that the red side of the ClCO spectrum was dominated by the $1^2\mathrm{A}'' \leftarrow \mathrm{X}^2\mathrm{A}'$ transition.

MO diagram analysis suggested that the chlorine atom donates its unpaired electron into the π* bonding of CO, weakening the CO triple bond and creating a reactive central carbon. Kinetic studies of the ClCO + O_2 reaction, conducted by monitoring the absorption signals of ClCO radicals from 248 nm $(\mathrm{ClCO})_2$ photolysis, showed that the decay rate of ClCO radicals increased at higher total pressures (20–100 Torr) and lower temperatures (236–255 K), with an Arrhenius activation energy of $E_a = -(2.5 \pm 1.0)$ kcal mol^{-1}. The low-pressure limit rate coefficient was determined as $k_{\mathrm{ClCO+O2}}(0) = (9.0 \pm 2.3) \times 10^{-32}$ $\mathrm{cm}^6\ \mathrm{s}^{-1}$ at 236 K. Furthermore, chamber studies were performed to directly estimate the Cl catalysis efficiency by monitoring CO depletion kinetics and CO_2 formation. From these studies, we derived an effective termolecular reaction rate coefficient, $k_{\mathrm{eff}} = K_{\mathrm{ClCO}}k_{\mathrm{ClCO+O2}} = (5.04 \pm 0.07) \times 10^{-32}$ and $(6.92 \pm 0.53) \times 10^{-32}$ $\mathrm{cm}^6\ \mathrm{s}^{-1}$, at (292.7 ± 0.2) and (278.4 ± 0.2) K, as a measure of the catalysis efficiency.

4.5—Methods

4.5.1—UV-Vis Absorption Measurements

The experimental setup and performance were described and evaluated previously.[20] In short, a free-space broadband light source (LDLS, Energetiq EQ-99) was collimated using a parabolic mirror (Thorlab, MPD149–F01, RFL = 101.6 mm, 90° OAP) and directed into a White cell for ten passes, which gives an effective absorption length of $L_{\mathrm{eff}} \approx$ 450 cm. After exiting the multipass system, the light was focused into a spectrograph, installed with either a 600 grooves/mm or a 300 grooves/mm grating (Princeton Instruments, SpectraPro HRS–300). A half-high mirror within the spectrograph guided the bottom portion of the light to a photomultiplier tube (Hamamatsu R928) and left the upper portion to an intensified CCD camera (Instruments PI-MAX4, 1024x256). A long-pass filter (Semrock LP02-257RU-30x40) was placed at the exit of the White cell to isolate the photolysis laser from an excimer laser, which generated either 193 nm or 248 nm by changing the rare gas (Coherent COMPex 205F, ArF or KrF).

The chlorine atom precursors, $(ClCO)_2$ (Sigma-Aldrich >99%, ampule seal) and Cl_2SO (Sigma-Aldrich > 99%), were delivered by a small stream of nitrogen flow in a bubbler, immersed into a temperature-controlled water bath (Fisherbrand, Isotemp 4100) at 292 K. The emerging flow from the bubbler was mixed with the CO (Airgas >99.99%), N_2 and O_2 (Airgas >99.999%) flows and guided into a temperature-regulated double-jacket flow reactor. The gas mixtures were pre-cooled through a Graham condenser (Chemglass, CG-1830-30) with a cone shape exit, reducing the temperature inhomogeneity (236–298K, with a margin of ± 1.6 K) compared to our previous setup. To remove potential impurities, the CO stream flowed through a potassium hydroxide (Baker Analyzed > 86.7%) trap immersed into a methanol/methanol ice mixture (near −95°C). The pressures in the flow reactor and precursor bubbler were continuously monitored using diaphragm gauges (MKS, 127AA series). Total pressure in the reactor was controlled by a throttle valve (MKS type 153). Detailed experimental conditions were listed in the supplementary material.

4.5.2—Theoretical Methods

The CFOUR program suite[32] was utilized for performing various coupled-cluster calculations, including single and double (CCSD) and higher-order (CCSD(T) and CCSDT) computations. We selected the ano-pVXZ basis sets,[33] as atomic natural orbital (ANO) basis sets have demonstrated exceptional effectiveness in calculating harmonic frequencies, especially with a frozen-core approximation. These basis sets are particularly suitable since they were not optimized for core correlation. For ground state geometries, we optimized using CCSD with unrestricted Hartree-Fock (UHF) for open-shell molecules and restricted Hartree-Fock (RHF) for closed-shell molecules. The properties of excited states were calculated using the EOMEE-CCSD method. Additionally, we optimized the transition states for the $O_2 + CO \rightarrow CO_2 + O$ and $ClC(O)O_2 \rightarrow ClO + CO_2$ reactions.

While the EOM-CCSD method accurately treats dynamic correlation in the excited state, it failed in describing the behavior of adiabatic states near the conical intersection and during the bond-breaking process. Therefore, to qualitatively depict the potential energy surface and account for the complex interactions of the ClCO radical—particularly due to the Renner-Teller effect and pseudo-Jahn-Teller effect—we employed the multireference equation of motion coupled-cluster (MR-EOM-CC) method. This approach used a complete active space self-consistent field five states averaged (CASSCF(11, 8)-5SA) reference within the ORCA program suite. Additionally, preliminary N-electron valence state perturbation theory (NEVPT2) calculations were carried out to explore the potential energy surface of the $ClO + O_2$ reaction, using a CASSCF(9,6) reference and the ano-pVTZ basis set. For the visualization of orbitals, we used the IboView package.[34]

4.5.3—Spectral Simulation

For the spectral simulation we used the ground-state geometry and normal modes calculated at the CCSD/ano-pVQZ level of theory using the CFOUR program suite. A nuclear ensemble, consisting of 5000 geometries, was created using a Wigner distribution based on normal mode displacements with the Newton-X (version 2.4 B06) program.[35,36] The large nuclear ensemble used minimizes the numerical integration error due to the statistical sampling in the final spectrum.[37] For each geometry vertical excitation energies and oscillator strengths for the ten first singlet excited states were calculated at the EOMEE-CCSD/ano-pVQZ level of theory with Gaussian 16 (Rev. C.02)[38] interfaced to Newton-X. The individual vertical transitions were convoluted with a 0.1 eV full width at half maximum normalized Gaussian function, as recommended by Farahani et al.[37]

We tested different basis sets for the EOMEE-CCSD calculations and found that in all cases the final spectra were almost identical to the one calculated at the EOMEE-CCSD/ano-pVQZ level of theory (see Figure S6). We also performed spectral simulations at three different temperatures, 0 K, 236 K, and 298 K. As can be seen in Figure S7, the differences between the spectra at the different temperatures are negligible.

4.5.4—Chamber Studies

Experiments were conducted using a 140 L quartz photoreactor, interfaced to a Mattson Sirus 100 FTIR spectrometer and surrounded by 16 UV-B (Qlab 313L narrow band UV-B) lamps, the latter used to photochemically initiate the experiments. The reactor is housed in a Cascade Thermal Solutions environmental chamber providing temperature control from 243–322 K. In-situ multi-pass optics[39] provides a total optical path length of 24.44 m. Infrared spectra were derived from 32 co-added interferograms with a spectral resolution of 0.25 cm^{-1}. A liquid nitrogen cooled midband MCT detector was used in this study. All experiments were performed in 700 Torr total pressure of N_2 diluent. Cl atoms were produced by the photolysis of molecular chlorine using the UV-B lamps (peak at 313 nm): $Cl_2 + h\nu \rightarrow 2\ Cl$.

Analysis of the IR spectra was achieved through a process of spectral stripping in which small fractions of a calibrated reference spectrum were subtracted from the sample spectrum. CO and CH_2F_2 were monitored using absorption features over the wavenumber ranges 1088 cm^{-1} (CH_2F_2), 2036–2236 cm^{-1} (CO) and 2283–2289 cm^{-1} (CO_2). Dark experiments were performed ensuring no unwanted loss of CO and CH_2F_2 occurred within the chamber. Mixtures of reactants were irradiated with UV and subsequently left in the dark for 30 min with no losses (<2%) observed. We conclude that dark reactions/ heterogeneous reactions are not a complication in the present study. The samples of CH_2F_2 and CO used in the experiments were obtained from commercial sources with purities >95%. Quoted uncertainties for the relative rate data are two standard deviations from the least-squares regressions (forced through zero).

4.6—References

1. Guo, K., Wu, Z., Chen, C. & Fang, J. UV/Chlorine Process: An Efficient Advanced Oxidation Process with Multiple Radicals and Functions in Water Treatment. *Acc. Chem. Res.* **55**, 286–297 (2022).
2. Chiodi, D. & Ishihara, Y. "Magic Chloro": Profound Effects of the Chlorine Atom in Drug Discovery. *J. Med. Chem.* **66**, 5305–5331 (2023).
3. Yao, H., Wang, J., Xu, Y., Zhang, S. & Hou, J. Recent Progress in Chlorinated Organic Photovoltaic Materials. *Acc. Chem. Res.* **53**, 822–832 (2020).
4. Zhu, G., et al. Rechargeable Na/Cl2 and Li/Cl2 batteries. *Nature* **596**, 525–530 (2021).
5. Trost, B. M. & Fleming, I. *Comprehensive Organic Synthesis: Selectivity, Strategy, and Efficiency in Modern Organic Chemistry.* (Pergamon Press, Oxford, England New York, 1991).
6. Wang, X., et al. The role of chlorine in global tropospheric chemistry. *Atmospheric Chemistry and Physics* **19**, 3981–4003 (2019).
7. Molina, M. J. & Rowland, F. S. Stratospheric sink for chlorofluoromethanes: chlorine atom-catalysed destruction of ozone. *Nature* **249**, 810–812 (1974).
8. Bierson, C. J. & Zhang, X. Chemical Cycling in the Venusian Atmosphere: A Full Photochemical Model From the Surface to 110 km. *JGR Planets* **125**, e2019JE006159 (2020).
9. Marov, M. Y. A., et al. Venera 8: Measurements of Temperature, Pressure and Wind Velocity on the Illuminated Side of Venus 1. *Journal of the Atmospheric Sciences* **30**, 1210–1214 (1973).

10. Marov, M. Ya., Lystsev, V. E., Lebedev, V. N., Lukashevich, N. L. & Shari, V. P. The structure and microphysical properties of the Venus clouds: Venera 9, 10, and 11 data. *Icarus* **44**, 608–639 (1980).
11. García Muñoz, A., Mills, F. P., Slanger, T. G., Piccioni, G. & Drossart, P. Visible and near-infrared nightglow of molecular oxygen in the atmosphere of Venus. *Journal of Geophysical Research* **114**, E12002 (2009).
12. DeMore, W. B. & Yung, Y. L. Catalytic Processes in the Atmospheres of Earth and Venus. *Science* **217**, 1209–1213 (1982).
13. Chao, W., Yin, C., Takahashi, K. & Lin, J. J.-M. Hydrogen-Bonding Mediated Reactions of Criegee Intermediates in the Gas Phase: Competition between Bimolecular and Termolecular Reactions and the Catalytic Role of Water. *J. Phys. Chem. A* **123**, 8336–8348 (2019).
14. Nicovich, J. M., Kreutter, K. D. & Wine, P. H. Kinetics and thermochemistry of ClCO formation from the Cl+CO association reaction. *The Journal of Chemical Physics* **92**, 3539–3544 (1990).
15. Mills, F. P. & Allen, M. A review of selected issues concerning the chemistry in Venus' middle atmosphere. *Planetary and Space Science* **55**, 1729–1740 (2007).
16. Hewitt, A. D., Brahan, K. M., Boone, G. D. & Hewitt, S. A. Kinetics and mechanism of the Cl + CO reaction in air. *Int. J. Chem. Kinet.* **28**, 763–771 (1996).
17. Adrian, F. J., Cochran, E. L. & Bowers, V. A. Electron Spin Resonance Spectra of ClCO and ClOO. *The Journal of Chemical Physics* **56**, 6251–6255 (1972).
18. Schnöckel, H., Eberlein, R. A. & Plitt, H. S. Infrared spectra of matrix isolated ClCO and *ab initio* calculation. *The Journal of Chemical Physics* **97**, 4–7 (1992).

19. Chen, S.-H., Chu, L.-K., Chen, Y.-J., Chen, I.-C. & Lee, Y.-P. Detection of ClCO with time-resolved Fourier-transform infrared absorption spectroscopy. *Chemical Physics Letters* **333**, 365–370 (2001).
20. Winiberg, F. A. F., et al. A white cell based broadband transient UV-vis absorption spectroscopy with pulsed laser photolysis reactors for chemical kinetics under variable temperatures and pressures. *Rev. Sci. Instrum.* **94**, 114103 (2023).
21. Baklanov, A. V. & Krasnoperov, L. N. Oxalyl ChlorideA Clean Source of Chlorine Atoms for Kinetic Studies. *J. Phys. Chem. A* **105**, 97–103 (2001).
22. Hemmi, N. & Suits, A. G. Photodissociation of Oxalyl Chloride at 193 nm Probed via Synchrotron Radiation. *J. Phys. Chem. A* **101**, 6633–6637 (1997).
23. Wu, C.-Y., Lee, Y.-P., Ogilvie, J. F. & Wang, N. S. Photolysis of Oxalyl Chloride (ClCO)$_2$ at 248 nm: Emission of CO($v' \leqslant 3$, $J' \leqslant 51$) Detected with Time-Resolved Fourier Transform Spectroscopy. *J. Phys. Chem. A* **107**, 2389–2393 (2003).
24. Baklanov, A. V. & Krasnoperov, L. N. UV Absorption Spectrum and Rate Constant for Self-Reaction of Silyl Radicals. *J. Phys. Chem. A* **105**, 4917–4922 (2001).
25. Krossner, Th., Zülicke, L., Staikova, M. & Peyerimhoff, S. D. Ab initio investigation of the electronic spectrum of the chloroformyl radical ClCO. *Chemical Physics letters* **241**, 511–515 (1995).
26. Francisco, J. S. & Goldstein, A. N. The structure and dissociation energetics of low-lying states of the chloroformyl radical, ClCO. *Chemical Physics* **128**, 367–372 (1988).
27. Bersuker, I. B. Pseudo-Jahn–Teller Effect—A Two-State Paradigm in Formation, Deformation, and Transformation of Molecular Systems and Solids. *Chem. Rev.* **113**, 1351–1390 (2013).

28. Ghosh, B., Papanastasiou, D. K. & Burkholder, J. B. Oxalyl chloride, ClC(O)C(O)Cl: UV/vis spectrum and Cl atom photolysis quantum yields at 193, 248, and 351 nm. *The Journal of Chemical Physics* **137**, 164315 (2012).
29. Burkholder, J. B., et al. JPL Publication 19-5. Chemical Kinetics and Photochemical Data for Use in Atmospheric Studies. *JPL Publication* **19–5**, 2–7 (2020).
30. Danis, F., Caralp, F., Rayez, M. T. & Lesclaux, R. Kinetic study of the reaction trichloromethyl + oxygen + M. fwdarw. trichloromethyl peroxyl + M from 1 to 760 Torr and from 233 to 333 K. *J. Phys. Chem.* **95**, 7300–7307 (1991).
31. Carr, S. A., et al. Experimental and Modeling Studies of the Pressure and Temperature Dependences of the Kinetics and the OH Yields in the Acetyl + O_2 Reaction. *J. Phys. Chem. A* **115**, 1069–1085 (2011).
32. Matthews, D. A., et al. Coupled-cluster techniques for computational chemistry: The CFOUR program package. *J. Chem. Phys.* **152**, 214108 (2020).
33. Neese, F. & Valeev, E. F. Revisiting the Atomic Natural Orbital Approach for Basis Sets: Robust Systematic Basis Sets for Explicitly Correlated and Conventional Correlated *ab initio* Methods? *J. Chem. Theory Comput.* **7**, 33–43 (2011).
34. Knizia, G. & Klein, J. E. M. N. Electron Flow in Reaction Mechanisms-Revealed from First Principles. *Angew. Chem. Int. Ed.* **54**, 5518–5522 (2015).
35. Barbatti, M., et al. Newton-X Platform: New Software Developments for Surface Hopping and Nuclear Ensembles. *J. Chem. Theory Comput.* **18**, 6851–6865 (2022).
36. Crespo-Otero, R. & Barbatti, M. Spectrum simulation and decomposition with nuclear ensemble: formal derivation and application to benzene, furan and 2-phenylfuran. *Theor Chem Acc* **131**, 1237 (2012).

37. Farahani, S., Frandsen, B. N., Kjaergaard, H. G. & Lane, J. R. Simulated Electronic Absorption Spectra of Sulfur-Containing Molecules Present in Earth's Atmosphere. *J. Phys. Chem. A* **123**, 6605–6617 (2019).
38. Frisch, M. J., et al. Gaussian 16 Rev. C.02. (2019).
39. White, J. U. Long Optical Paths of Large Aperture. *J. Opt. Soc. Am.* **32**, 285 (1942).

Chapter 5—The Future: Estimation of the Equilibrium Constant of Cl + CO ⇌ ClCO Reaction by High-Resolution Spectroscopic Data and Theoretical Calculations

5.1—Introduction

The catalytic role of the chlorine atom holds importance in the Earth's atmosphere. Notably, the studies of the ozone degradation in the troposphere, leading to the formation of ozone holes, has garnered significant attention. Given their high reactivity, Cl atoms are also purported to participate in reactions with other pollutants, including organic compounds, NO_2, SO_2, and CO molecules.

As terrestrial planets, both Earth and Venus share a similar atmospheric origin but distinct evolutionary paths stem from Venus' hydrodynamic escape process. Consequently, the natural abundance of Cl atoms in the gas phase of Venus' atmosphere is orders of magnitude higher than that of Earth, underscoring the importance of Cl atom catalysis. For instance, earlier telescope measurements have observed an extremely low O_2 level and high CO_2 level, which has been attributed to the catalytic role of Cl atoms in oxidizing CO into CO_2 via intermediate ClCO radicals. While Mills et al. have modeled this process, the current uncertainty in the equilibrium constant of the association reaction of Cl atoms and CO molecules is approximately a factor of four (2 standard deviations), leading to significantly distinct outcomes in the modeling analysis.

Obtaining an experimental determination of the equilibrium constant may prove challenging, particularly with regards to achieving a small enough uncertainty for modeling purposes. This is due to the potentially perturbations caused by secondary chemistry, such as the ClCO self-reaction or reactions with Cl atom precursors, particularly when Cl concentration is high, and the signal-to-noise (S/N) ratios are moderate. Additionally, the expected absorption cross-section of ClCO is anticipated to be small, further complicating the experimental endeavor. However, statistical thermodynamics has provided a means of estimating thermodynamic properties from molecular properties, by calculating the partition function of reactants and products. With the advent of high-resolution spectroscopic techniques, molecular properties can be determined within a few wavenumbers (1 kJ mol^{-1} = 83.6 cm^{-1}), which is significantly more accurate than traditional thermodynamic methods (a few kJ mol^{-1} accuracy).

This brief report outlines the error propagation inherent in estimating the equilibrium constant from partition functions and organizes the available spectroscopic data on ClCO. However, due to a lack of sufficient experimental data, high-level ab initio calculations were performed to complete the gap in determining the equilibrium constant.

5.2—Methods

5.2.1—Formulas of Partition Functions

For all species, the translational partition function, q_T, is calculated from the thermal wavelength, Λ, as shown below,

$$q_T = \frac{1}{\Lambda^3} \text{ and } \Lambda = \frac{h}{\sqrt{2\pi mkT}}$$

where h denotes the Planck constant, m is the mass of the species, k is the Boltzmann constant and T is the absolute temperature. We note that by using this definition, the translational partition has dimension in length^{-3}.

The rotational partition functions are classified into linear, symmetric top and non-symmetric top species. In our analysis, CO belongs to linear species and ClCO belongs to non-symmetric top species. The used formulas are shown below.

$$q_R = \frac{kT}{\sigma B} \text{ for linear species}$$

$$q_R = \frac{\sqrt{\pi}}{\sigma}\sqrt{\frac{(kT)^3}{ABC}} \text{ for non-symmetric top species}$$

where A, B and C denote the rotational constants. The σ is the rotational symmetry number which is unity for both CO and ClCO.

Under harmonic approximation, the total vibrational partition function is the multiple of the partition functions for each vibrational mode.

$$q_{vib} = \prod_i q_i = \prod_i \frac{1}{1-e^{-h\nu_i/kT}}$$

where index i go through the total number of vibrational modes and ν_i denotes the vibrational frequency.

The simplified formulas for partition function not only allowed us to get an initial result but also be used to estimate the contributions of total error from each degree of freedom. With the available of high-resolution spectroscopic data, we can numerically calculate all the energy levels considering the rovibronic coupling and the anharmonicity for better estimations.

5.2.2—Error Analysis

To calculate the partition function from molecular properties, such as rotational constants, vibrational frequencies, and bond dissociation energy, several approximations must be made. Typically, analytical formulas for the partition functions are available under the high-temperature approximation for the upper atmosphere of Venus, which has a temperature range of 200 - 263 K, corresponding to 1.66 - 2.19 kJ mol^{-1} (139 - 183 cm^{-1}).

Table 1 summarizes the available ClCO properties. First, for translational and rotational motions, the target thermal energy is at least 25 times higher than the typical energies for these motions, so we have adapted the high-temperature formulas. Second, we note that the vibrational frequency is in the same scale as the target thermal energy, which causes a breakdown in the high-temperature approximation. However, we have simplified the calculation by ignoring the anharmonicity and adopting the harmonic oscillator approximation to obtain an initial result. The analytic formula for harmonic oscillator is available for all temperatures. Third, the excited state energy is far higher than the thermal energy except for Cl atom, in which the first excited state is 882.35 cm^{-1} due to the spin-orbital coupling.

Table 5.1. Summary of the available spectroscopic data of the ClCO radicals.

ClCO Properties		Experimental	Theoretical [a]
Rotational Constant / cm^{-1}	A	No Available Data	5.2363 (5.2719)
	B		0.1950 (0.1910)
	C		0.1880 (0.1844)
Frequency / cm^{-1}	CO stretching	1876.7[b] (1884.59)[c]	1906.1 (1943.5)
	ClC stretching	570.1[b]	576.3 (581.4)
	Bending	334.6[b]	343.2 (340.3)
Dissociation Enthalpy/ cm^{-1}	$\Delta H°(0\mathrm{K})$	2413 ± 245 (6.9 ± 0.7)[d]	2226.1 ± 125.4 (26.630 ± 1.5)[e]

[a] Theoretical result calculated at CCSD(T)/cc-pVQZ level without frozen-core approximation. Values in parentheses were calculated at B3LYP/aug-cc-pVTZ level by Ref. 1.

[b] Ar Matrix Isolation by Ref . 2.

[c] Gas phase Measurement by Ref. 1.

[d] Adapted from Ref . 3. Error represents two standard deviations. Values in parentheses in kcal mol^{-1}, conversion factor used 1 kcal mol^{-1} = 349.757 cm^{-1}.

[e] Calculated using the HEAT method. Values in parentheses in kJ mol^{-1}, conversion factor used 1 kJ mol^{-1} = 83.593 cm^{-1}.

Following the literature, the equilibrium constant, K_p, is defined as the association reaction below, where $\Delta H°(0\mathrm{K})$ represents the dissociation reaction enthalpy and $q°$ is the unit conversion factor from number density to pressure.

$$K_p = \frac{P_{\mathrm{ClCO}}}{P_{\mathrm{Cl}}P_{\mathrm{CO}}} = e^{\Delta H^\circ(0K)/kT}\frac{q_{\mathrm{ClCO}}}{q_{\mathrm{Cl}}q_{\mathrm{CO}}}q^\circ$$

Considering the differential forms for each term, the individual errors were estimated using the following formulas.

$$\frac{dq_R}{q_R} = \frac{1}{2}\frac{dB}{B}$$

$$\frac{dq_i}{q_i} = \frac{ue^{-u}}{1-e^{-u}}\frac{d\nu_i}{\nu_i} \text{ where } u = \frac{h\nu_i}{kT}$$

$$\text{Let } \alpha = e^{E/kT}\text{, then } \frac{d\alpha}{\alpha} = \frac{dE}{kT}$$

Because the properties of the Cl atom and CO molecule are well studied, the error in the rotational constant and vibrational frequency of CO is approximately 0.3%, significantly smaller than the errors from ClCO. Furthermore, we observed that the primary source of error arises from the exponential term due to the accuracy of reaction enthalpy. By assuming a thermal energy of about 160 cm^{-1}, an error of approximately 1 kJ mol^{-1} results in a relative error of 54% in the estimated equilibrium constant, but it is still better than the literature values.

We emphasize that the relative error in rotational constants and vibrational frequencies can be determined spectroscopically with an accuracy of less than 1%. In addition, the dissociation energy could be determined within a few tens wavenumbers, which contributes to a relative error of about 10%. Therefore, high-resolution spectroscopic investments on ClCO are necessary for narrowing down the accuracy.

5.2.3—Theoretical Calculations

The largest contributor to the error in estimating the equilibrium constant is the accuracy of the bond dissociation energy, which is challenging to measure in spectroscopic resolution. To address this, we estimated the bond dissociation energy using the HEAT (High-accuracy Extrapolated Ab initio Thermochemistry-345(Q))[4] method developed by Dr. Stanton. This method has been shown to push the current limit (~1kcal mol^{-1}) of the art of calculations to a new level of accuracy (~1 kJ mol^{-1}) for species containing only first and second row elements of the periodic table.

Following the HEAT method, we conducted a comparison of the dissociation energy for ten reactions involving Cl atoms (see Table 2 and Table 3). Our analysis indicated that the largest error in our calculated bond dissociation energy is approximately ±1.5 kJ mol^{-1}. Additionally, we optimized the geometry and calculated the vibrational frequency, including anharmonicity, providing sufficient information to calculate the equilibrium constants using theoretical parameters (blue line, Figure 1).

We would like to mention that Dr. Stanton's group has developed modified versions of the HEAT method, called mHEAT,[5] that reduce the computational resources required. However, we chose not to use this method in our calculations because the current ANO basis set used for geometry optimization and vibrational frequency calculations does not support third-row elements and mHEAT has been shown to have larger errors compared to the original HEAT method.

Table 5.2. Individual contributions to the HEAT total energies. All values in hartree.

Species	E^{∞}_{HF}	$\Delta E^{\infty}_{\mathrm{CCSD(T)}}$	$\Delta E_{\mathrm{CCSDT}}$	$\Delta E_{\mathrm{CCSDTQ}}$	ΔE_{REL}	ΔE_{DBOC}	ΔE_{SO}[a]	ΔE_{ZPE}	Total
Cl	-459.489895	-0.665245	-0.000767	-0.000161	-1.404007	0.005940	-0.001338	0.000000	-461.555473
Cl_2	-919.010527	-1.395247	-0.000841	-0.000707	-2.807659	0.011876	0.000000	0.001264	-923.201840
ClF	-558.920189	-1.069579	-0.000466	-0.000906	-1.490974	0.008526	0.000000	0.001790	-561.471797
HCl	-460.112773	-0.713921	-0.000541	-0.000265	-1.403590	0.006143	0.000000	0.006774	-462.218173
HOCl	-534.934722	-1.053208	-0.000301	-0.000999	-1.455927	0.008474	0.000000	0.013103	-537.423580
ClO	-534.319275	-1.006841	-0.001190	-0.000857	-1.456078	0.008308	-0.000724	0.001944	-536.774715
H_3CCl	-499.157012	-0.974687	-0.000558	-0.000509	-1.418406	0.008290	0.000000	0.037525	-501.505357
HCCCl	-535.786624	-1.162003	0.000155	-0.001355	-1.433294	0.009386	0.000000	0.018817	-538.354918
ClCOH	-572.881607	-1.269522	-0.000207	-0.001347	-1.470767	0.010167	0.000000	0.019016	-575.594267
ClCN	-551.844260	-1.200184	0.000305	-0.001711	-1.447795	0.009541	0.000000	0.008598	-554.475506
ClOO	-609.146947	-1.334064	Working	Working	-1.508675	0.010756	0.000000	0.004193	Working
ClCO	-572.259204	-1.235703	-0.000513	-0.001413	-1.471009	0.009955	0.000000	0.006536	-574.951351

[a] Values adopted from the CCCBDB database, II.C.2 Electronic Spin Splitting Corrections.

Table 5.3. Comparisons of the HEAT energies to the reaction enthalpies at 0 K from the ATcT table. All values in kJ mol^{-1}.

Reaction [a]	$\Delta H°$(0 K, ATcT) [b]	$\Delta H°$(0 K, HEAT) [c]	$\Delta H°$(0 K, HEAT – ATcT)
$Cl_2 \rightarrow 2\ Cl$	239.242 ± 0.002	238.639	-0.60
$ClF \rightarrow Cl + F$	252.496 ± 0.034	251.851	-0.64
$HCl \rightarrow Cl + H$	427.643 ± 0.006	427.805	0.16
$HOCl \rightarrow Cl + OH$	230.739 ± 0.036	229.539	-1.20
$ClO \rightarrow Cl + O$	265.341 ± 0.035	264.194	-1.15
$H_3CCl \rightarrow Cl + CH_3$	344.223 ± 0.169	343.649	-0.57
$HCCCl \rightarrow Cl + CCH$	454.061 ± 0.474	452.598	-1.46
$ClCOH \rightarrow Cl + HCO$	340.872 ± 0.677	342.199	1.33
$ClCN \rightarrow Cl + CN$	421.181 ± 0.481	421.744	0.56
$ClCO \rightarrow Cl + CO$		26.630	

[a] The HEAT Energies not shown in Table S1 were adapted from Ref. 4.

[b] Error correspond to estimated 95% confidence limits..

[c] Conversion factor used 1 hartree = 2625.4976 kJ mol^{-1}.

5.3—Results

Figure 1 displays a comparison between the calculated equilibrium constant (blue lines) and literature values (red), along with error bars for a few representative temperatures. The calculated error bars are approximately half the size of those reported in the literature. The calculated equilibrium constants are summarized in Table 4. The detailed parameters used to estimate the equilibrium constant are listed in Table 5.

We found the calculated has less deviation from the literature at high temperature, which agrees with the behavior using high-temperature approximation to calculate the partition functions. Moreover, the calculated value is smaller than the literature, other relatively small contributions from anharmonicity, centrifugal distortion and vibronic coupling, each may contribute a few percent in the calculated error, could account for the small difference.

Herein, we conducted high-level calculations to determine the dissociation enthalpy of ClCO to form Cl atom and CO using the HEAT method. The calculated energy was estimated to have a maximum error of about 1.5 kJ mol^{-1} (125 mol^{-1}). Additionally, we demonstrated that high-resolution spectroscopy data can be used to estimate the equilibrium constant. We strongly recommend further investigations into the molecular properties of the ClCO radical, including bond dissociation energy, vibrational and rotational spectra. With these high-resolution spectroscopic data, a better estimation on partition function could be calculated numerically and possibly to reduce the error to ~10% for obtaining meaningful results from modeling works.

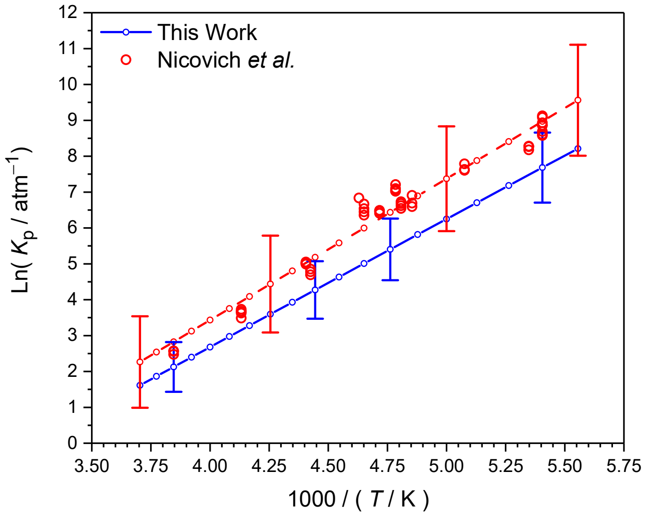

Figure 5.1. Van't Hoff plot for comparison with the literature values. The error presents two standard deviations.

Table 5.4. The calculated equilibrium constants at distinct temperatures.

T / K	K_p / atm^{-1}
180	3683.923
185	2170.285
190	1313.530
195	815.073
200	517.596
205	335.818
210	222.271
215	149.878
220	102.832
225	71.707
230	50.767
235	36.458
240	26.534
245	19.556
250	14.584
255	10.998
260	8.382
265	6.451
270	5.012

Table 5.5 Summary of parameters used in calculating the equilibrium constant.

Cl	m / kg	5.81×10^{-26} (35)[a]
	g_e(Cl)	4
	E(Cl*) / cm^{-1}	882.35
	g_e (Cl*)	2
CO	m / kg	4.65×10^{-26} (28)[a]
	g_e	1
	ν_{CO} / cm^{-1}	2169.81
	B / cm^{-1}	1.93128
ClCO	m / kg	10.47×10^{-26} (63)[a]
	g_e	2
	ν_{CO} / cm^{-1}	1906.1
	ν_{ClC} / cm^{-1}	576.3
	ν_{Bend} / cm^{-1}	343.2
	A / cm^{-1}	5.2363
	B / cm^{-1}	0.1950
	C / cm^{-1}	0.1880

[a] Values in parentheses represents the nominal mass.

5.4—References

1. Chen, S.-H., Chu, L.-K., Chen, Y.-J., Chen, I.-C. & Lee, Y.-P. Detection of ClCO with time-resolved Fourier-transform infrared absorption spectroscopy. *Chemical Physics Letters* **333**, 365–370 (2001).
2. Schnöckel, H., Eberlein, R. A. & Plitt, H. S. Infrared spectra of matrix isolated ClCO and *ab initio* calculation. *The Journal of Chemical Physics* **97**, 4–7 (1992).
3. Nicovich, J. M., Kreutter, K. D. & Wine, P. H. Kinetics and thermochemistry of ClCO formation from the Cl+CO association reaction. *The Journal of Chemical Physics* **92**, 3539–3544 (1990).
4. Tajti, A., et al. HEAT: High accuracy extrapolated *ab initio* thermochemistry. *The Journal of Chemical Physics* **121**, 11599–11613 (2004).
5. Thorpe, J. H., et al. High-accuracy extrapolated *ab initio* thermochemistry. IV. A modified recipe for computational efficiency. *J. Chem. Phys.* **150**, 224102 (2019).

Chapter 6—Chemical Kinetic Study of the Reaction of CH_2OO with CH_3O_2

This chapter is reprinted and adapted with permission from J. Phys. Chem. Lett, 14, 13, 3690 - 3697. Copyright 2024, American Chemical Society.

6.1—Abstract

Criegee intermediates play an important role in the oxidizing capacity of the Earth's troposphere. Although extensive studies have been conducted on Criegee intermediates in the past decade, their kinetics with radical species remain underexplored. We have investigated the kinetics of the simplest Criegee intermediate, CH_2OO, with the methyl peroxy radical, CH_3O_2, as a model system to explore the reactivities of Criegee intermediates with peroxy radicals. Using a multipass UV-Vis spectrometer coupled to a pulsed-laser photolysis flow reactor, CH_2OO and CH_3O_2 were generated simultaneously from the photolysis of $CH_2I_2/CH_3I/O_2/N_2$ mixtures with CH_2OO measured directly near 340 nm. We determined a reaction rate coefficient $k_{\mathrm{CH2OO+CH3O2}} = (1.7 \pm 0.5)\times10^{-11}$ cm^3 s^{-1} at 294 K and 10 Torr, where the influence of iodine adducts is reduced. This rate coefficient is faster than previous theoretical predictions, highlighting the challenges in accurately describing the interaction between zwitterionic and bi-radical characteristics of Criegee intermediates.

6.2—Introduction

Carbonyl oxides, also known as Criegee intermediates, play critical roles in the Earth's troposphere.[1–3] These intermediates arise from the ozonolysis of unsaturated organic compounds, such as isoprene, and are believed to enhance the atmosphere's oxidation capacity. They also contribute to the formation of secondary organic aerosols (SOA) and ultrafine particles, especially in biogenic rich atmospheres like that of the Amazon rainforest.[2–4] Laboratory chamber experiments have shown that different oligomers are generated as secondary products of ozonolysis reactions in the presence of different OH radical scavengers, resulting in the production of different peroxy radicals.[5,6] Moreover, a recent study on the chemical composition of SOA from β-pinene ozonolysis revealed that the aerosol composition is predominantly influenced by reactions of stabilized Criegee intermediates with the corresponding peroxy radicals.[7]

In laboratory studies, small Criegee intermediates (with three carbon atoms or fewer) are generated through the photolysis of diiodoalkanes.[8,9] Their spectroscopic characteristics have been extensively studied, providing valuable insights into their reactivities.[10] As a result of the pronounced zwitterionic nature of the C=O–O functional group,[11] the reactivities of some Criegee intermediates depends heavily on their structures. For example, the *anti*-conformers (where a hydrogen atom aligns with the terminal oxygen) undergo rapid reactions with hydrogen-bonding molecules, such as H_2O, NH_3 and CH_3OH, via a 1,2-insertion mechanism into the hydrogen-bond.[12] Conversely, the *syn*-conformers (where other substitution groups align with the terminal oxygen) react slowly with hydrogen-bonding molecules but can rapidly decompose to yield OH radicals.[13]

The oxidation of SO_2 and NO_2 via reactions with Criegee intermediates, generating SO_3 and Criegee-NO_2 adducts, only show weak structural dependencies.[9,14] Isoprene-derived Criegee intermediates, such as methyl vinyl ketone oxide[15] and methacrolein oxide[16], display similar reactivity in the reaction with SO_2 to their smaller counterparts. This suggests that small Criegee intermediates can be used as analogues to understand the behavior of larger ones, greatly reducing the computational cost for high-level *ab initio* calculations.

While the reactivities of small Criegee intermediates with stable molecules has been thoroughly investigated,[10,17] there is a notable gap in our understanding of their interactions with radical species. Welz et al. determined a rate coefficient of $\leq 6\times10^{-14}$ cm^3 s^{-1} and 7×10^{-12} cm^3 s^{-1} for the reactions of the simplest Criegee intermediate, CH_2OO, with NO and NO_2, respectively.[8] Further studies on reactions of *syn*-CH_3CHOO,[9] *anti*-CH_3CHOO[9] and $(CD_3)_2COO$[18] with NO_2 have similar rate coefficients near 2×10^{-12} cm^3 s^{-1}. Chhantyal-Pun et al.[19] measured fast reaction rate coefficients for methyl peroxy, CH_3O_2, and acetyl peroxy radicals, $CH_3C(O)O_2$, reporting the rate coefficients $k(CH_2OO + RO_2$, RO_2 = CH_3O_2 or $CH_3C(O)O_2)$ = $(2.4 \pm 1.2)\times10^{-11}$ cm^3 s^{-1} with weak temperature (243–310 K) effects.[19]

Criegee intermediates are unique, exhibiting both zwitterionic and biradical characters, with respect to reaction pathways. From the zwitterionic perspective, the reactions of Criegee intermediates with radicals are expected to be slow. However, the bi-radical perspective predicts a fast rate similar to a typical radical-radical association reaction.[20] Theoretical calculations indicate that the CH_2OO + CH_3O_2 reaction passes through a submerged barrier, yielding a fast rate coefficient of 4×10^{-12} cm^3 s^{-1} at 290 K,[21] suggesting a pronounced bi-radical character in contrast to the widely accepted zwitterionic perspective.

In this work, we have investigated the reaction kinetics of CH_2OO + CH_3O_2 at 294 K and 10 Torr total pressure. CH_2OO and CH_3O_2 were generated through the photolysis of diiodomethane, CH_2I_2, and iodomethane, CH_3I, respectively, in the presence of oxygen. We monitored the near-UV absorption using a White cell multipass UV-Vis spectrometer coupled to a pulsed-laser photolysis flow reactor,[22] and constructed a chemical kinetics model to analyze the measured temporal profiles. The absorption cross-sections of the species that can be characterized in our experimental system are summarized in figure S1.

6.3—Results and Discussion

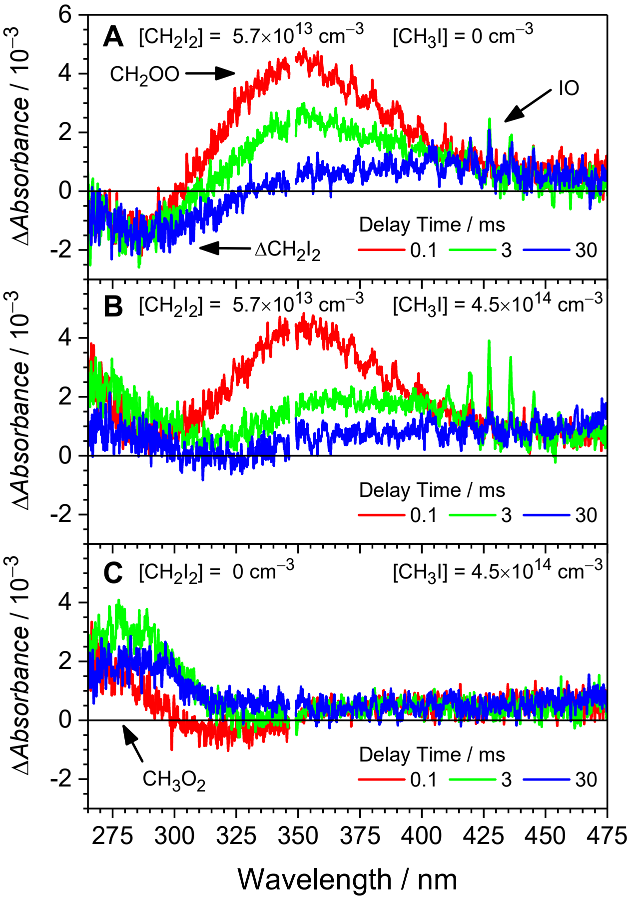

Figure 6.1. Representative absorption spectra of the photochemical systems containing (A) only CH_2I_2, (B) both CH_2I_2 and CH_3I, and (C) only CH_3I at selected delay times (gate width = 117.5 μs and 1024 laser shot average) at 50 Torr and 294 K. Each spectrum is composed of two measurements using a 600 grooves/mm grating with center wavelength 280 nm and 413 nm (spectral coverage ±63 nm); thus, a small spectral gap of 7 nm appears in our spectra. The absorption features of CH_2OO, IO, CH_2I_2 and CH_3O_2 are indicated. Note that the absorption signals below 325 nm are different at 0.1 ms (red) and 3 ms (green) in the presence of CH_3I.

In the $CH_2I_2/O_2/N_2$ photolysis system ($CH_2I_2 + h\nu \rightarrow CH_2I + I$, $CH_2I + O_2 \rightarrow CH_2OO + I$, $k_{CH2I+O2} = 1.5\times10^{-12}$ cm^3 s^{-1})[23], the CH_2I radical exhibited a lifetime of less than 2 μs at 10 Torr of O_2, resulting in the prompt formation of CH_2OO. As anticipated, the characteristic absorptions from CH_2OO near 340 nm and IO around 430 nm were clearly visible. Additionally, a negative absorption near 300 nm was observed, which was attributed to the depletion of CH_2I_2 due to photolysis as illustrated in Figure 1A.

Figure 1B presents the spectra from photolysis of an $N_2/O_2/CH_2I_2/CH_3I$ mixture at 50 Torr total pressure. The CH_3O_2 radicals were generated via the photolysis of CH_3I followed by the reaction of the resulting CH_3 radical with O_2 ($CH_3I + h\nu \rightarrow CH_3 + I$, $CH_3 + O_2 + M \rightarrow CH_3O_2 + M$, $k_{CH3+O2} = 2.7\times10^{-13}$ cm^3 s^{-1} at 50 Torr);[24] the CH_3 radical lifetime was roughly 12 μs at 10 Torr of O_2, leading to the immediate formation of CH_3O_2. Based on the collisional energy transfer parameter for modeling the pressure dependence of $CH_3 + O_2$ reaction,[25] we estimate that CH_3O_2 reaches thermal equilibrium within 0.5 ms even though its formation is highly exothermic (30 kcal mol^{-1}). The initial signal intensity for CH_2OO remained unchanged upon the introduction of CH_3I, suggesting that the formations of CH_2OO and CH_3O_2 were both rapid and independent. The absorption signals of IO were observed at 3 ms, attributable to the increased iodine atom concentration following CH_3I photolysis. Yet, in the absence of CH_2I_2 (Figure 1C), no IO was detected, implying that IO primarily stemmed from the chemistry involving CH_2I and CH_2OO.

The CH_2OO was monitored near 340 nm, where both CH_3O_2 and CH_3I have negligible absorption cross-sections. Figure 2 shows the temporal profiles of CH_2OO as a function of [CH_3I] at 10 and 50 Torr total pressures. At 50 Torr (Figure 2B), the decay rates increased with [CH_3I] but remained the same for [CH_3I] > 8.5×10^{14} cm^{-3}. Furthermore, an increase in absorption was observed at longer times for the higher [CH_3I] runs. At lower [CH_3I], the longtime signals were negative, attributed to photolytic depletion of CH_2I_2. However, at higher [CH_3I], positive signals were recorded at longer times, with the intensity being proportional to [CH_3I] (Figure S2). Additionally, we noted that this shift became more pronounced at 90 Torr and 238 K (Figure 2C) and it was significantly minimized at 10 Torr and 294 K (Figure 2A).

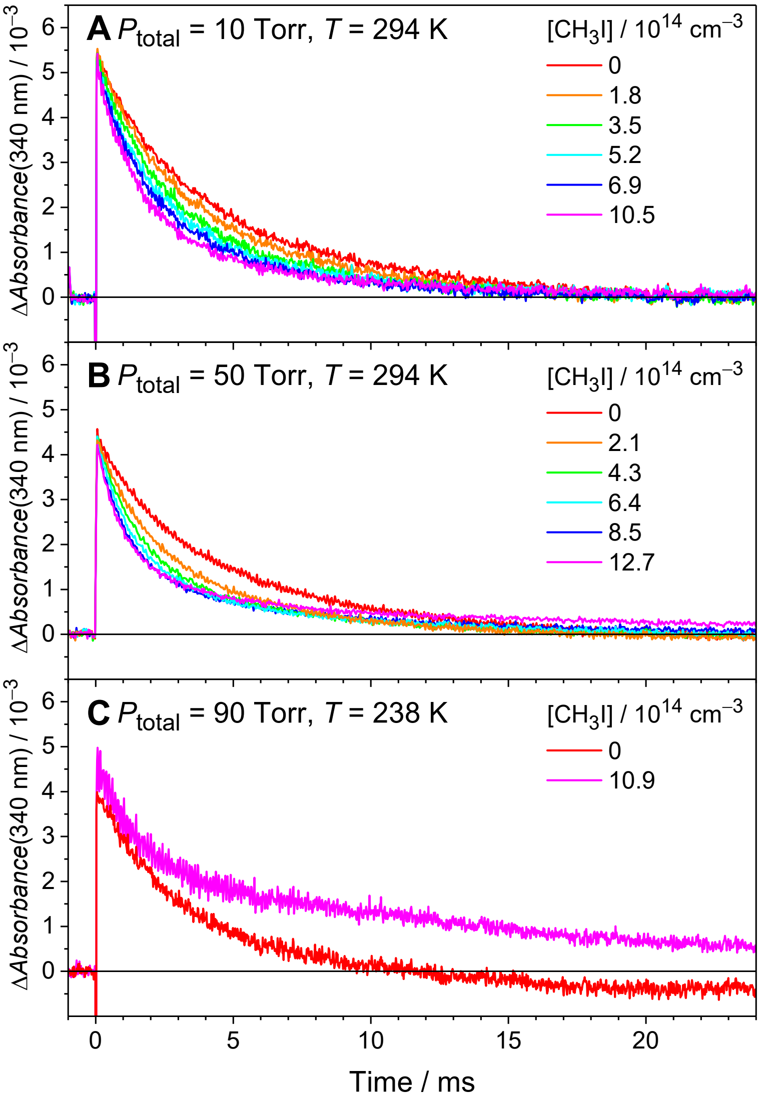

Figure 6.2. Representative temporal profiles near 340 nm at various [CH_3I] with a total pressure and temperature of (A) 10 Torr, 294 K, (B) 50 Torr, 294 K, and (C) 90 Torr, 238 K. The O_2 pressures are 9 Torr, 10 Torr and 5 Torr for (A), (B), and (C), respectively. Note that the baseline shift is less obvious at 10 Torr and 294 K.

We have considered IO, ICH_2OO and CH_3OOI as possible candidates that would explain the observed features at longer delay time. First, we note the absorption of IO is far smaller than the expected absorbance of 0.02 near 427 nm, σ_{IO}(427 nm) / σ_{IO}(340 nm) = 1.44×10^{-17} cm^2 / 2.84×10^{-19} = 50.7.[26] Second, a residual absorption signal at 340 nm, attributed to the ICH_2OO adduct, has been observed when CH_2OO was fully scavenged by water vapor.[27] However, we did not observe any distinct absorption features from ICH_2OO within our detection window. Even under ideal conditions for the formation of ICH_2OO, where the yield is expected to be greater than 30% (20−90 Torr and 238 K),[28] the absorption could be comprehensively accounted for by ΔCH_2I_2, CH_2OO, and IO (Figure S4−S6), indicating that it is unlikely to be the carrier. Lastly, an absorption signal was observed when only $CH_3I/O_2/N_2$ mixture was introduced to the reactor at lower temperatures (Figure S7, green trace). The profile was indicative of a secondary product from a strong absorption feature with peak near 290 nm (Figure S8), which has been previously assigned to CH_3OOI.[29]

We observed the absorption feature became stronger at lower temperatures (figures S3), in line with the formation through the $CH_3O_2 + I \rightarrow CH_3OOI$ association reaction. Also, the absorption feature at short wavelengths, which is dominated by CH_3O_2, remained unchanged at 10 Torr (Figure S11) compared to 50 Torr (Figure 1). Nevertheless, we observed a small absorption signal at 340 nm ($<5\times10^{-4}$ in absorbance) in the absence of CH_2I_2 for the photolysis of $CH_3I/N_2/O_2$ mixture (Figure S15). The absorption cross-section of CH_3OOI near 290 nm[29] has been reported to be 8.8×10^{-18} cm^2 and we estimated an absorption cross-section near 340 nm[30] of 2×10^{-18} cm^2 based on the relative profiles. The maximum [CH_3OOI] in our experiments at 10 Torr will be less than 5×10^{11} cm^{-3} ($L_{eff} \approx 450$ cm). A background subtraction to eliminate the minor influence of CH_3OOI (<10% of the initial CH_2OO signals, Figure S15) was applied to the CH_2OO temporal profiles.

Table 6.1. Summary of the rate coefficients of the chemical kinetics model for the kinetic analysis.

Comments	Reactions[a]	Rate Coefficients at 298 K and 10 Torr[b]	Notation
CH_2OO Chemistry	$CH_2I_2 + h\nu \rightarrow CH_2I + I$	Instantaneous	-
	$CH_2I + O_2 \rightarrow CH_2OO + I$	1.13×10^{12}[c]	k_{1a}[31]
	$CH_2I + O_2 \rightarrow H_2CO + IO$	1.5×10^{13}	k_{1b}[32]
	$CH_2I + O_2 \rightarrow$ Other Products	2.2×10^{13}[d]	k_{1c}[31]
	$CH_2OO + I \rightarrow H_2CO + IO$	$(2.2 \pm 1.1)\times10^{12}$	k_2[33]
	$CH_2OO + CH_2OO \rightarrow 2\ H_2CO + O_2$	$(7.4 \pm 0.6)\times10^{11}$	k_3[34]
Iodine Chemistry	$I + I \rightarrow I_2$	6.2×10^{15}	k_4[30]
	$IO + IO \rightarrow$ Products	9.9×10^{11}	k_5[35]
CH_3O_2 Chemistry	$CH_3I + h\nu \rightarrow CH_3 + I$	Instantaneous	-
	$CH_3 + O_2 \rightarrow CH_3O_2$	9.2×10^{14}	k_6[24]
	$CH_3O_2 + CH_3O_2 \rightarrow 2\ CH_3O + O_2$	$(2.0 \pm 0.9)\times10^{13}$	k_7[36]
	$CH_3O + CH_3O \rightarrow H_2CO + CH_3OH$	7.0×10^{11}	k_8[37]
	$CH_3O + O_2 \rightarrow H_2CO + HO_2$	1.9×10^{15}	k_9[24]
	$CH_3O + HO_2 \rightarrow$ Products[e]	1.1×10^{10}	k_{10}[37]
	$HO_2 + HO_2 \rightarrow H_2O_2 + O_2$	1.4×10^{12}	k_{11}[24]
CH_3OOI Chemistry	$CH_3O_2 + I \rightarrow CH_3OOI$	2.9×10^{12}[f]	k_{12}[29]
	$CH_3OOI + I \rightarrow CH_3O_2 + I_2$	1.5×10^{10}	k_{13}[29]
Target Reaction	$CH_2OO + CH_3O_2 \rightarrow$ Adduct	$(1.7 \pm 0.5)\times10^{11}$	$k_{CH2OO+CH3O2}$

[a] The first-order diffusion was simulated using $C_{diff} \times m^{-0.5}$ formula for radical species, including CH_2OO, CH_3O_2, CH_3O, HO_2, IO and I atom, where C_{diff} denotes for the proportional constant and m denotes the molar mass.

[b] Unit: $cm^3\ s^{-1}$. The reaction rate coefficients with uncertainty were considered in the Monte Carlo error analysis procedure.

[c] The $CH_2I+O_2 \rightarrow$ Products reaction rate coefficients $k_1 = 1.5\times10^{-12}\ cm^3\ s^{-1}$. The listed rate coefficients are derived based on the measured yield of Ref. 28.

[d] The reaction rate coefficients were derived as $k_{1c} = k_1 - k_{1a} - k_{1b}$ to match the yield of CH_2OO.

[e] Calculations from Ref 37 suggest $CH_2O + H_2O_2$ and $CH_3OH + O_2(^3P)$ as products on the singlet and the triplet potential energy surfaces, respectively.

[f] Assuming a linear pressure dependence and derived from $2\times10^{-11}\ cm^3\ s^{-1}$ at 70 Torr of Ref. 29.

As mentioned previously, these traces were analyzed using a chemical kinetics model, with the reactions considered listed in Table 1. These reactions were classified into those involving CH_2OO (reactions k_1–k_3), iodine species (reactions k_4 and k_5), CH_3O_2 (reactions k_6–k_{11}) and CH_3OOI (reactions k_{12} and k_{13}). We also considered the lumped first-order decay due to diffusion or wall loss (C_{diff}). The CH_2OO + I reaction (k_2) and the CH_2OO self-reaction (k_3) dominate the observed CH_2OO decay in the absence of co-reactants. We found that the modeled [CH_2OO] reproduced the measured temporal profiles at 10 Torr (Figure S12). At [CH_2I_2] = 5.1×10^{13} cm^{-3} and 2.6×10^{13} cm^{-3}, the obtained C_{diff} values were (796 ± 11) and (701 ± 7) s^{-1} $g^{0.5}$ $mol^{-0.5}$, which correspond to first-order decay rates of (117 ± 2) and (103 ± 1) s^{-1}, respectively. These values agreed with the natural decay of CH_2OO in our flow reactor (Figure S13 and S14) and were adopted for analyzing the CH_2OO + CH_3O_2 reaction rate coefficients.

These fits yielded rate coefficients $k_2 = (2.30 \pm 0.12)\times10^{-12}$ cm^3 s^{-1} and $k_3 = (7.81 \pm 0.32)\times10^{-12}$ cm^3 s^{-1}, with errors representing one standard deviation. Previous studies have been conducted to model the photolysis of $CH_2I_2/O_2/N_2$ mixtures, monitoring the signals of CH_2OO, IO, and iodine atom over 10–760 Torr.[31–34,38–40] For the CH_2OO + I reaction (k_2), there is prevailing consensus in the literature indicating a slow rate coefficient of approximately 2×10^{-12} cm^3 s^{-1} below 10 Torr, which is in agreement with our results. We note that there is no clear agreement in the literature for the rate coefficient of CH_2OO + I reaction at pressures of 50 Torr and above;[31–34,38–40] therefore, only the temporal profiles recorded at 10 Torr were analyzed to obtain the rate coefficient for CH_2OO + CH_3O_2 .

In previous studies, CH_3OOI was assumed to react rapidly with I atoms (k_{13} = 1.5×10^{-10} cm^3 s^{-1})[29] to regenerate CH_3O_2 and produce I_2, in order to explain the fast formation of I_2 and the overestimation of CH_3O_2 concentration. For the $CH_3OO + I \rightarrow CH_3OOI$ reaction, calculations[41] predict a strong pressure dependence with the fall-off region from 10^{-4} to 1000 Torr and Dillon et al.[29] reported a rate coefficient $k_{12} = 2\times10^{-11}$ cm^3 s^{-1} at 70 Torr. By assuming a linear pressure dependence, we estimated $k_{12} = 2.9\times10^{-12}$ cm^3 s^{-1} at 10 Torr. In the kinetic fitting, we varied k_{12} from 0 to 2×10^{-11} cm^3 s^{-1} to estimate the influence of CH_3OOI formation, which effectively decreases the [CH_3O_2] and [I].

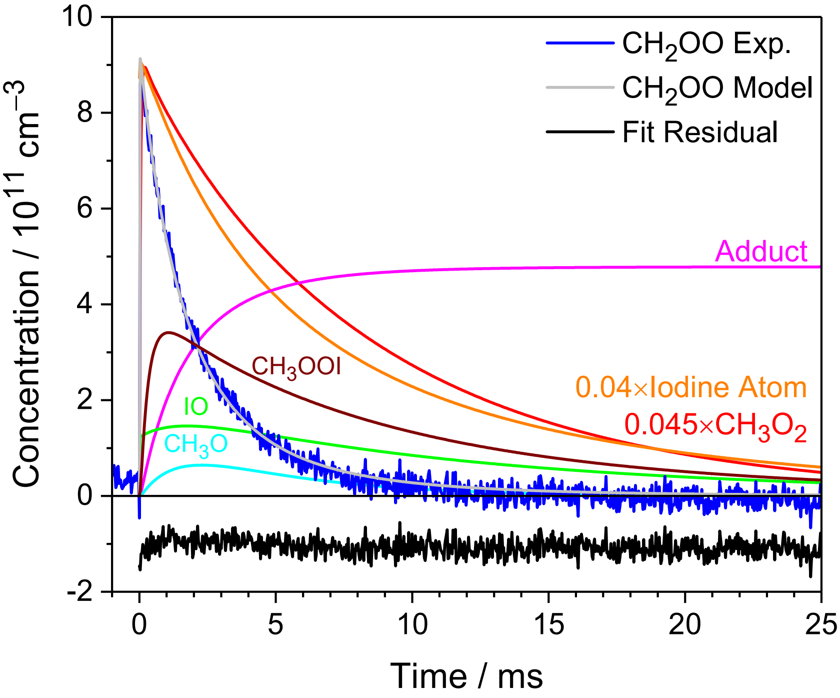

Figure 6.3. Representative experimental (blue) and modeled (smooth lines) temporal profiles. The residual (black) have been offset in the figure to avoid overlap with the measured profiles. The model profiles of [CH_3O_2] (red) and [I] (orange) were scaled for comparison. The magenta line shows the product formation from CH_2OO + CH_3O_2 reaction; P_{O2} = 9.5 Torr, [CH_2I_2] = 5.1×10^{13} cm^{-3}, and [CH_3I] = 1.1×10^{15} cm^{-3}, balanced with N_2 to 10.0 Torr at 294 K. The concentration of CH_2OO was derived using L_{eff} = 450 cm and σ_{CH2OO}(340nm) = 1.2×10^{-17} cm^2. The profile was corrected for the negative absorption of ΔCH_2I_2, which resulted in a positive concentration before the time zero.

Figure 3 displays a representative fit of the temporal profile of CH_2OO along with modeled CH_3OOI, IO, CH_3O, CH_3O_2 and I. The concentrations of each species at a delay of 0.2 ms were obtained by performing a least-squares-fit of the recorded spectra (figure S16 as an example) to the reported absorption cross-section (Figure S1). The effective absorption length ($L_{\mathrm{eff}} \approx 450$ cm) was characterized by previous measurements of NO_2.[22]

The fit was highly sensitive to the accurate determination of $[CH_3O_2]_{t=0}$, for which we utilized two different approaches. First, we extrapolated the $[CH_3O_2]$ to t=0. However, as shown in figure S16, there was considerable spectral overlap of the CH_3I and CH_3O_2 which could result in significant errors. A second approach was to utilize the relative depletion of ΔCH_2I_2 to ΔCH_3I, assuming that photolysis of CH_3I yields 100% CH_3O_2 and using the known absorption cross-sections of both precursors at 248 nm.[24] The $[CH_3O_2]$ derived from both methods were consistent with an uncertainty of 20% (one standard deviation) in all except in a few measurements at lower $[CH_3I]$ (Figure S17).

The uncertainty of the fitted $CH_2OO + CH_3O_2$ reaction rate coefficients was estimated using a Monte Carlo fitting procedure, by performing multiple fits with randomly varied fixed parameters taking into account the literature uncertainty (assuming a normal distribution) in the rate coefficients of $CH_2OO + I$ (k_2), $CH_2OO + CH_2OO$ (k_3) and $CH_3O_2 + CH_3O_2$ (k_7) rate coefficients, as well as the 20% error of $[CH_3O_2]$ (Figure S21–S23, Table S1). The modeled concentrations of both CH_2OO and CH_3O_2 were found to be the most sensitive to these reactions in our model. This error analysis procedure produced a distribution of values for the target rate coefficient (Figure S21), which represents the error propagation. We determined the rate coefficient as the mean value and the error as one standard deviation of the distribution.

The mean rate coefficients as a function of $[CH_3I]$ are summarized in Figure 4. The modeled reaction rate coefficients were constant, within experimental error, as a function of $[CH_3I]$ and $[CH_2I_2]$ which were varied by an order of magnitude and a factor of two, respectively. A rate coefficient of $k_{\mathrm{CH2OO+CH3O2}} = (1.7 \pm 0.5)\times10^{-11}$ cm^3 s^{-1} was derived from our data at 10 Torr and 294 K. Including the formation of CH_3OOI increases the determined $k_{\mathrm{CH2OO+CH3O2}}$ by 6% by reducing the concentration of CH_3O_2 and I atoms, but the effect is relatively small in comparison to the overall uncertainty.

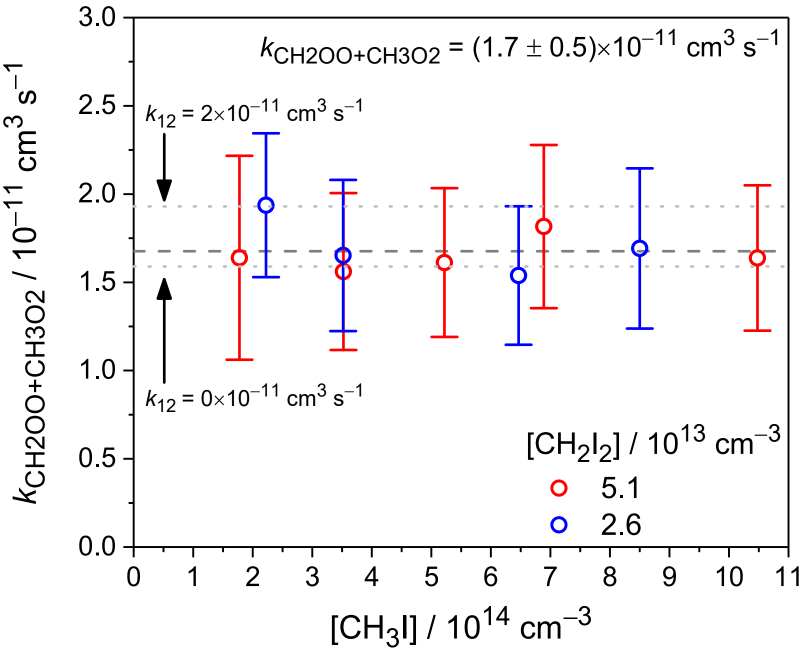

Figure 6.4. Summary of the fitted $CH_2OO + CH_3O_2$ reaction rate coefficients, $k_{CH2OO+CH3O2}$, for distinct [CH_3I] and [CH_2I_2] at 10 Torr and 294 K. The $CH_3OO + I \rightarrow CH_3OOI$ rate coefficient (k_{12}) was set to 2.9×10^{-12} cm^3 s^{-1}. Error bars represent one standard deviation of the distribution of $k_{CHH2OO+CH3O2}$, obtained from the Monte Carlo error analysis procedure, including the uncertainty of $[CH_3]_0$, k_2, k_3 and k_7. The dashed gray line shows the average of total nine measurements. The dotted light gray lines show the average values using different k_{12} in the model (Figure S24 and S25).

There is only one other study of the reaction of CH_2OO + CH_3O_2 in the literature to date.[19] Acetone photolysis was utilized to generate peroxy radicals, which resulted in the simultaneous generation of $CH_3C(O)O_2$ and CH_3O_2, while monochromatic Cavity Ring-down spectroscopy was used for the detection of transient species. While highly sensitive, the single wavelength method was unable to independently measure $CH_3C(O)O_2$, CH_3O_2 and CH_2OO. By assuming the same rate coefficients for reactions of $CH_2OO + CH_3O_2$ and $CH_2OO + CH_3C(O)O_2$, they reported a rate coefficient $k(CH_2OO + RO_2, RO_2 = CH_3O_2$ or $CH_3C(O)O_2) = (2.4\pm1.2)\times10^{-11}$ cm^3 s^{-1}.[19] This agrees with our measured $k_{CH2OO+CH3O2}$ within the large reported experimental uncertainty. Nevertheless, the results of both studies serve to suggest that the reactivities of Criegee intermediates toward peroxy radicals are similar, *i.e.*, fast and of the order of ~ 10^{-11} cm^3 s^{-1}. Clearly, there is considerable uncertainty and further work on the reaction between $CH_3C(O)O_2$ with CH_2OO is required.

Theoretical calculations suggest that the terminal oxygen of the peroxy radical approaches the central carbon of the Criegee intermediate and donates its unpaired electron to the central carbon.[20,21] While this interaction is repulsive for the ground state of CH_2OO due to its zwitterionic character, mixing with a triplet excited state can lead to a strongly bound potential.[20] The addition reaction can be compared to that of radicals and carbonyl moiety, such as formaldehyde. The energy of the lowest triplet excited state of CH_2OO is 1.4 eV (32.3 kcal mol^{-1}),[20] 2.7 times lower than the lowest excited state energy (87.6 kcal mol^{-1})[42] of formaldehyde. Notably, the reaction rate of HO_2 with formaldehyde is quite slow (~3×10^{-14} cm^3 s^{-1}),[43] implying that the mixing between the singlet ground state and the triplet excited state may be weak for formaldehyde, likely because of the significant energy gap.

The $CH_2OO + CH_3O_2$ rate coefficient of 4×10^{-12} cm^3 s^{-1} was calculated at CASPT2(19, 15)/aug-cc-pVTZ level[21] and is four times slower than our measurements. This discrepancy points to the need for a more sophisticated treatment of the mixing of the excited state at the transition state structure beyond the perturbation method, e.g., multi-reference configuration interaction method, in order to fully understand the reaction of Criegee intermediates with peroxy radicals.

Association reactions of Criegee intermediates, such as the reaction with organic acids, results in the formation of low vapor pressure reaction products and can contribute to SOA formation.[44] Such reactions have been shown to be of particular importance in the Amazon rainforest, where Criegee intermediates are estimated to achieve concentrations as high as 2000 cm^{-3}.[45] Field measurements have revealed significant SOA formation, yet current atmospheric models struggle to replicate this observation.[4] Chamber experiments further suggest that oligomers play an important role in the mechanism of particle formation.[7] By integrating new reaction pathways, such as the fast reactions involving peroxy radicals reported in this study, and water enhancement effects of reactions with hydrogen-bonding molecules,[12] the gap between empirical models and filed measurements might be bridged.

In this study, we investigated the $CH_2OO + CH_3O_2$ reaction using a White cell multipass UV-Vis spectrometer coupled with a pulsed-laser-photolysis flow reactor. The CH_2OO and CH_3O_2 were generated by photolyzing CH_2I_2 and CH_3I, respectively, in the presence of oxygen. Photolysis of the $CH_3I/O_2/N_2$ mixture produced a prominent absorption signal with peak position near 290 nm, which was attributed to the formation of CH_3OOI. The absorption temporal profiles of CH_2OO were monitored near 340 nm at low pressures, which mitigated the impacts of $CH_3O_2 + I$ and $CH_2OO + I$ reactions, and we were able to determine the $CH_2OO + CH_3O_2$ reaction rate coefficient $k_{CH2OO+CH3O2} = (1.7 \pm 0.5)\times10^{-11}$ $cm^3\ s^{-1}$ at 10 Torr and 294 K.

6.4—Experimental Methods

The experimental setup was described in our previous works.[22] In short, we utilized a free-space broadband light source (LDLS, Energetiq EQ-99) that was collimated using parabolic mirrors (Thorlab, MPD149–F01, RFL = 101.6 mm, 90° OAP) and directed through a White cell. The photolysis laser passed through the gap between the object mirrors, and was directed co-linearly with the flow reactor and fully overlapped with the probe beam, achieving an effective absorption pathlength of $L_{\mathrm{eff}} \approx 450$ cm. After passing through the multipass system, the probe beam was focused into a dual-exit spectrograph. We used two spectrographs over the course of this study, fitted with either a 600 grooves/mm (Princeton Instruments, SpectraPro HRS−300) or a 300 grooves/mm grating (Acton Research Corporation, SpectraPro 300i), each offering distinct spectral resolution and coverage. A half-height mirror in the spectrograph splits the probe beam, directing the lower portion to a photomultiplier tube (Hamamatsu R928) and the upper portion to an intensified CCD camera (Princeton Instruments PI-MAX4, 1024x256), allowing for simultaneous spectral and fixed wavelength temporal light collection.

A small stream of nitrogen flowed through a bubbler containing CH_2I_2 (Sigma-Aldrich >99%) and copper shavings as a stabilizer. The bubbler was held in a temperature-controlled bath at 292 K (Fisherbrand, Isotemp 4100). CH_3I (Sigma-Aldrich > 99.5%) was purified using freeze-pump-thaw techniques and stored in a nitrogen-balanced cylinder. These sample flows were mixed with an oxygen flow (Airgas, Ultra High Purity) and a buffer flow of N_2 in a mixing volume approximately 100 cm long before being directed into a temperature-regulated double-jacket flow reactor (240–298 K, ± 2 K). The reactor's pressure was continuously monitored and controlled using a pressure gauge (MKS 127AA-00100A, 0 - 100 Torr) and a throttle valve (MKS type 153). The gas mixture underwent photolysis at 248 nm via an excimer laser (Coherent COMPex 205F, KrF), which was isolated from the spectrograph using a long-pass filter (Semrock LP02-257RU-30x40). Typical concentrations in this study ranged from $[CH_2I_2] = (2.6–5.1)\times10^{13}$ cm^{-3}, $[CH_3I] = (0–1.3)\times10^{15}$ cm^{-3}, with O_2 between 5−10 Torr, balanced with N_2 between 10−90 Torr, and temperatures set at either 238 or 294 K.

Analysis routines were developed for simulating and fitting the kinetic traces, which made use of numerical ordinary differential equation solver from the SciPy libary[46] and the nonlinear least-squares fitting library LMFIT.[47] For the Monte Carlo analysis, specified parameters were varied as standard normal random variables with a specified standard deviation. Each run was fit with 1024 different random inputs, and the results were compiled to provide an estimated error for the floating parameters.

6.5—References

1. Taatjes, C. A., Shallcross, D. E. & Percival, C. J. Research frontiers in the chemistry of Criegee intermediates and tropospheric ozonolysis. *Phys. Chem. Chem. Phys.* **16**, 1704–1718 (2014).
2. Khan, M. A. H., Percival, C. J., Caravan, R. L., Taatjes, C. A. & Shallcross, D. E. Criegee intermediates and their impacts on the troposphere. *Environ. Sci.: Processes Impacts* **20**, 437–453 (2018).
3. Chhantyal-Pun, R., et al. Criegee intermediates: production, detection and reactivity. *Int. Rev. Phys. Chem.* **39**, 385–424 (2020).
4. Zhao, B., et al. High concentration of ultrafine particles in the Amazon free troposphere produced by organic new particle formation. *Proc. Natl. Acad. Sci. U.S.A.* **117**, 25344–25351 (2020).
5. Zhao, Y., Wingen, L. M., Perraud, V., Greaves, J. & Finlayson-Pitts, B. J. Role of the reaction of stabilized Criegee intermediates with peroxy radicals in particle formation and growth in air. *Phys. Chem. Chem. Phys.* **17**, 12500–12514 (2015).
6. Sakamoto, Y., Inomata, S. & Hirokawa, J. Oligomerization Reaction of the Criegee Intermediate Leads to Secondary Organic Aerosol Formation in Ethylene Ozonolysis. *J. Phys. Chem. A* **117**, 12912–12921 (2013).
7. Gong, Y., Jiang, F., Li, Y., Leisner, T. & Saathoff, H. Impact of temperature on the role of Criegee intermediates and peroxy radicals in dimer formation from β -pinene ozonolysis. *Atmos. Chem. Phys.* **24**, 167–184 (2024).
8. Welz, O., et al. Direct Kinetic Measurements of Criegee Intermediate (CH_2OO) Formed by Reaction of CH_2I with O_2. *Science* **335**, 204–207 (2012).

9. Taatjes, C. A., et al. Direct Measurements of Conformer-Dependent Reactivity of the Criegee Intermediate CH_3CHOO. *Science* **340**, 177–180 (2013).
10. Jr-Min Lin, J. & Chao, W. Structure-dependent reactivity of Criegee intermediates studied with spectroscopic methods. *Chem. Soc. Rev.* **46**, 7483–7497 (2017).
11. Osborn, D. L. & Taatjes, C. A. The physical chemistry of Criegee intermediates in the gas phase. *Int. Rev. Phys. Chem.* **34**, 309–360 (2015).
12. Chao, W., Yin, C., Takahashi, K. & Lin, J. J.-M. Hydrogen-Bonding Mediated Reactions of Criegee Intermediates in the Gas Phase: Competition between Bimolecular and Termolecular Reactions and the Catalytic Role of Water. *J. Phys. Chem. A* **123**, 8336–8348 (2019).
13. Lester, M. I. & Klippenstein, S. J. Unimolecular Decay of Criegee Intermediates to OH Radical Products: Prompt and Thermal Decay Processes. *Acc. Chem. Res.* **51**, 978–985 (2018).
14. Caravan, R. L., et al. Products of Criegee intermediate reactions with NO_2: experimental measurements and tropospheric implications. *Faraday Discuss.* **200**, 313–330 (2017).
15. Caravan, R. L., et al. Direct kinetic measurements and theoretical predictions of an isoprene-derived Criegee intermediate. *Proc. Natl. Acad. Sci. U.S.A.* **117**, 9733–9740 (2020).
16. Lin, Y.-H., Yin, C., Takahashi, K. & Lin, J. J.-M. Surprisingly long lifetime of methacrolein oxide, an isoprene derived Criegee intermediate, under humid conditions. *Commun Chem* **4**, 12 (2021).
17. Taatjes, C. A. Criegee Intermediates: What Direct Production and Detection Can Teach Us About Reactions of Carbonyl Oxides. *Annu. Rev. Phys. Chem.* **68**, 183–207 (2017).

18. Chhantyal-Pun, R., et al. Direct Measurements of Unimolecular and Bimolecular Reaction Kinetics of the Criegee Intermediate $(CH_3)_2$ COO. *J. Phys. Chem. A* **121**, 4–15 (2017).
19. Chhantyal-Pun, R., et al. Impact of Criegee Intermediate Reactions with Peroxy Radicals on Tropospheric Organic Aerosol. *ACS Earth Space Chem.* **4**, 1743–1755 (2020).
20. Miliordos, E. & Xantheas, S. S. The Origin of the Reactivity of the Criegee Intermediate: Implications for Atmospheric Particle Growth. *Angew. Chem. Int. Ed.* **55**, 1015–1019 (2016).
21. Anglada, J. M., Olivella, S. & Solé, A. The reaction of formaldehyde carbonyl oxide with the methyl peroxy radical and its relevance in the chemistry of the atmosphere. *Phys. Chem. Chem. Phys.* **15**, 18921–18933 (2013).
22. Winiberg, F. A. F., et al. A white cell based broadband transient UV-vis absorption spectroscopy with pulsed laser photolysis reactors for chemical kinetics under variable temperatures and pressures. *Rev. Sci. Instrum.* **94**, 114103 (2023).
23. Sheps, L. Absolute Ultraviolet Absorption Spectrum of a Criegee Intermediate CH_2OO. *J. Phys. Chem. Lett.* **4**, 4201–4205 (2013).
24. Burkholder, J. B., et al. JPL Publication 19-5. Chemical Kinetics and Photochemical Data for Use in Atmospheric Studies. *JPL Publication* **19–5**, 2–7 (2020).
25. Zhu, R., Hsu, C.-C. & Lin, M. C. *Ab initio* study of the CH3+O2 reaction: Kinetics, mechanism and product branching probabilities. *J. Chem. Phys.* **115**, 195–203 (2001).
26. Spietz, P., Gómez Martín, J. C. & Burrows, J. P. Spectroscopic studies of the I_2/O_3 photochemistry. *J. Photochem. Photobiol., A* **176**, 50–67 (2005).
27. Wu, Y.-J., Takahashi, K. & Lin, J. J.-M. Kinetics of the Simplest Criegee Intermediate Reaction with Water Vapor: Revisit and Isotope Effect. *J. Phys. Chem. A* **127**, 8059–8072 (2023).

28. Huang, Y.-H., Chen, L.-W. & Lee, Y.-P. Simultaneous Infrared Detection of the ICH<sub>2</subOO Radical and Criegee Intermediate CH $_2$OO: The Pressure Dependence of the Yield of CH_2OO in the Reaction CH_2I + O_2. *J. Phys. Chem. Lett.* **6**, 4610–4615 (2015).
29. Dillon, T. J., Tucceri, M. E. & Crowley, J. N. Laser induced fluorescence studies of iodine oxide chemistry: Part II. The reactions of IO with CH_3O_2, CF_3O_2 and O_3. *Phys. Chem. Chem. Phys.* **8**, 5185–5198 (2006).
30. Jenkin, M. E., Cox, R. A., Mellouki, A., Le Bras, G. & Poulet, G. Kinetics of the reaction of iodine atoms with hydroperoxyl radicals. *J. Phys. Chem.* **94**, 2927–2934 (1990).
31. Ting, W.-L., et al. Detailed mechanism of the CH_2I + O_2 reaction: Yield and self-reaction of the simplest Criegee intermediate CH_2OO. *J. Chem. Phys.* **141**, 104308 (2014).
32. Foreman, E. S. & Murray, C. Kinetics of IO Production in the CH_2I + O_2 Reaction Studied by Cavity Ring-Down Spectroscopy. *J. Phys. Chem. A* **119**, 8981–8990 (2015).
33. Liu, Y., et al. A kinetic study of the CH_2OO Criegee intermediate reaction with SO_2, $(H_2O)_2$, CH_2I_2 and I atoms using OH laser induced fluorescence. *Phys. Chem. Chem. Phys.* **19**, 20786–20794 (2017).
34. Chhantyal-Pun, R., Davey, A., Shallcross, D. E., Percival, C. J. & Orr-Ewing, A. J. A kinetic study of the CH_2OO Criegee intermediate self-reaction, reaction with SO_2 and unimolecular reaction using cavity ring-down spectroscopy. *Phys. Chem. Chem. Phys.* **17**, 3617–3626 (2015).
35. Atkinson, R., et al. Evaluated kinetic and photochemical data for atmospheric chemistry: Volume III – gas phase reactions of inorganic halogens. *Atmos. Chem. Phys.* **7**, 981–1191 (2007).

36. Onel, L., et al. Kinetics and Product Branching Ratio Study of the CH_3O_2 Self-Reaction in the Highly Instrumented Reactor for Atmospheric Chemistry. *J. Phys. Chem. A* **126**, 7639–7649 (2022).

37. Assaf, E., Schoemaecker, C., Vereecken, L. & Fittschen, C. The reaction of fluorine atoms with methanol: yield of CH_3O/CH_2OH and rate constant of the reactions $CH_3O + CH_3O$ and $CH_3O + HO_2$. *Phys. Chem. Chem. Phys.* **20**, 10660–10670 (2018).

38. Mir, Z. S., et al. CH_2OO Criegee intermediate UV absorption cross-sections and kinetics of $CH_2OO + CH_2OO$ and $CH_2OO + I$ as a function of pressure. *Phys. Chem. Chem. Phys.* **22**, 9448–9459 (2020).

39. Su, Y.-T., et al. Extremely rapid self-reaction of the simplest Criegee intermediate CH_2OO and its implications in atmospheric chemistry. *Nat. Chem.* **6**, 477–483 (2014).

40. Buras, Z. J., Elsamra, R. M. I. & Green, W. H. Direct Determination of the Simplest Criegee Intermediate (CH_2OO) Self Reaction Rate. *J. Phys. Chem. Lett.* **5**, 2224–2228 (2014).

41. Zhang, Y., Song, R., Sun, Y., Sun, J. & Wang, R. Mechanistic and kinetic study on the reaction of methylperoxyl radical with atomic iodine. *J. Mol. Graphics Modell.* **76**, 512–520 (2017).

42. Clouthier, D. J. & Ramsay, D. A. The Spectroscopy of Formaldehyde and Thioformaldehyde. *Annu. Rev. Phys. Chem.* **34**, 31–58 (1983).

43. Morajkar, P., Schoemaecker, C., Okumura, M. & Fittschen, C. Direct Measurement of the Equilibrium Constants of the Reaction of Formaldehyde and Acetaldehyde with HO_2 Radicals. *Int. J. Chem. Kinet.* **46**, 245–259 (2014).

44. Johnson, D. & Marston, G. The gas-phase ozonolysis of unsaturated volatile organic compounds in the troposphere. *Chem. Soc. Rev.* **37**, 699–716 (2008).

45. Chhantyal-Pun, R., et al. Direct Kinetic and Atmospheric Modeling Studies of Criegee Intermediate Reactions with Acetone. *ACS Earth Space Chem.* **3**, 2363–2371 (2019).

46. Virtanen, P., et al. SciPy 1.0: fundamental algorithms for scientific computing in Python. *Nat. Methods* **17**, 261–272 (2020).

47. Newville, M., et al. LMFIT: Non-Linear Least-Square Minimization and Curve-Fitting for Python. [object Object] https://doi.org/10.5281/ZENODO.598352 (2014).